The Astrophysical Journal Supplement Series, 170:377–408, 2007 June

THREE-YEAR *WILKINSON MICROWAVE ANISOTROPY PROBE* (*WMAP*) OBSERVATIONS: IMPLICATIONS FOR COSMOLOGY

D. N. Spergel,[1,2] R. Bean,[1,3] O. Doré,[1,4] M. R. Nolta,[4,5] C. L. Bennett,[6,7] J. Dunkley,[1,5] G. Hinshaw,[6] N. Jarosik,[5] E. Komatsu,[1,8] L. Page,[5] H. V. Peiris,[1,9,10] L. Verde,[1,11] M. Halpern,[12] R. S. Hill,[6,13] A. Kogut,[6] M. Limon,[6] S. S. Meyer,[9] N. Odegard,[6,13] G. S. Tucker,[14] J. L. Weiland,[6,13] E. Wollack,[6] and E. L. Wright[15]

Received 2006 March 16; accepted 2007 January 12

ABSTRACT

A simple cosmological model with only six parameters (matter density, $\Omega_m h^2$, baryon density, $\Omega_b h^2$, Hubble constant, H_0, amplitude of fluctuations, σ_8, optical depth, τ, and a slope for the scalar perturbation spectrum, n_s) fits not only the 3 year *WMAP* temperature and polarization data, but also small-scale CMB data, light element abundances, large-scale structure observations, and the supernova luminosity/distance relationship. Using *WMAP* data only, the best-fit values for cosmological parameters for the power-law flat Λ cold dark matter (ΛCDM) model are $(\Omega_m h^2, \Omega_b h^2, h, n_s, \tau, \sigma_8) = (0.1277^{+0.0080}_{-0.0079}, 0.02229 \pm 0.00073, 0.732^{+0.031}_{-0.032}, 0.958 \pm 0.016, 0.089 \pm 0.030, 0.761^{+0.049}_{-0.048})$. The 3 year data dramatically shrink the allowed volume in this six-dimensional parameter space. Assuming that the primordial fluctuations are adiabatic with a power-law spectrum, the *WMAP* data *alone* require dark matter and favor a spectral index that is significantly less than the Harrison-Zel'dovich-Peebles scale-invariant spectrum ($n_s = 1,\ r = 0$). Adding additional data sets improves the constraints on these components and the spectral slope. For power-law models, *WMAP* data alone puts an improved upper limit on the tensor-to-scalar ratio, $r_{0.002} < 0.65$ (95% CL) and the combination of *WMAP* and the lensing-normalized SDSS galaxy survey implies $r_{0.002} < 0.30$ (95% CL). Models that suppress large-scale power through a running spectral index or a large-scale cutoff in the power spectrum are a better fit to the *WMAP* and small-scale CMB data than the power-law ΛCDM model; however, the improvement in the fit to the *WMAP* data is only $\Delta\chi^2 = 3$ for 1 extra degree of freedom. Models with a running-spectral index are consistent with a higher amplitude of gravity waves. In a flat universe, the combination of *WMAP* and the Supernova Legacy Survey (SNLS) data yields a significant constraint on the equation of state of the dark energy, $w = -0.967^{+0.073}_{-0.072}$. If we assume $w = -1$, then the deviations from the critical density, Ω_K, are small: the combination of *WMAP* and the SNLS data implies $\Omega_k = -0.011 \pm 0.012$. The combination of *WMAP* 3 year data plus the *HST* Key Project constraint on H_0 implies $\Omega_k = -0.014 \pm 0.017$ and $\Omega_\Lambda = 0.716 \pm 0.055$. Even if we do not include the prior that the universe is flat, by combining *WMAP*, large-scale structure, and supernova data, we can still put a strong constraint on the dark energy equation of state, $w = -1.08 \pm 0.12$. For a flat universe, the combination of *WMAP* and other astronomical data yield a constraint on the sum of the neutrino masses, $\sum m_\nu < 0.66$ eV (95%CL). Consistent with the predictions of simple inflationary theories, we detect no significant deviations from Gaussianity in the CMB maps using Minkowski functionals, the bispectrum, trispectrum, and a new statistic designed to detect large-scale anisotropies in the fluctuations.

Subject headings: cosmic microwave background — cosmology: observations

1. INTRODUCTION

The power-law ΛCDM model fits not only the *Wilkinson Microwave Anisotropy Probe* (*WMAP*) first-year data, but also a wide range of astronomical data (Bennett et al. 2003; Spergel et al. 2003). In this model, the universe is spatially flat, homogeneous, and isotropic on large scales. It is composed of ordinary matter, radiation, and dark matter and has a cosmological constant. The primordial fluctuations in this model are adiabatic, nearly scale-invariant Gaussian random fluctuations (Komatsu et al. 2003). Six cosmological parameters (the density of matter, the density of atoms, the expansion rate of the universe, the amplitude of the primordial fluctuations, their scale dependence, and the optical depth of the universe) are enough to predict not only the statistical properties of the microwave sky, measured by *WMAP* at several hundred thousand points on the sky, but also the large-scale distribution of matter and galaxies, mapped by the Sloan Digital Sky Survey (SDSS) and the 2dF Galaxy Redshift Survey (2dFGRS).

With 3 years of integration, improved beam models, better understanding of systematic errors (Jarosik et al. 2007), temperature data (Hinshaw et al. 2007), and polarization data (Page et al. 2007), the *WMAP* data have significantly improved. There have also been significant improvements in other astronomical data

[1] Department of Astrophysical Sciences, Princeton University, Princeton, NJ 08544-1001; dns@astro.princeton.edu.
[2] Visiting Scientist, Cerro-Tololo Inter-American Observatory.
[3] Cornell University, Ithaca, NY 14853.
[4] Canadian Institute for Theoretical Astrophysics, University of Toronto, ON M5S 3H8, Canada.
[5] Department of Physics, Jadwin Hall, Princeton University, Princeton, NJ 08544-0708.
[6] NASA Goddard Space Flight Center, Greenbelt, MD 20771.
[7] Department of Physics and Astronomy, The Johns Hopkins University, Baltimore, MD 21218-2686.
[8] Department of Astronomy, University of Texas, Austin, TX.
[9] Deptartments of Astrophysics and Physics, KICP and EFI, University of Chicago, Chicago, IL 60637.
[10] Hubble Fellow.
[11] Department of Physics, University of Pennsylvania, Philadelphia, PA.
[12] Department of Physics and Astronomy, University of British Columbia, Vancouver, BC V6T 1Z1, Canada.
[13] Science Systems and Applications, Inc. (SSAI), Lanham, MD 20706.
[14] Department of Physics, Brown University, Providence, RI 02912-1843.
[15] UCLA Astronomy, Los Angeles, CA 90095-1562.

TABLE 1
Cosmological Parameters Used in the Analysis

Parameter	Description	Definition
H_0	Hubble expansion factor	$H_0 = 100h$ Mpc^{-1} km s^{-1}
ω_b	Baryon density	$\omega_b = \Omega_b h^2 = \rho_b/1.88 \times 10^{-26}$ kg m^{-3}
ω_c	Cold dark matter density	$\omega_c = \Omega_c h^2 = \rho_c/18.8$ yoctograms m^{-3}
f_ν	Massive neutrino fraction	$f_\nu = \Omega_\nu/\Omega_c$
$\sum m_\nu$	Total neutrino mass (eV)	$\sum m_\nu = 94\Omega_\nu h^2$
N_ν	Effective number of relativistic neutrino species	
Ω_k	Spatial curvature	
$\Omega_{\rm DE}$	Dark energy density	For $w = -1$, $\Omega_\Lambda = \Omega_{\rm DE}$
Ω_m	Matter energy density	$\Omega_m = \Omega_b + \Omega_c + \Omega_\nu$
w	Dark energy equation of state	$w = p_{\rm DE}/\rho_{\rm DE}$
$\Delta^2_{\mathcal{R}}$	Amplitude of curvature perturbations $\mathcal{R}$	$\Delta^2_{\mathcal{R}}(k = 0.002$ Mpc$^{-1}) \approx 29.5 \times 10^{-10} A$
A	Amplitude of density fluctuations ($k = 0.002$ Mpc^{-1})	See Spergel et al. (2003)
n_s	Scalar spectral index at 0.002 Mpc^{-1}	
α	Running in scalar spectral index	$\alpha = dn_s/dlnk$ (assume constant)
r	Ratio of the amplitude of tensor fluctuations to scalar potential fluctuations at $k = 0.002$ Mpc^{-1}	
n_t	Tensor spectral index	Assume $n_t = -r/8$
τ	Reionization optical depth	
σ_8	Linear theory amplitude of matter fluctuations on 8 h^{-1} Mpc	
Θ_s	Acoustic peak scale (deg)	See Kosowsky et al. (2002)
$A_{\rm SZ}$	SZ marginalization factor	See Appendix A
$b_{\rm SDSS}$	Galaxy bias factor for SDSS sample	$b = [P_{\rm SDSS}(k, z = 0)/P(k)]^{1/2}$ (constant)
$C^{\rm TT}_{220}$	Amplitude of the TT temperature power spectrum at $l = 220$	
z_s	Weak lensing source redshift	

Note.—The Web site http://lambda.gsfc.nasa.gov lists the marginalized values for these parameters for all of the models discussed in this paper.

sets: analysis of galaxy clustering in the SDSS (Tegmark et al. 2004a; Eisenstein et al. 2005) and the completion of the 2dFGRS (Cole et al. 2005); improvements in small-scale CMB measurements (Kuo et al. 2004; Readhead et al. 2004a, 2004b; Grainge et al. 2003; Leitch et al. 2005; Piacentini et al. 2006; Montroy et al. 2006; O'Dwyer et al. 2005); much larger samples of high-redshift supernova (Riess et al. 2004; Astier et al. 2005; Nobili et al. 2005; Clocchiatti et al. 2006; Krisciunas et al. 2005); and significant improvements in the lensing data (Refregier 2003; Heymans et al. 2005; Semboloni et al. 2006; Hoekstra et al. 2006).

In § 2, we describe the basic analysis methodology used, with an emphasis on changes since the first year. In § 3, we fit the ΛCDM model to the *WMAP* temperature and polarization data. With its basic parameters fixed at $z \sim 1100$, this model predicts the properties of the low-redshift universe: the galaxy power spectrum, the gravitational lensing power spectrum, the Hubble constant, and the luminosity-distance relationship. In § 4, we compare the predictions of this model to a host of astronomical observations. We then discuss the results of combined analysis of *WMAP* data, other astronomical data, and other CMB data sets. In § 5, we use the *WMAP* data to constrain the shape of the power spectrum. In § 6, we consider the implications of the *WMAP* data for our understanding of inflation. In § 7, we use these data sets to constrain the composition of the universe: the equation of state of the dark energy, the neutrino masses, and the effective number of neutrino species. In § 8, we search for non-Gaussian features in the microwave background data. The conclusions of our analysis are described in § 9.

2. METHODOLOGY

The basic approach of this paper is similar to that of the first-year *WMAP* analysis: our goal is to find the simplest model that fits the CMB and large-scale structure data. Unless explicitly noted in § 2.1, we use the methodology described in Verde et al. (2003) and applied in Spergel et al. (2003). We use Bayesian statistical techniques to explore the shape of the likelihood function, we use Monte Carlo Markov chain methods to explore the likelihood surface, and we quote both our maximum-likelihood parameters and the marginalized expectation value for each parameter in a given model:

$$\langle \alpha_i \rangle = \int d^N \alpha \, \mathcal{L}(d|\alpha) p(\alpha) \alpha_i = \frac{1}{M} \sum_{j=1}^{M} \alpha_i^j, \qquad (1)$$

where α_i^j is the value of the ith parameter in the chain and j indexes the chain element. The number of elements (M) in the typical merged Markov chain is at least 50,000 and is always long enough to satisfy the Gelman & Rubin (1992) convergence test with $R < 1.1$. In addition, we use the spectral convergence test described in Dunkley et al. (2005) to confirm convergence. Most merged chains have over 100,000 elements. We use a uniform prior on cosmological parameters, $p(\alpha)$, unless otherwise specified. We refer to $\langle \alpha_i \rangle$ as the best-fit value for the parameter and the peak of the likelihood function as the best-fit model.

The Markov chain outputs and the marginalized values of the cosmological parameters listed in Table 1 are available online[16] for all of the models discussed in the paper.

2.1. *Changes in Analysis Techniques*

We now use not only the measurements of the temperature power spectrum (TT) and the temperature polarization power spectrum (TE), but also measurements of the polarization power spectra (EE) and (BB).

[16] See http://lambda.gsfc.nasa.gov.

At the lowest multipoles, a number of the approximations used in the first-year analysis were suboptimal. Efstathiou (2004) notes that a maximum-likelihood analysis is significantly better than a quadratic estimator analysis at $l = 2$. Slosar et al. (2004) note that the shape of the likelihood function at $l = 2$ is not well approximated by the fitting function used in the first-year analysis (Verde et al. 2003). More accurate treatments of the low-l likelihoods decrease the significance of the evidence for a running spectral index (Efstathiou 2004; Slosar et al. 2004; O'Dwyer et al. 2004). Hinshaw et al. (2007) and Page et al. (2007) describe our approach to addressing this concern: for low multipoles, we explicitly compute the likelihood function for the *WMAP* temperature and polarization maps. For the analysis of the polarization maps, we use the resolution $N_{\rm side} = 8N^{-1}$ matrices. This pixel-based method is used for $C_l^{\rm TT}$ for $2 \leq l \leq 30$ and polarization for $2 \leq l \leq 23$. For most of the analyses in the paper, we use a $N_{\rm side} = 8$ version of the temperature map for the analysis of the low- l likelihood that uses a pixel-based version for $l \leq 12$. For the *WMAP* ΛCDM only case, we use the more time-consuming $N_{\rm side} = 16$ version of the code. Hinshaw et al. (2007) compares various approaches toward computing the low-l likelihood. In Appendix A, we discuss various choices made in the maximum-likelihood code. For the ΛCDM model, we have computed the best-fit parameters using a range of assumptions for the amplitude of point source contamination and different treatments of the low-l likelihood.

There are several improvements in our analysis of high-l temperature data (Hinshaw et al. 2007): better beam models, improved foreground models, and the use of maps with smaller pixels ($N_{\rm side} = 1024$). The improved foreground model is significant at $l < 200$. The $N_{\rm side} = 1024$ maps significantly reduce the effects of subpixel CMB fluctuations and other pixelization effects. We found that $N_{\rm side} = 512$ maps had higher χ^2 than $N_{\rm side} = 1024$ maps, particularly for $l = 600$–700, where there is significant signal-to-noise and pixelization effects are significant.

We now marginalize over the amplitude of Sunyaev-Zel'dovich (SZ) fluctuations. The expected level of SZ fluctuations (Refregier et al. 2000; Komatsu & Seljak 2001; Bond et al. 2005) is $l(l+1)C_l/(2\pi) = 19 \pm 3\ \mu{\rm K}^2$ at $l = 450$–800 for $\Omega_m = 0.26$, $\Omega_b = 0.044$, $h = 0.72$, $n_s = 0.97$, and $\sigma_8 = 0.80$. The amplitude of SZ fluctuations is very sensitive to σ_8 (Komatsu & Kitayama 1999; Komatsu & Seljak 2001). For example at 60 GHz, $l(l+1)C_l/(2\pi) = 65 \pm 15\ \mu{\rm K}^2$ at $l = 450$–800 for $\sigma_8 = 0.91$, which is comparable to the *WMAP* statistical errors at the same multipole range. Since the *WMAP* spectral coverage is not sufficient to be able to distinguish CMB fluctuations from SZ fluctuations (see discussion in Hinshaw et al. 2007), we marginalize over its amplitude using the Komatsu & Seljak (2002) analytical model for the shape of the SZ fluctuations. We impose the prior that the SZ signal is between 0 and 2 times the Komatsu & Seljak (2002) value. Consistent with the analysis of Huffenberger et al. (2004) we find that the SZ contribution is not a significant contaminant to the CMB signal on the scales probed by the *WMAP* experiment. We report the amplitude of the SZ signal normalized to the Komatsu & Seljak (2002) predictions for the cosmological parameters listed above with $\sigma_8 = 0.80$. $A_{\rm SZ} = 1$ implies that the SZ contribution is 8.4, 18.7, and 25.2 $(\mu{\rm K})^2$ at $l = 220$, 600, and 1000, respectively. We discuss the effects of this marginalization in Appendix A. We have checked that gravitational lensing of the microwave background, the next most significant secondary effect after the thermal SZ effect (Lewis & Challinor 2006) does not have a significant effect on parameters.

We now use the CAMB code (Lewis et al. 2000) for our analysis of the *WMAP* power spectrum. The CAMB code is derived from CMBFAST (Zaldarriaga & Seljak 2000) but has the advantage of running a factor of 2 faster on the Silicon Graphics, Inc. (SGI), machines used for the analysis in this paper. For the multipole range probed by *WMAP*, the numerical uncertainties and physical uncertainties in theoretical calculations of multipoles are about 1 part in 10^3 (Seljak et al. 2003), significantly smaller than the experimental uncertainties. When we compare the results to large-scale structure and lensing calculations, the analytical treatments of the growth of structure in the nonlinear regime are accurate to better than 10% on the smallest scales considered in this paper (Smith et al. 2003).

2.2. *Parameter Choices*

We consider constraints on the hot big bang cosmological scenario with Gaussian, adiabatic primordial fluctuations as would arise from single field, slow-roll inflation. We do not consider the influence of isocurvature modes nor the subsequent production of fluctuations from topological defects or unstable particle decay.

We parameterize our cosmological model in terms of 15 parameters:

$$\boldsymbol{p} = \{\omega_b,\ \omega_c,\ \tau,\ \Omega_\Lambda,\ w,\ \Omega_k,\ f_\nu,\ N_\nu,\ \Delta^2_{\mathcal{R}},\ n_s,\ r,\ dn_s/d\ln k,\ A_{\rm SZ},\ b_{\rm SDSS},\ z_s\}, \quad (2)$$

where these parameters are defined in Table 1. For the basic power-law ΛCDM model, we use ω_b, ω_c, $\exp(-2\tau)$, Θ_s, n_s, and $C^{\rm TT}_{l=220}$, as the cosmological parameters in the chain, $A_{\rm SZ}$ as a nuisance parameter, and unless otherwise noted, we assume a flat prior on these parameters. Note that τ is the optical depth since reionization. Prior to reionization, x_e is set to the standard value for the residual ionization computed in RECFAST (Seager et al. 2000). For other models, we use these same basic seven parameters plus the additional parameters noted in the text. Other standard cosmological parameters (also defined in Table 1), such as σ_8 and h, are functions of these six parameters. Appendix A discusses the dependence of results on the choice of priors.

With only 1 yr of *WMAP* data, there were significant degeneracies even in the ΛCDM model: there was a long degenerate valley in n_s-τ space, and there was also a significant degeneracy between n_s and $\Omega_b h^2$ (see Fig. 5 in Spergel et al. 2003). With the measurements of the rise to the third peak (Hinshaw et al. 2007) and the EE power spectrum (Page et al. 2007), these degeneracies are now broken (see § 3). However, more general models, most notably those with nonflat cosmologies and with richer dark energy or matter content, have strong parameter degeneracies. For models with adiabatic fluctuations, the *WMAP* data constrain the ratio of the matter density/radiation density, effectively, $\Omega_m h^2$, the baryon density, $\Omega_b h^2$, the slope of the primordial power spectrum and the distance to the surface of last scatter. In a flat vacuum energy-dominated universe, this distance is a function only of Ω and h, so the matter density and Hubble constant are well constrained. On the other hand, in nonflat models, there is a degeneracy between Ω_m, h and the curvature (see § 7.3). Similarly, in models with more complicated dark energy properties ($w \neq -1$), there is a degeneracy between Ω_m, h, and w. In models where the number of neutrino species is not fixed, the energy density in radiation is no longer known so that the *WMAP* data only constrain a combination of $\Omega_m h^2$ and the number of neutrino species. These degeneracies slow convergence as the Markov chains need to explore degenerate valleys in the likelihood surface.

3. ΛCDM MODEL: DOES IT STILL FIT THE DATA?

3.1. *WMAP Only*

The ΛCDM model is still an excellent fit to the *WMAP* data. With longer integration times and smaller pixels, the errors in the

TABLE 2

POWER-LAW ΛCDM MODEL PARAMETERS AND 68% CONFIDENCE INTERVALS

Parameter	First-Year Mean	WMAPext Mean	3 Year Mean (No SZ)	3 Year Mean	3 Year + ALL Mean
$100\Omega_b h^2$	$2.38^{+0.13}_{-0.12}$	$2.32^{+0.12}_{-0.11}$	2.23 ± 0.08	2.229 ± 0.073	2.186 ± 0.068
$\Omega_m h^2$	$0.144^{+0.016}_{-0.016}$	$0.134^{+0.006}_{-0.006}$	0.126 ± 0.009	$0.1277^{+0.0080}_{-0.0079}$	$0.1324^{+0.0042}_{-0.0041}$
H_0	72^{+5}_{-5}	73^{+3}_{-3}	73.5 ± 3.2	$73.2^{+3.1}_{-3.2}$	$70.4^{+1.5}_{-1.6}$
τ	$0.17^{+0.08}_{-0.07}$	$0.15^{+0.07}_{-0.07}$	$0.088^{+0.029}_{-0.030}$	0.089 ± 0.030	$0.073^{+0.027}_{-0.028}$
n_s	$0.99^{+0.04}_{-0.04}$	$0.98^{+0.03}_{-0.03}$	0.961 ± 0.017	0.958 ± 0.016	0.947 ± 0.015
Ω_m	$0.29^{+0.07}_{-0.07}$	$0.25^{+0.03}_{-0.03}$	0.234 ± 0.035	0.241 ± 0.034	0.268 ± 0.018
σ_8	$0.92^{+0.1}_{-0.1}$	$0.84^{+0.06}_{-0.06}$	0.76 ± 0.05	$0.761^{+0.049}_{-0.048}$	$0.776^{+0.031}_{-0.032}$

Parameter	First-Year ML	WMAPext ML	3 Year ML (No SZ)	3 Year ML	3 Year + ALL ML
$100\Omega_b h^2$	2.30	2.21	2.23	2.22	2.19
$\Omega_m h^2$	0.145	0.138	0.125	0.127	0.131
H_0	68	71	73.4	73.2	73.2
τ	0.10	0.10	0.0904	0.091	0.0867
n_s	0.97	0.96	0.95	0.954	0.949
Ω_m	0.32	0.27	0.232	0.236	0.259
σ_8	0.88	0.82	0.737	0.756	0.783

NOTES.—The 3 Year fits in the columns labeled "No SZ" use the likelihood formalism of the first-year paper and assume no SZ contribution, $A_{SZ} = 0$, to allow direct comparison with the first-year results. Fits that include SZ marginalization are given in the last two columns of the upper and lower parts of the table and represent our best estimate of these parameters. The last column includes all data sets.

high-l temperature multipoles have shrunk by more than a factor of 3. As the data have improved, the likelihood function remains peaked around the maximum-likelihood peak of the first-year *WMAP* value. With longer integration, the most discrepant high-l points from the first-year data are now much closer to the best-fit model (see Fig. 2). For the first-year *WMAP* TT and TE data (Spergel et al. 2003), the reduced $\chi^2_{\rm eff}$ was 1.09 for 893 degrees of freedom (dof) for the TT data and was 1.066 for the combined TT and TE data (893 + 449 = 1342 dof). For the 3 year data, which has much smaller errors for $l > 350$, the reduced $\chi^2_{\rm eff}$ for 982 dof (l = 13–1000; 7 parameters) is now 1.068 for the TT data and 1.041 for the combined TT and TE data (1410 dof, including TE l = 24–450), where the TE data contribution is evaluated from l = 24–500.

For the T, Q, and U maps using the pixel-based likelihood we obtain a reduced $\chi^2_{\rm eff} = 0.981$ for 1838 pixels (corresponding to $C_l^{\rm TT}$ for l = 2–12 and $C_l^{\rm TE}$ for l = 2–23). The combined reduced $\chi^2_{\rm eff} = 1.037$ for 3162 degrees of freedom for the combined fit to the TT and TE power spectrum at high l and the T, Q, and U maps at low l.

While many of the maximum-likelihood parameter values (Table 2, cols. [3] and [7], and Fig. 1) have not changed significantly, there has been a noticeable reduction in the marginalized value for the optical depth, τ, and a shift in the best-fit value of $\Omega_m h^2$. (Each shift is slightly larger than 1 σ). The addition of the EE data now eliminates a large region of parameter space with large τ and n_s that was consistent with the first-year data. With only the first-year data set, the likelihood surface was very flat. It

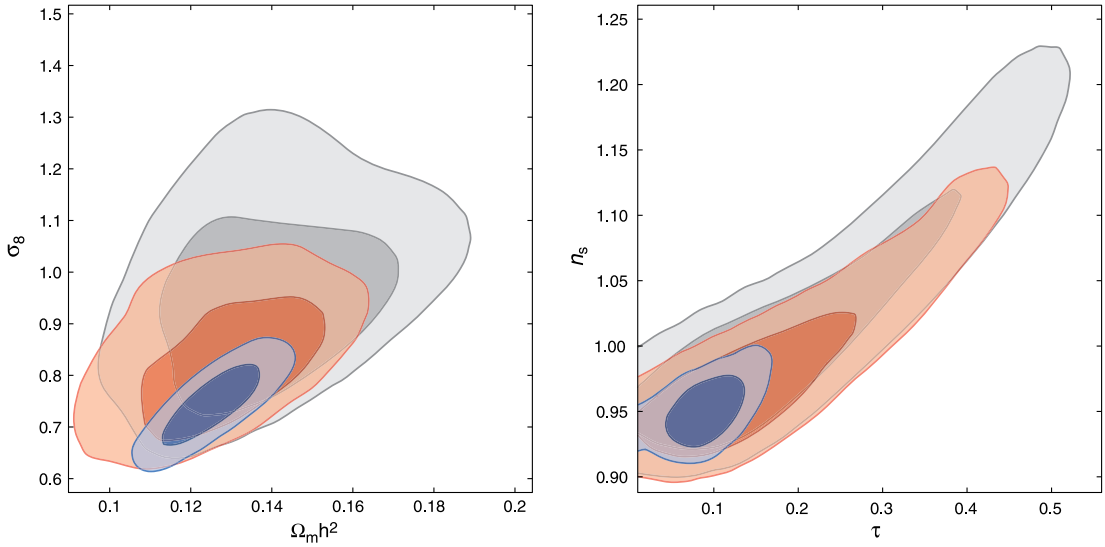

FIG. 1.—Improvement in parameter constraints for the power-law ΛCDM model (model M5 in Table 3). The contours show the 68% and 95% joint 2D marginalized contours for the ($\Omega_m h^2$, σ_8) plane (*left*) and the (n_s, τ) plane (*right*). The black contours represent the first-year *WMAP* data (with no prior on τ). The red contours show the first-year *WMAP* data combined with CBI and ACBAR (WMAPext in Spergel et al. 2003). The blue contours represent the three year *WMAP* data only with the SZ contribution set to 0 to maintain consistency with the first-year analysis. The *WMAP* measurements of EE power spectrum provide a strong constraint on the value of τ. The models with no reionization ($\tau = 0$) or a scale-invariant spectrum ($n_s = 1$) are both disfavored at $\Delta\chi^2_{\rm eff} > 6$ for five parameters (see Table 3). Improvements in the measurement of the amplitude of the third peak yield better constraints on $\Omega_m h^2$.

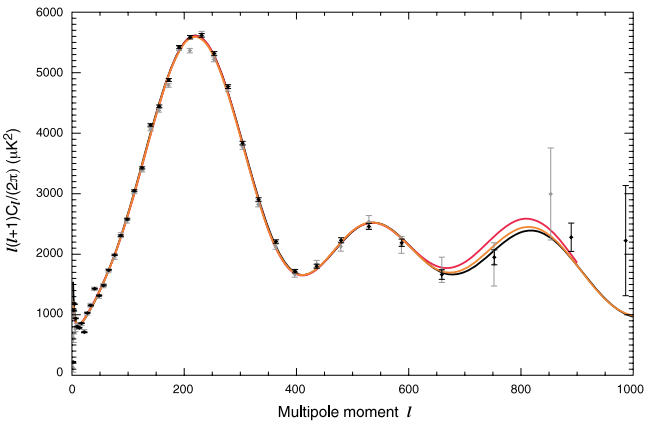

FIG. 2.—Comparison of the predictions of the different best-fit models to the data. The black line is the angular power spectrum predicted for the best-fit 3 year *WMAP* only ΛCDM model. The red line is the best fit to the 1 year *WMAP* data. The orange line is the best fit to the combination of the 1 year *WMAP* data, CBI and ACBAR (WMAPext in Spergel et al. 2003). The solid data points represent the 3 year data and the light gray data points the first-year data.

covered a ridge in τ-n_s over a region that extended from $\tau \simeq 0.07$ to nearly $\tau = 0.3$. If the optical depth of the universe were as large as $\tau = 0.3$ (a value consistent with the first-year data), then the measured EE signal would have been 10 times larger than the value reported in Page et al. (2007). On the other hand, an optical depth of $\tau = 0.05$ would produce one-quarter of the detected EE signal. As discussed in Page et al. (2007) the reionization signal is now based primarily on the EE signal rather than the TE signal. See Figure 26 in Page et al. (2007) for the likelihood plot for τ: note that the form of this likelihood function is relatively insensitive to the cosmological model (over the range considered in this paper).

There has also been a significant reduction in the uncertainties in the matter density, $\Omega_m h^2$. With the first year of *WMAP* data, the third peak was poorly constrained (see the light gray data points in Fig. 2). With 3 years of integration, the *WMAP* data better constrain the height of the third peak: *WMAP* is now cosmic variance limited up to $l = 400$, and the signal-to-noise ratio exceeds unity up to $l = 850$. The new best-fit *WMAP*-only model is close to the *WMAP* (first-year) + CBI + ACBAR model in the third peak region. As a result, the preferred value of $\Omega_m h^2$ now shifts closer to the "WMAPext" value reported in Spergel et al. (2003). Figure 1 shows the $\Omega_m h^2 - \sigma_8$ likelihood surfaces for the first-year *WMAP* data, the first-year WMAPext data and the 3 year *WMAP* data. The accurately determined peak position constrains $\Omega_m^{0.275} h$ (Page et al. 2003a), fixes the cosmological age, and determines the direction of the degeneracy surface. With 1 year data, the best-fit value is $\Omega_m^{0.275} h = 0.498$. With 3 years of data, the best fit shifts to $0.492^{+0.008}_{-0.017}$. The lower third peak implies a smaller value of $\Omega_m h^2$ and because of the peak constraint, a lower value of Ω_m.

The best-fit value of σ_8 (marginalized over the other parameters) is now noticeably smaller for the 3 year data alone, $0.761^{+0.049}_{-0.048}$ than for the first-year *WMAP* data alone, 0.92 ± 0.10. This lower value is due to a smaller third peak height, which leads to a lower value of Ω_m, and less structure growth and a lower best-fit value for τ. The height of the third peak was very uncertain with the first-year data alone. In Spergel et al. (2003) we used external CMB data sets to constrain the third peak and with these data, the maximum-likelihood value was 0.84. With 3 years of data, the third peak is better determined and its height is close to the value estimated from the ground-based data. With the EE measurements, we have eliminated most of the high-τ region of parameter space. Since higher values of τ imply a higher amplitude of primordial fluctuations, the best-fit value of σ is proportional to $\exp(\tau)$. For a model with all other parameters fixed, $\tau = 0.10$ implies a 7% lower value of σ_8. As discussed in § 4.1, this lower value of σ_8 is more consistent with the X-ray measurements but lower than the best-fit value from recent lensing surveys. Lower σ_8 implies later growth of structure.

In the first-year data, we assumed that the SZ contribution to the *WMAP* data was negligible. Appendix A discusses the change in priors and the change in the SZ treatment and their effects on parameters: marginalizing over SZ most significantly shifts n_s and σ_8 by 1% and 3%, respectively. In Table 2 in the column labeled No SZ and Figure 1, we assume $A_{\rm SZ} = 0$ and use the first-year likelihood code to make a consistent comparison between the first-year and 3 year results. As in the first-year analysis, we use a flat prior on the logarithm of the amplitude and a flat prior on Θ_s and a flat prior on τ. The first column of Table 5 list the parameters fitted to the *WMAP* 3 year data with $A_{\rm SZ}$ allowed to vary between 0 and 2. In the tables, the "mean" value is calculated according to equation (1) and the "maximum-likelihood (ML)" value is the value at the peak of the likelihood function. In the last two columns, we provide our current best estimate of parameters including SZ marginalization and using the full $N_{\rm side} = 16$ likelihood code to compute the TT likelihoods. In subsequent tables and figures, we will allow the SZ contribution to vary and quote the appropriate marginalized values. Allowing for an SZ contribution lowers the best-fit primordial contribution at high l; thus, the best-fit models with an SZ contribution have lower n_s and σ_8 values. However, in other tables, we use the faster $N_{\rm side} = 8$ likelihood code unless specifically noted. In all of the tables, we quote the 68% confidence intervals on parameters and the 95% confidence limits on bounded parameters.

3.2. *Reionization History*

Since the Kogut et al. (2003) detection of τ, the physics of reionization has been a subject of extensive theoretical study (Cen 2003; Ciardi et al. 2003; Haiman & Holder 2003; Madau et al. 2004; Oh & Haiman 2003; Venkatesan et al. 2003; Ricotti & Ostriker 2004; Sokasian et al. 2004; Somerville & Livio 2003; Wyithe & Loeb 2003; Iliev et al. 2005). Page et al. (2007) provides a detailed discussion of the new polarization data: while the best-fit value for τ has not changed significantly, the new EE data, combined with an improved treatment of the TE data, imply smaller marginalized maximum-likelihood value. The 3 year data favor $\tau \simeq 0.1$, consistent with the predictions of a number of simulations of ΛCDM models. For example, Ciardi et al. (2003) ΛCDM simulations predict $\tau = 0.104$ for parameters consistent with the *WMAP* primordial power spectrum. Tumlinson et al. (2004) use the nucleosynthetic data to derive and construct an initial mass function (IMF) for reionization and find $\tau \sim 0.1$. Chiu et al. (2003) found that their joint analysis of the *WMAP* and SDSS quasar data favored a model with $\tau = 0.11$, $\sigma_8 = 0.83$, and $n = 0.96$, very close to our new best-fit values. Wyithe & Cen (2006) predict that if the product of star formation efficiency and escape fraction for Population III stars is comparable to that for Population II stars, $\tau = 0.09$–0.12 with reionization histories characterized by an extended ionization plateau from $z = 7$–12. They argue that this result holds regardless of the redshift where the intergalactic medium (IGM) becomes enriched with metals.

Measurements of the EE and TE power spectrum are a powerful probe of early star formation and an important complement to other astronomical measurements. Observations of galaxies (Malhotra & Rhoads 2004), quasars (Fan et al. 2006), and gamma-ray bursts (Totani et al. 2006) imply that the universe was mostly

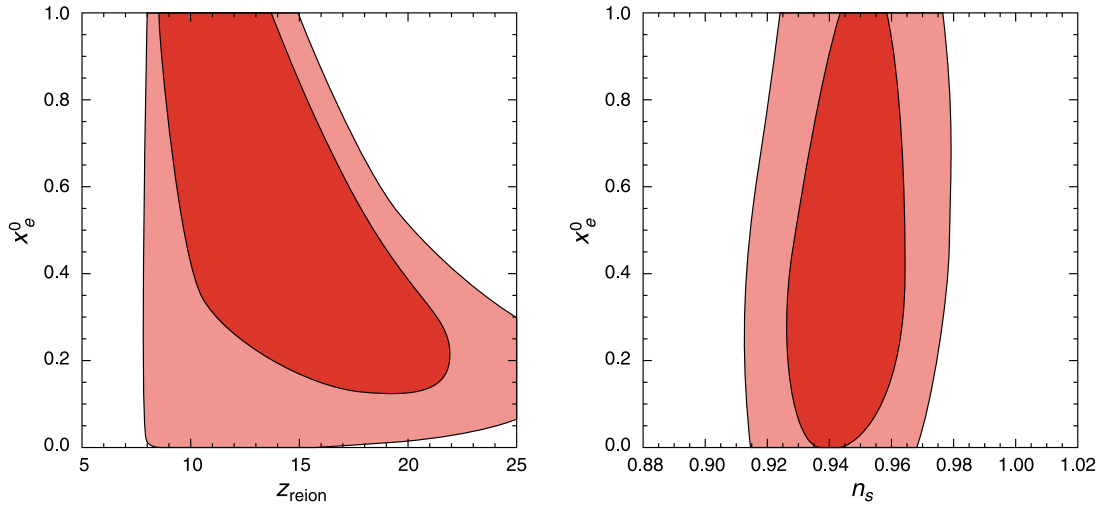

FIG. 3.—*WMAP* constraints on the reionization history. (*Left*) The 68% and 95% joint 2D marginalized confidence level contours for $x_e^0 - z_{\rm reion}$ for a power-law Λ cold dark matter (ΛCDM) model with the reionization history described by eq. (3) and fitted to the *WMAP* 3 year data. In eq. (3) we assume that the universe was partially reionized at $z_{\rm reion}$ to an ionization fraction of x_e^0 and then became fully ionized at $z = 7$. (*Right*) The 68% and 95% joint 2D marginalized confidence level contours for $x_e^0 - n_s$. This figure shows that x_e^0 and n_s are nearly independent for a given value of τ, indicating that *WMAP* determinations of cosmological parameters are not affected by details of the reionization history. Note that we assume a uniform prior on $z_{\rm reion}$ in this calculation, which favors models with lower x_e^0 values in the right panel.

ionized by $z = 6$. The detection of large-scale TE and EE signal (Page et al. 2007) implies that the universe was mostly reionized at even higher redshift. CMB observations have the potential to constrain some of the details of reionization, as the shape of the CMB EE power spectrum is sensitive to reionization history (Kaplinghat et al. 2003; Hu & Holder 2003). Here we explore the ability of the current EE data to constrain reionization by postulating a two-stage process as a toy model. During the first stage, the universe is partially reionized at redshift $z_{\rm reion}$ and complete reionization occurs at $z = 7$:

$$x_e = \begin{cases} 0, & z > z_{\rm reion}, \\ x_e^0, & z_{\rm reion} > z > 7, \\ 1, & z < 7. \end{cases} \quad (3)$$

We have modified CAMB to include this reionization history.

Figure 3 shows the likelihood surface for x_e^0 and $z_{\rm reion}$. The plot shows that the data do not yet constrain x_e^0 and that the characteristic redshift of reionization is sensitive to our assumptions about reionization. If we assume that the universe is fully reionized, $x_e^0 = 1$, then the maximum-likelihood peak is $z_{\rm reion} = 11.3$. The maximum-likelihood peak value of the cosmic age at the reionization epoch is $t_{\rm reion} = 365$ Myr.

Reionization alters the TT power spectrum by suppressing fluctuations on scales smaller than the horizon size at the epoch of reionization. Without strong constraints from polarization data on τ, there is a strong degeneracy between spectral index and τ in likelihood fits (Spergel et al. 2003). The polarization measurements now strongly constrain τ; however, there is still significant uncertainty in x_e and the details of the reionization history. Fortunately, the temperature power spectrum mostly depends on the amplitude of the optical depth signal, τ, so that the other fit parameters (e.g., n_s) are insensitive to the details of the reionization history (see Fig. 3). Because of this weak correlation, we will assume a simple reionization history ($x_e^0 = 1$) in all of the other analysis in this paper. Allowing for a more complex history is not likely to alter any of the conclusions of the other sections.

3.3. *How Many Parameters Do We Need to Fit the WMAP Data?*

In this subsection, we compare the power-law ΛCDM to other cosmological models. We consider both simpler models with fewer parameters and models with additional physics, characterized by additional parameters. We quantify the relative goodness of fit of the models,

$$\Delta\chi^2_{\rm eff} \equiv -\Delta(2\ln\mathcal{L}) = 2\ln\mathcal{L}(\Lambda{\rm CDM}) - 2\ln\mathcal{L}({\rm model}). \quad (4)$$

A positive value for $\Delta\chi^2_{\rm eff}$ implies the model is disfavored. A negative value means that the model is a better fit. We also characterize each model by the number of free parameters, $N_{\rm par}$. There are 3162 degrees of freedom in the combination of T, Q, and U maps and high-l TT and TE power spectra used in the fits and 1448 independent C_l values, so that the effective number of data degrees of freedom is between 1448 and 3162.

Table 3 shows that the power-law ΛCDM is a significantly better fit than the simpler models. For consistency, all of the models are computed with the $N_{\rm side} = 8$ likelihood code and the higher value of the point source amplitude. If we reduce the number of parameters in the model, the cosmological fits significantly worsen:

1. Cold dark matter serves as a significant forcing term that changes the acoustic peak structure. Alternative gravity models (e.g., MOND), and all baryons-only models, lack this forcing term so they predict a much lower third peak than is observed by *WMAP* and small-scale CMB experiments (McGaugh 2004; Skordis et al. 2006). Models without dark matter (even if we allow for a cosmological constant) are very poor fits to the data.

2. Positively curved models without a cosmological constant are consistent with the *WMAP* data alone: a model with the same six parameters and the prior that there is no dark energy, $\Omega_\Lambda = 0$, fits as well as the standard model with the flat universe prior, $\Omega_m + \Omega_\Lambda = 1$. However, if we imposed a prior that $H_0 > 40$ km s^{-1} Mpc^{-1}, then the *WMAP* data would not be consistent with $\Omega_\Lambda = 0$. Moreover, the parameters fitted to the no-cosmological-constant model, ($H_0 = 30$ km s^{-1} Mpc^{-1} and

TABLE 3
GOODNESS OF FIT, $\Delta\chi^2_{\rm eff} \equiv -2 \ln \mathcal{L}$, FOR *WMAP* DATA ONLY RELATIVE TO A POWER-LAW ΛCDM MODEL

Model Number	Model	$-\Delta(2 \ln \mathcal{L})$	$N_{\rm par}$
M1	Scale-invariant fluctuations ($n_s = 1$)	6	5
M2	No reionization ($\tau = 0$)	7.4	5
M3	No dark matter ($\Omega_c = 0$, $\Omega_\Lambda \neq 0$)	248	6
M4	No cosmological constant ($\Omega_c \neq 0$, $\Omega_\Lambda = 0$)	0	6
M5	Power law ΛCDM	0	6
M6	Quintessence ($w \neq -1$)	0	7
M7	Massive neutrino ($m_\nu > 0$)	−1	7
M8	Tensor modes ($r > 0$)	0	7
M9	Running spectral index ($dn_s/d \ln k \neq 0$)	−4	7
M10	Nonflat universe ($\Omega_k \neq 0$)	−2	7
M11	Running spectral index and tensor modes	−4	8
M12	Sharp cutoff	−1	7
M13	Binned $\Delta^2_{\mathcal{R}}(k)$	−22	20

NOTE.—A worse fit to the data is $\Delta\chi^2_{\rm eff} > 0$.

$\Omega_m = 1.3$) are terrible fits to a host of astronomical data: large-scale structure observations, supernova data, and measurements of local dynamics. As discussed in § 7.3, the combination of *WMAP* data and other astronomical data solidifies the evidence against these models. The detected cross-correlation between CMB fluctuations and large-scale structure provides further evidence for the existence of dark energy (see § 4.1.10).

3. The simple scale-invariant ($n_s = 1.0$) model is no longer a good fit to the *WMAP* data. As discussed in the previous subsection, combining the *WMAP* data with other astronomical data sets further strengthens the case for $n_s < 1$.

The conclusion that the *WMAP* data demands the existence of dark matter and dark energy is based on the assumption that the primordial power spectrum is a power-law spectrum. By adding additional features in the primordial perturbation spectrum, these alternative models may be able to better mimic the ΛCDM model. This possibility requires further study.

The bottom half of Table 3 lists the relative improvement of the generalized models over the power-law ΛCDM. As the table shows, the *WMAP* data alone do not require the existence of tensor modes, quintessence, or modifications in neutrino properties. Adding these parameters does not improve the fit significantly. For the *WMAP* data, the region in likelihood space where ($r = 0$, $w = -1$, and $m_\nu = 0$ lies within the 1 σ contour. In § 7, we consider the limits on these parameters based on *WMAP* data and other astronomical data sets.

If we allow for a nonflat universe, then models with small negative Ω_k are a better fit than the power-law ΛCDM model. These models have a lower intervening Sachs-Wolfe (ISW) signal at low l and are a better fit to the low-l multipoles. The best-fit closed universe model has $\Omega_m = 0.415$, $\Omega_\Lambda = 0.630$, and $H_0 = 55$ kms^{-1} Mpc^{-1} and is a better fit to the *WMAP* data alone than the flat universe model($\Delta\chi^2_{\rm eff} = 2$) However, as discussed in § 7.3, the combination of *WMAP* data with either SNe data, large-scale structure data, or measurements of H_0 favors models with Ω_K close to 0.

In § 5, we consider several different modifications to the shape of the power spectrum. As noted in Table 3, none of the modifications lead to significant improvements in the fit. Allowing the spectral index to vary as a function of scale improves the goodness of fit. The low-l multipoles, particularly $l = 2$, are lower than predicted in the ΛCDM model. However, the relative improvement in fit is not large, $\Delta\chi^2_{\rm eff} = 3$, so the *WMAP* data alone do not require a running spectral index.

Measurement of the goodness of fit is a simple approach to test the needed number of parameters. These results should be confirmed by Bayesian model comparison techniques (Beltrán et al. 2005; Trotta 2007; Mukherjee et al. 2006; Bridges et al. 2006). Bayesian methods, however, require an estimate of the number of data points in the fit. It is not clear whether we should use the $\sim 10^{10}$ points in the TOD, the 10^6 points in the temperature maps, the 3×10^3 points in the TT, TE, or EE power spectrum, or the $\sim 10-20$ numbers needed to fit the peaks and valleys in the TT data in evaluating the significance of new parameters.

4. *WMAP* ΛCDM MODEL AND OTHER ASTRONOMICAL DATA

In this paper, our approach is to show first that a wide range of astronomical data sets are consistent with the predictions of the ΛCDM model with its parameters fitted to the *WMAP* data (see § 4.1). We then use the external data sets to constrain extensions of the standard model.

In our analyses, we consider several different types of data sets. We consider the SDSS LRGs, the SDSS full sample, and the 2dFGRS data separately; this allows a check of systematic effects. We divide the small-scale CMB data sets into low-frequency experiments (CBI, VSA) and high-frequency experiments (BOOMERANG, ACBAR). We divide the supernova data sets into two groups as described below. The details of the data sets are also described in § 4.1.

When we consider models with more parameters, there are significant degeneracies, and external data sets are essential for parameter constraints. We use this approach in § 4.2 and subsequent sections.

4.1. *Predictions from the WMAP Best-Fit ΛCDM Model*

The *WMAP* data alone are now able to accurately constrain the basic six parameters of the ΛCDM model. In this section, we focus on this model and begin by using only the *WMAP* data to fix the cosmological parameters. We then use the Markov chains (and linear theory) to predict the amplitude of fluctuations in the local universe and compare to other astronomical observations. These comparisons test the basic physical assumptions of the ΛCDM model.

4.1.1. *Age of the Universe and H_0*

The CMB data do not directly measure H_0; however, by measuring $\Omega_m H_0^2$ through the height of the peaks and the conformal

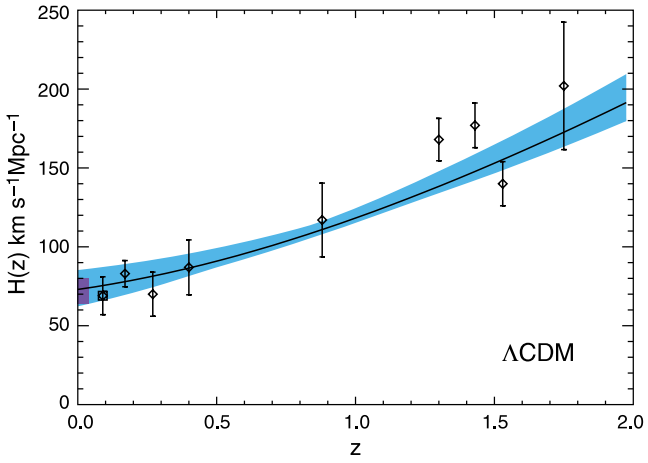

FIG. 4.—ΛCDM model fit to the *WMAP* data predicts the Hubble parameter redshift relation. The blue band shows the 68% confidence interval for the Hubble parameter, H. The dark blue rectangle shows the *HST* Key Project estimate for H_0 and its uncertainties (Freedman et al. 2001). The other points are from measurements of the differential ages of galaxies, based on fits of synthetic stellar population models to galaxy spectroscopy. The squares show values from Jimenez et al. (2003) analyses of SDSS galaxies. The diamonds show values from the Simon et al. (2005) analysis of a high-redshift sample of red galaxies.

distance to the surface of last scatter through the peak positions (Page et al. 2003b), the CMB data produce a determination of H_0 *if we assume the simple flat ΛCDM model*. Within the context of the basic model of adiabatic fluctuations, the CMB data provide a relatively robust determination of the age of the universe as the degeneracy in other cosmological parameters is nearly orthogonal to measurements of the age (Knox et al. 2001; Hu et al. 2001).

The *WMAP* ΛCDM best-fit value for the age, $t_0 = 13.73^{+0.16}_{-0.15}$ Gyr, agrees with estimates of ages based on globular clusters (Chaboyer & Krauss 2002) and white dwarfs (Hansen et al. 2004; Richer et al. 2004). Figure 4 compares the predicted evolution of $H(z)$ to the *HST* Key Project value (Freedman et al. 2001) and to values from analysis of differential ages as a function of redshift (Jimenez et al. 2003; Simon et al. 2005).

The *WMAP* best-fit value, $H_0 = 73.2^{+3.1}_{-3.2}$ km s^{-1} Mpc^{-1}, is also consistent with *HST* measurements (Freedman et al. 2001), $H_0 = 72 \pm 8$ km s^{-1} Mpc^{-1}, where the error includes random and systematic uncertainties and the estimate is based on several different methods (Type Ia supernovae, Type II supernovae, surface brightness fluctuations, and fundamental plane). It also agrees with detailed studies of gravitationally lensed systems such as B1608+656 (Koopmans et al. 2003), which yields 75^{+7}_{-6} km s^{-1} Mpc^{-1}, measurements of the Hubble constant from SZ and X-ray observations of clusters (Bonamente et al. 2006) that find $H_0 = 76^{+3.9}_{-3.4}{}^{+10.0}_{-8.0}$ km s^{-1} Mpc^{-1}, and recent measurements of the Cepheid distances to nearby galaxies that host Type Ia supernova (Riess et al. 2005), $H_0 = 73 \pm 4 \pm 5$ km s^{-1} Mpc^{-1}.

4.1.2. *Big Bang Nucleosynthesis*

Measurements of the light element abundances are among the most important tests of the standard big bang model. The *WMAP* estimate of the baryon abundance depends on our understanding of acoustic oscillations 300,000 years after the big bang. The BBN abundance predictions depend on our understanding of physics in the first minutes after the big bang.

Table 4 lists the primordial deuterium abundance, $y_D^{\rm FIT}$, the primordial ^{3}He abundance, y_3, the primordial helium abundance, Y_P, and the primordial ^{7}Li abundance, $y_{\rm Li}$, based on analytical fits to the predicted BBN abundances (Kneller & Steigman 2004) and the power-law ΛCDM 68% confidence range for the baryon/photon ratio, $\eta_{10} = (273.9 \pm 0.3)\Omega_b h^2$. The lithium abundance is often expressed as a logarithmic abundance, $[{\rm Li}]_P = 12 + \log_{10}({\rm Li/H})$.

TABLE 4

PRIMORDIAL ABUNDANCES BASED ON USING THE STEIGMAN (2005) FITTING FORMULA FOR THE ΛCDM 3 yr *WMAP* ONLY VALUE FOR THE BARYON/PHOTON RATIO, $\eta_{10} = 6.116^{+0.197}_{-0.249}$

Abundance	CMB-based BBN Prediction	Observed Value
$10^5 y_D^{\rm FIT}$	$2.57^{+0.17}_{-0.13}$	1.6–4.0
$10^5 y_3$	$1.05 \pm 0.03 \pm 0.03$ (syst.)	$<1.1 \pm 0.2$
Y_P	$0.24819^{+0.00029}_{-0.00040} \pm 0.0006$(syst.)	0.232–0.258
[Li]	2.64 ± 0.03	2.2–2.4

The systematic uncertainties in the helium abundances are due to the uncertainties in nuclear parameters, particularly neutron lifetime (Steigman 2005). Prior to the measurements of the CMB power spectrum, uncertainties in the baryon abundance were the biggest source of uncertainty in CMB predictions. Serebrov et al. (2005) argues that the currently accepted value, $\tau_n = 887.5$ s, should be reduced by 7.2 s, a shift of several times the reported errors in the Particle Data Book. This (controversial) shorter lifetime lowers the predicted best-fit helium abundance to $Y_P = 0.24675$ (Mathews et al. 2005; Steigman 2005).

The deuterium abundance measurements provide the strongest test of the predicted baryon abundance. Kirkman et al. (2003) estimate a primordial deuterium abundance, $[{\rm D}]/[{\rm H}] = 2.78^{+0.44}_{-0.38} \times 10^{-5}$, based on five QSO absorption systems. The six systems used in the Kirkman et al. (2003) analysis show a significant range in abundances: $(1.65–3.98) \times 10^{-5}$ and have a scatter much larger than the quoted observational errors. Recently, Crighton et al. (2004) report a deuterium abundance of $1.6^{+0.5}_{-0.4} \times 10^{-5}$ for PKS 1937−1009. Because of the large scatter, we quote the range in [D]/[H] abundances in Table 4; however, note that the mean abundance is in good agreement with the CMB prediction.

It is difficult to directly measure the primordial ^{3}He abundance. Bania et al. (2002) quote an upper limit on the primordial ^{3}He abundance of $y_3 < 1.1 \pm 0.2 \times 10^{-5}$. This limit is compatible with the BBN predictions.

Olive & Skillman (2004) have reanalyzed the estimates of primordial helium abundance based on observations of metal-poor H II regions. They conclude that the errors in the abundance are dominated by systematic errors and argue that a number of these systematic effects have not been properly included in earlier analyses. In Table 4, we quote their estimate of the allowed range of Y_P. Olive & Skillman (2004) find a representative value of 0.249 ± 0.009 for a linear fit of [O]/[H] to the helium abundance, significantly above earlier estimates and consistent with *WMAP*-normalized BBN.

While the measured abundances of the other light elements appear to be consistent with BBN predictions, measurements of neutral lithium abundance in low-metallicity stars imply values that are a factor of 2 below the BBN predictions: most recent measurements (Charbonnel & Primas 2005; Boesgaard et al. 2005) find an abundance of $[{\rm Li}]_P \simeq 2.2–2.25$. While Meléndez & Ramírez (2004) find a higher value, $[{\rm Li}]_P \simeq 2.37 \pm 0.05$, even this value is still significantly below the BB-predicted value, 2.64 ± 0.03. These discrepancies could be due to systematics in the inferred lithium abundance (Steigman 2005), uncertainties in the stellar temperature scale (Fields et al. 2005), destruction of lithium in an early generation of stars, or the signature of new early universe physics (Coc et al. 2004; Jedamzik 2004; Richard et al.

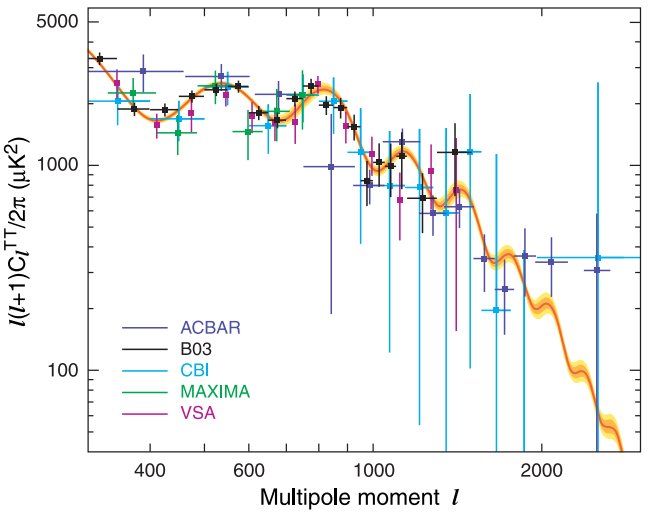

FIG. 5.—Prediction for the small-scale angular power spectrum seen by ground-based and balloon CMB experiments from the ΛCDM model fit to the *WMAP* data only. The colored lines show the best-fit (*red*) and the 68% (*dark orange*) and 95% confidence levels (*light orange*) based on fits of the ΛCDM models to the *WMAP* data. The points in the figure show small-scale CMB measurements (Ruhl et al. 2003; Abroe et al. 2004; Kuo et al. 2004; Readhead et al. 2004a; Dickinson et al. 2004). The plot shows that the ΛCDM model (fit to the *WMAP* data alone) can accurately predict the amplitude of fluctuations on the small scales measured by ground and balloon-based experiments.

2005; Ellis et al. 2005; Larena et al. 2005; Jedamzik et al. 2005). The recent detection (Asplund et al. 2005) of ^{6}Li in several low-metallicity stars further constrains chemical evolution models and exacerbates the tensions between the BBN predictions and observations.

4.1.3. *Small-Scale CMB Measurements*

With the parameters of the ΛCDM model fixed by the measurements of the first three acoustic peaks, the basic properties of the small-scale CMB fluctuations are determined by the assumption of a power law for the amplitude of potential fluctuations and by the physics of Silk damping. We test these assumptions by comparing the *WMAP* best-fit power-law ΛCDM model to data from several recent small-scale CMB experiments (BOOMERANG, MAXIMA, ACBAR, CBI, VSA). These experiments probe smaller angular scales than the *WMAP* experiment and are more sensitive to the details of recombination and the physics of acoustic oscillations. The good agreement seen in Figure 5 suggests that the standard cosmological model is accurately characterizing the basic physics at $z \simeq 1100$.

In subsequent sections, we combine *WMAP* with small-scale experiments. We include four external CMB data sets which complement the *WMAP* observations at smaller scales: the Cosmic Background Imager (CBI; Mason et al. 2003; Sievers et al. 2003; Pearson et al. 2003; Readhead et al. 2004a), the Very Small Array (VSA; Dickinson et al. 2004), the Arcminute Cosmology Bolometer Array Receiver (ACBAR; Kuo et al. 2004), and BOOMERANG (Ruhl et al. 2003; Montroy et al. 2006; Piacentini et al. 2006) We do not include results from a number of experiments that overlap in l range coverage with *WMAP* as these experiments have nontrivial cross-correlations with *WMAP* that would have to be included in the analysis.

We do not use the small-scale polarization results for parameter determination as they do not yet noticeably improve constraints. These polarization measurements, however, already provide important tests on the basic assumptions of the model (e.g., adiabatic fluctuations and standard recombination history).

The measurements beyond the third peak improve constraints on the cosmological parameters. These observations constrict the $\{\tau, \omega_b, A_s, n_s\}$ degeneracy and provide an improved probe of a running tilt in the primordial power spectrum. In each case we only use bandpowers that do not overlap with signal-dominated *WMAP* observations, so that they can be treated as independent measurements.

In the subsequent sections, we perform likelihood analysis for two combinations of *WMAP* data with other CMB data sets: *WMAP* + high-frequency bolometer experiments (ACBAR + BOOMERANG) and *WMAP* + low-frequency radiometer experiments (CBI + VSA). The CBI data set is described in Readhead et al. (2004a). We use seven bandpowers, with mean l-values of 948, 1066, 1211, 1355, 1482, 1692, and 1739, from the even binning of observations rescaled to a 32 GHz Jupiter temperature of 147.3 ± 1.8K. The rescaling reduces the calibration uncertainty to 2.6% from 10% assumed in the first-year analyses; CBI beam uncertainties scale the entire power spectrum and, thus, act like a calibration error. We use a lognormal form of the likelihood as in Pearson et al. (2003). The VSA data (Dickinson et al. 2004) uses five bandpowers with mean l-values of 894, 995, 1117, 1269, and 1407, which are calibrated to the *WMAP* 32 GHz Jupiter temperature measurement. The calibration uncertainty is assumed to be 3%, and again we use a lognormal form of the likelihood. For ACBAR (Kuo et al. 2004), we use the same bandpowers as in the first-year analysis, with central l-values 842, 986, 1128, 1279, 1426, 1580, and 1716, and errors from the ACBAR Web site.[17] We assume a calibration uncertainty of 20% in C_l, and the quoted 3% beam uncertainty in full width at half-maximum. We use the temperature data from the 2003 flight of BOOMERANG, based on the "NA pipeline" (Jones et al. 2006) considering the 7 data points and covariance matrix for bins with mean l-values, 924, 974, 1025, 1076, 1117, 1211, and 1370. While there is overlap between some of the small-scale power spectrum measurements and *WMAP* measurements at $800 < l < 1000$, the *WMAP* measurements are noise-dominated so that there is little covariance between the measurements.

4.1.4. *Large-Scale Structure*

With the *WMAP* polarization measurements constraining the suppression of temperature anisotropy by reionization, we now have an accurate measure of the amplitude of fluctuations at the redshift of decoupling. If the power-law ΛCDM model is an accurate description of the large-scale properties of the universe, then we can extrapolate forward the roughly 1000-fold growth in the amplitude of fluctuations due to gravitational clustering and compare the predicted amplitude of fluctuations to the large-scale structure observations. This is a powerful test of the theory as some alternative models fit the CMB data but predict significantly different galaxy power spectra (e.g., Blanchard et al. 2003).

Using *only* the *WMAP* data, together with linear theory, we can predict the amplitude and shape of the matter power spectrum. The band in Figure 6 shows the 68% confidence interval for the matter power spectrum. Most of the uncertainty in the figure is due to the uncertainties in $\Omega_m h$. The points in the figure show the SDSS Galaxy power spectrum (Tegmark et al. 2004b) with the amplitude of the fluctuations normalized by the galaxy lensing measurements and the 2dFGRS data (Cole et al. 2005). The figure shows that the ΛCDM model, when normalized to observations at

[17] See http://cosmology.berkeley.edu/group/swlh/acbar/data.

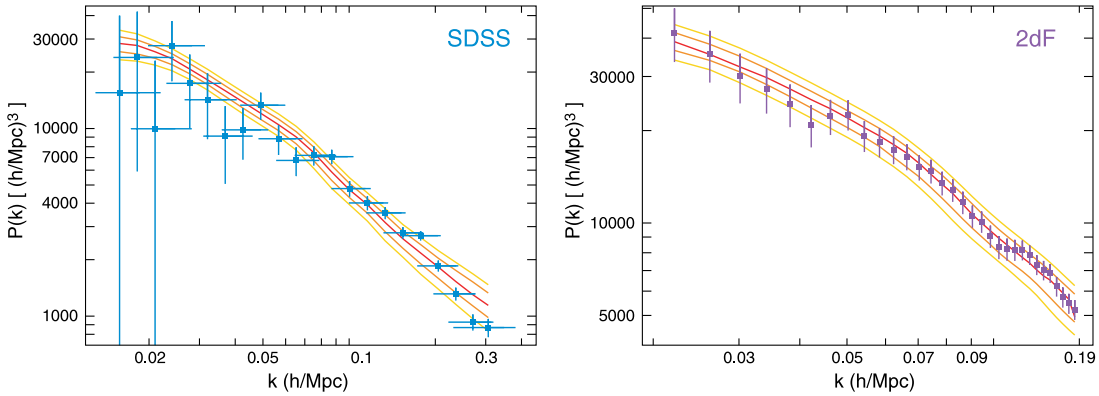

FIG. 6.—*Left*: Predicted power spectrum (based on the range of parameters consistent with the *WMAP*-only parameters) is compared to the mass power spectrum inferred from the SDSS galaxy power spectrum (Tegmark et al. 2004b) as normalized by weak lensing measurements (Seljak et al. 2005b). *Right*: Predicted power spectrum is compared to the mass power spectrum inferred from the 2dFGRS galaxy power spectrum (Cole et al. 2005) with the best-fit value for b_{2dFGRS} based on the fit to the *WMAP* model. Note that the 2dFGRS data points shown are correlated.

$z \sim 1100$, accurately predicts the large-scale properties of the matter distribution in the nearby universe. It also shows that adding the large-scale structure measurements will reduce uncertainties in cosmological parameters.

When we combine *WMAP* with large-scale structure observations in subsequent sections, we consider the measurements of the power spectrum from the two large-scale structure surveys. Since the galaxy power spectrum does not suffer the optical depth-driven suppression in power seen in the CMB, large-scale structure data give an independent measure of the normalization of the initial power spectrum (to within the uncertainty of the galaxy biasing and redshift space distortions) and significantly truncates the $\{\tau, \omega_b, A_s, n_s\}$ degeneracy. In addition, the galaxy power spectrum shape is determined by $\Omega_m h$ as opposed to the $\Omega_m h^2$ dependency of the CMB. Its inclusion therefore further helps to break the $\{\omega_m, \Omega_\Lambda, w, \text{or } \Omega_k\}$ degeneracy.

The 2dFGRS survey probes the universe at redshift $z \sim 0.1$ (we assume $z_{\rm eff} = 0.17$ for the effective redshift for the survey) and probes the power spectrum on scales of $0.022\ h\ \mathrm{Mpc}^{-1} < k < 0.19\ h\ \mathrm{Mpc}^{-1}$. From the data and covariance described in Cole et al. (2005) we use 32 of the 36 bandpowers in the range $0.022\ h\ \mathrm{Mpc}^{-1} < k < 0.19\ h\ \mathrm{Mpc}^{-1}$. We correct for nonlinearities and nonlinear redshift space distortions using the prescription employed by the 2dF team,

$$P_{\rm gal}^{\rm redsh}(k) = \frac{1 + Qk^2}{1 + Ak} P_{\rm gal}^{\rm theory}(k) \qquad (5)$$

where $P_{\rm gal}^{\rm redsh}$ and $P_{\rm gal}^{\rm theory}$ are the redshift space and theoretical real space galaxy power spectra with $Q = 4\ h^{-2}\ \mathrm{Mpc}^2$ and $A = 1.4\ h^{-1}$ Mpc. We analytically marginalize over the power spectrum amplitude, effectively applying no prior on the linear bias and on linear redshift space distortions, in contrast to our first-year analyses.

The SDSS main galaxy survey measures the galaxy distribution at redshift of $z \sim 0.1$; however, as in the analysis of the SDSS team (Tegmark et al. 2004b) we assume $z_{\rm eff} = 0.07$, and we use 14 power spectrum bandpowers between $0.016\ h\ \mathrm{Mpc}^{-1} < k < 0.11\ h\ \mathrm{Mpc}^{-1}$. We follow the approach used in the SDSS analysis in Tegmark et al. (2004a): we use the nonlinear evolution of clustering as described in Smith et al. (2003) and include a linear bias factor, $b_{\rm SDSS}$, and the linear redshift space distortion parameter, β:

$$P_{\rm gal}^{\rm redsh}(k) = \left(1 + \frac{2}{3}\beta + \frac{1}{5}\beta^2\right) P_{\rm gal}^{\rm theory}(k). \qquad (6)$$

Following Lahav et al. (1991) we use $\beta b = d \ln \delta / d \ln a$, where $\beta \approx [\Omega_m^{4/7} + (1 + \Omega_m/2)(\Omega_\Lambda/70)]/b$. We impose a Gaussian prior on the bias of $b = 1.03 \pm 0.15$, based on an estimate from weak lensing of the same SDSS galaxies used to derive the matter power spectrum. This value includes a 4% calibration uncertainty in quadrature with the reported bias error[18] and is a symmetrized form of the bias constraint in Table 2 of Seljak et al. (2005b). While the *WMAP* first-year data were used in the Seljak et al. (2005b) analysis, the covariance between the data sets are small. We restrict our analysis to scales where the bias of a given galaxy population does not show significant scale dependence (Zehavi et al. 2005). Analyses that use galaxy clustering data on smaller scales require detailed modeling of nonlinear dynamics and the relationship between galaxy halos and galaxy properties (see, e.g., Abazajian et al. 2005).

The SDSS luminous red galaxy (LRG) survey uses the brightest class of galaxies in the SDSS survey (Eisenstein et al. 2005). While a much smaller galaxy sample than the main SDSS galaxy sample, it has the advantage of covering $0.72\ h^{-3}\ \mathrm{Gpc}^3$ between $0.16 < z < 0.47$. Because of its large volume, this survey was able to detect the acoustic peak in the galaxy correlation, one of the distinctive predictions of the standard adiabatic cosmological model (Peebles & Yu 1970; Sunyaev & Zel'dovich 1970; Silk & Wilson 1981; Bond & Efstathiou 1984; Vittorio & Silk 1984; Bond & Efstathiou 1987). We use the SDSS acoustic peak results to constrain the balance of the matter content, using the well-measured combination

$$A(z = 0.35) \equiv \left\{\frac{[d_A(z = 0.35)/0.35c]^2}{H(z = 0.35)}\right\}^{1/3} \sqrt{\Omega_m H_0^2}, \qquad (7)$$

where d_A is the comoving angular diameter distance and c is the speed of light. We impose a Gaussian prior of $A = 0.469(n_s/0.98)^{-0.35} \pm 0.017$ based on the analysis of Eisenstein et al. (2005).

4.1.5. *Lyα Forest*

Absorption features in high-redshift quasars (QSO) at around the frequency of the Lyα emission line are thought to be produced by regions of low-density gas at redshifts $2 < z < 4$ (Croft et al. 1998; Gnedin & Hamilton 2002). These features allow the matter distribution to be characterized on scales of

[18] M. Tegmark 2006, private communication.

$0.2\ h\ \mathrm{Mpc}^{-1} < k < 5\ h\ \mathrm{Mpc}^{-1}$ and as such extend the lever arm provided by combining large-scale structure data and CMB. These observations also probe a higher redshift range ($z \sim 2$–3). Thus, these observations nicely complement CMB measurements and large-scale structure observations. While there has been significant progress in understanding systematics in the past few years (McDonald et al. 2005; Meiksin & White 2004), time constraints limit our ability to consider all relevant data sets.

Recent fits to the Lyα forest imply a higher amplitude of density fluctuations: Jena et al. (2005) find that $\sigma_8 = 0.9$, $\Omega_m = 0.27$, $h = 0.71$ provides a good fit to the Lyα data. Seljak et al. (2005a) combines first-year *WMAP* data, other CMB experiments, large-scale structure, and Lyα to find $n_s = 0.98 \pm 0.02$, $\sigma_8 = 0.90 \pm 0.03$, $h = 0.71 \pm 0.021$, and $\Omega_m = 0.281^{+0.023}_{-0.021}$. Note that if they assume $\tau = 0.09$, the best-fit value drops to $\sigma_8 = 0.84$. While these models have somewhat higher amplitudes than the new best-fit *WMAP* values, a recent analysis by Desjacques & Nusser (2005) find that the Lyα data are consistent with σ_8 between 0.7 and 0.9. This suggests that the Lyα data are consistent with the new *WMAP* best-fit values; however, further analysis is needed.

4.1.6. *Galaxy Motions and Properties*

Observations of galaxy peculiar velocities probe the growth rate of structure and are sensitive to the matter density and the amplitude of mass fluctuations. The Feldman et al. (2003) analysis of peculiar velocities of nearby ellipticals and spirals finds $\Omega_m = 0.30^{+0.17}_{-0.07}$ and $\sigma_8 = 1.13^{+0.22}_{-0.23}$, within 1 σ of the *WMAP* best-fit value for Ω_m and 1.5 σ higher than the *WMAP* value for σ_8. These estimates are based on dynamics and are not sensitive to the shape of the power spectrum. Mohayaee & Tully (2005) apply orbit retracing methods to motions in the local supercluster and obtain $\Omega_m = 0.22 \pm 0.02$, consistent with the *WMAP* values.

Modeled galaxy properties can be compared to the clustering properties of galaxies on smaller scales. The best-fit parameters for *WMAP* only are consistent with the recent Abazajian et al. (2005) analysis of the pre–3 year release CMB data combined with the SDSS data. In their analysis, they fit a Halo Occupation Distribution model to the galaxy distribution so as to use the galaxy clustering data at smaller scales. Their best-fit parameters ($H_0 = 70 \pm 2.6$ km s^{-1} Mpc^{-1}, $\Omega_m = 0.271 \pm 0.026$) are consistent with the results found here. Vale & Ostriker (2006) fit the observed galaxy luminosity functions with $\sigma_8 = 0.8$ and $\Omega_m = 0.25$. Van den Bosch et al. (2003) use the conditional luminosity function to fit the 2dFGRS luminosity function and the correlation length as a function of luminosity. Combining with the first-year *WMAP* data, they find $\Omega_m = 0.25^{+0.10}_{-0.07}$ and $\sigma_8 = 0.78 \pm 0.12$ (95% CL), again in remarkable agreement with the three year *WMAP* best-fit values.

4.1.7. *Weak Lensing*

Over the past few years, there has been dramatic progress in using weak lensing data as a probe of mass fluctuations in the nearby universe. Lensing surveys complement CMB measurements (Contaldi et al. 2003; Tereno et al. 2005), and their dominant systematic uncertainties differ from the large-scale structure surveys.

Measurements of weak gravitational lensing, the distortion of galaxy images by the distribution of mass along the line of sight, directly probe the distribution of mass fluctuations along the line of sight (see Refregier 2003 for a recent review). Figure 7 shows that the *WMAP* ΛCDM model predictions for σ_8 and Ω_m are lower than the amplitude found in most recent lensing surveys: Hoekstra et al. (2002) calculate $\sigma_8 = 0.94^{+0.10}_{-0.14}(\Omega_m/0.25)^{-0.52}$ (95% confidence) from the RCS survey, and Van Waerbeke et al. (2005) determine $\sigma_8 = 0.91 \pm 0.08(\Omega_m/0.25)^{-0.49}$ from the VIRMOS-DESCART survey; however, Jarvis et al. (2003) find $\sigma_8 = 0.79^{+0.13}_{-0.16}(\Omega_m/0.25)^{-0.57}$ (95% confidence level) from the 75 Degree CTIO survey.

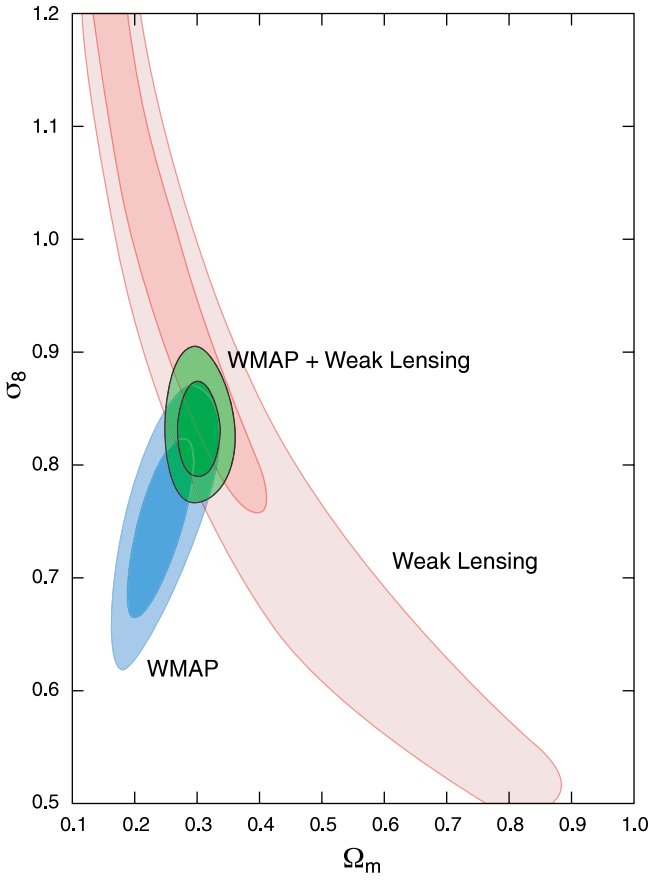

FIG. 7.—Prediction for the mass fluctuations measured by the CFTHLS weak-lensing survey from the ΛCDM model fit to the *WMAP* data only. The blue, red, and green contours show the joint 2D marginalized 68% and 95% confidence limits in the (σ_8, Ω_m) plane for *WMAP* only, CFHTLS only and *WMAP* + CFHTLS, respectively, for the power-law ΛCDM models. All constraints come from assuming the same priors on input parameters, with the additional marginalization over z_s in the weak lensing analysis, using a top-hat prior of $0.613 < z_s < 0.721$. While lensing data favors higher values of $\sigma_8 \simeq 0.8$–1.0 (see § 4.1.7), X-ray cluster studies favor lower values of $\sigma_8 \simeq 0.7$–0.8 (see § 4.1.9).

In § 4.2, we use the data set provided by the first weak gravitational lensing analysis of the Canada-France-Hawaii Telescope Legacy Survey (CFHTLS)[19] as conducted by Hoekstra et al. (2006, hereafter Ho06) and Semboloni et al. (2006). Following Ho06, we use only the wide fields W1 and W3, hence a total area of 22 deg^2 observed in the i' band limited to a magnitude of $i' = 24.5$. We follow the same methodology as Ho06 and Tereno et al. (2005). For each given model and set of parameters, we compute the predicted shear variance at various smoothing scales, $\langle \gamma^2 \rangle$ and then evaluate its likelihood (see Ho06, eq. [13]).

Since the lensing data are in a noise-dominated regime, we neglect the cosmological dependence of the covariance matrix. To account conservatively for a possible residual systematic contamination, we use $\langle \gamma_B^2 \rangle$ as a monitor and add it in quadrature to the diagonal of the noise covariance matrix, as in Ho06. We furthermore marginalize over the mean source redshift, z_s (defined in eq. [16] of Ho06) assuming a uniform prior between 0.613 and 0.721. This marginalization is performed by including these extra

[19] See http://www.cfht.hawaii.edu/Science/CFHTLS.

TABLE 5
ΛCDM Model: Joint Likelihoods

Parameter	*WMAP* Only	*WMAP* + CBI + VSA	*WMAP* + ACBAR + BOOMERANG	*WMAP* + 2dFGRS
$100\Omega_b h^2$	$2.230^{+0.075}_{-0.073}$	2.208 ± 0.071	2.232 ± 0.074	$2.223^{+0.069}_{-0.068}$
$\Omega_m h^2$	$0.1265^{+0.0081}_{-0.0080}$	$0.1233^{+0.0075}_{-0.0074}$	0.1260 ± 0.0081	0.1261 ± 0.0050
h	0.735 ± 0.032	0.742 ± 0.031	$0.739^{+0.033}_{-0.032}$	$0.733^{+0.020}_{-0.021}$
τ	$0.088^{+0.029}_{-0.030}$	0.087 ± 0.029	$0.088^{+0.031}_{-0.032}$	0.083 ± 0.028
n_s	0.951 ± 0.016	0.947 ± 0.015	0.951 ± 0.016	0.948 ± 0.015
σ_8	0.742 ± 0.051	$0.721^{+0.047}_{-0.046}$	$0.739^{+0.050}_{-0.051}$	0.737 ± 0.036
Ω_m	0.237 ± 0.034	0.226 ± 0.031	$0.233^{+0.033}_{-0.034}$	0.236 ± 0.020

Note.—These values are calculated using the $N_{\rm side} = 8$ likelihood code with $A_{PS} = 0.017$.

parameters in the Monte Carlo Markov Chain. Our analysis differs, however, from the likelihood analysis of Ho06 in the choice of the transfer function. We use the Novosyadlyj et al. (1999, hereafter NDL) CDM transfer function (with the assumptions of Tegmark et al. 2001) rather than the Bardeen et al. (1986) CDM transfer function. The NDL transfer function includes more accurately baryon oscillations and neutrino effects. This modification alters the shape of the likelihood surface in the two-dimensional (σ_8, Ω_m) likelihood space.

4.1.8. *Strong Lensing*

Strong lensing provides another potentially powerful probe of cosmology. The number of multiply lensed arcs and quasars is very sensitive to the underlying cosmology. The cross section for lensing depends on the number of systems with surface densities above the critical density, which in turn is sensitive to the angular diameter distance relation (Turner 1990). The CLASS lensing survey (Chae et al. 2002) finds that the number of lenses detected in the radio survey is consistent with a flat universe with a cosmological constant and $\Omega_m = 0.31^{+0.27}_{-0.14}$. The statistics of strong lenses in the SDSS is also consistent with the standard ΛCDM cosmology (Oguri 2004). The number and the properties of lensed arcs are also quite sensitive to cosmological parameters (but also to the details of the data analysis). Wambsganss et al. (2004) conclude that arc statistics are consistent with the concordance ΛCDM model.

Soucail et al. (2004) has used multiple lenses in Abell 2218 to provide another geometrical test of cosmological parameters. They find that $0 < \Omega_m < 0.33$ and $w < -0.85$ for a flat universe with dark energy. This method is another independent test of the standard cosmology.

4.1.9. *Clusters and the Growth of Structure*

The numbers and properties of rich clusters are another tool for testing the emerging standard model. Since clusters are rare, the number of clusters as a function of redshift is a sensitive probe of cosmological parameters. Recent analyses of both optical and X-ray cluster samples yield cosmological parameters consistent with the best-fit *WMAP* ΛCDM model (Borgani et al. 2001; Bahcall & Bode 2003; Allen et al. 2003; Vikhlinin et al. 2003; Henry 2004). The parameters are, however, sensitive to uncertainties in the conversion between observed properties and cluster mass (Pierpaoli et al. 2003; Rasia et al. 2005).

Clusters can also be used to infer cosmological parameters through measurements of the baryon/dark matter ratio as a function of redshift (Pen 1997; Ettori et al. 2003; Allen et al. 2004). Under the assumption that the baryon/dark matter ratio is constant with redshift, the universe is flat, and standard baryon densities, Allen et al. (2004) find $\Omega_m = 0.24 \pm 0.04$ and $w = -1.20^{+0.24}_{-0.28}$. Voevodkin & Vikhlinin (2004) determine $\sigma_8 = 0.72 \pm 0.04$ and $\Omega_m h^2 = 0.13 \pm 0.07$ from measurements of the baryon fraction. These parameters are consistent with the values found here and in § 7.1.

4.1.10. *Integrated Sachs-Wolfe (ISW) Effect*

The ΛCDM model predicts a statistical correlation between CMB temperature fluctuations and the large-scale distribution of matter (Crittenden & Turok 1996). Several groups have detected correlations between the *WMAP* measurements and various tracers of large-scale structure at levels consistent with the concordance ΛCDM model (Boughn & Crittenden 2004, 2005; Nolta et al. 2004; Afshordi et al. 2004; Scranton et al. 2003; Fosalba & Gaztañaga 2004; Padmanabhan et al. 2005; Corasaniti et al. 2005; Vielva et al. 2006). These detections provide an important independent test of the effects of dark energy on the growth of structure. However, the first-year *WMAP* data are already signal-dominated on the scales probed by the ISW effect, thus, improved large-scale structure surveys are needed to improve the statistical significance of this detection (Afshordi 2004; Bean & Dore 2004; Pogosian et al. 2005).

4.1.11. *Supernova*

With the realization that their light curve shapes could be used to make SN Ia into standard candles, supernovae have become an important cosmological probe (Phillips 1993; Hamuy et al. 1996; Riess et al. 1996). They can be used to measure the luminosity distance as a function of redshift. The dimness of $z \approx 0.5$ supernova provide direct evidence for the accelerating universe (Riess et al. 1998; Schmidt et al. 1998; Perlmutter et al. 1999; Tonry et al. 2003; Knop et al. 2003; Nobili et al. 2005; Clocchiatti et al. 2006; Krisciunas et al. 2005; Astier et al. 2005). Recent *HST* measurements (Riess et al. 2004) trace the luminosity distance/redshift relation out to higher redshift and provide additional evidence for presence of dark energy. Assuming a flat universe, the Riess et al. (2004) analysis of the supernova data alone finds that $\Omega_m = 0.29^{+0.05}_{-0.03}$, consistent with the fits to *WMAP* data alone (see Table 2) and to various combinations of CMB and LSS data sets (see Tables 5 and 6). Astier et al. (2005) find that $\Omega_m = 0.263^{+0.042}_{-0.042}(\text{stat.})^{+0.032}_{-0.032}(\text{sys.})$ from the first-year supernova legacy survey.

Within the ΛCDM model, the supernovae data serve as a test of our cosmological model. Figure 8 shows the consistency between the supernova and CMB data. Using just the *WMAP* data and the ΛCDM model, we can predict the distance/luminosity relationship and test it with the supernova data.

In § 4.2 and subsequent sections, we consider two recently published high-z supernovae data sets in combination with the *WMAP* CMB data: the first sample is 157 supernova in the "Gold Sample" as described in Riess et al. (2004) with $0.015 < z < 1.6$ based on a combination of ground-based data and the GOODS

TABLE 6
ΛCDM MODEL

Parameter	*WMAP* + SDSS	*WMAP* + LRG	*WMAP* + SNLS	*WMAP* + SNGold	*WMAP* + CFHTLS
$100\Omega_b h^2$	$2.230^{+0.071}_{-0.070}$	$2.242^{+0.069}_{-0.070}$	$2.234^{+0.075}_{-0.074}$	$2.230^{+0.069}_{-0.072}$	2.255 ± 0.067
$\Omega_m h^2$	$0.1327^{+0.0063}_{-0.0064}$	0.1336 ± 0.0049	0.1293 ± 0.0059	$0.1349^{+0.0061}_{-0.0060}$	0.1409 ± 0.0038
h	0.710 ± 0.026	$0.709^{+0.019}_{-0.018}$	0.724 ± 0.023	0.701 ± 0.021	0.687 ± 0.018
τ	$0.080^{+0.029}_{-0.030}$	0.082 ± 0.029	0.085 ± 0.030	$0.079^{+0.030}_{-0.029}$	$0.088^{+0.028}_{-0.027}$
n_s	$0.948^{+0.016}_{-0.015}$	0.951 ± 0.016	$0.950^{+0.016}_{-0.017}$	0.946 ± 0.016	0.953 ± 0.016
σ_8	$0.772^{+0.040}_{-0.041}$	0.780 ± 0.036	0.758 ± 0.041	$0.784^{+0.042}_{-0.041}$	$0.827^{+0.026}_{-0.025}$
Ω_m	0.265 ± 0.030	$0.266^{+0.020}_{-0.021}$	$0.248^{+0.024}_{-0.025}$	0.276 ± 0.026	0.300 ± 0.021

ACS Treasury program using *HST*, and the second sample is 115 supernova in the range $0.015 < z < 1$ from the Supernova Legacy Survey (SNLS; Astier et al. 2005).

Measurements of the apparent magnitude, m, and inferred absolute magnitude, M_0, of each SN have been used to derive the distance modulus $\mu_{\rm obs} = m - M_0$, from which a luminosity distance is inferred, $\mu_{\rm obs} = 5 \log [d_L(z)/{\rm Mpc}] + 25$. The luminosity distance predicted from theory, $\mu_{\rm th}$, is compared to observations using a χ^2 analysis summing over the SN sample:

$$\chi^2 = \sum_i \frac{\left[\mu_{{\rm obs},i}(z_i) - \mu_{\rm th}(z_i, M_0)\right]^2}{\sigma^2_{{\rm obs},i}}, \quad (8)$$

where the absolute magnitude, M_0, is a "nuisance parameter," analytically marginalized over in the likelihood analysis (Lewis & Bridle 2002), and $\sigma_{\rm obs}$ contains systematic errors related to the light curve stretch factor, K-correction, extinction, and the intrinsic redshift dispersion due to SNe peculiar velocities (assumed 400 and 300 km s^{-1} for *HST*/GOODS and SNLS data sets, respectively).

4.2. *Joint Constraints on ΛCDM Model Parameters*

In the previous section we showed that the power-law LCDM model fit to *WMAP* data only is consistent with other astronomical data. Motivated by this stringent series of cosmological tests, we combine the *WMAP* data with other astronomical observations to further constrain cosmological parameters.

Tables 5 and 6 show that adding external data sets has little effect on several parameters: $\Omega_b h^2$, n_s, and τ. However, the various combinations do reduce the uncertainties on Ω_m and the amplitude of fluctuations. The data sets used in Table 5 favor smaller values of the matter density, higher Hubble constant values, and lower values of σ_8. The data sets used in Table 6 favor higher values of Ω_m, lower Hubble constants, and higher values of σ_8. The lensing data are most discrepant and it most strongly pulls the combined results toward higher amplitudes and higher Ω_m (see Figs. 7 and 9). The overall effect of combining the data sets is shown in Figure 10.

The best fits shown in Table 6 differ by about 1 σ from the best fits shown in Table 5 in their predictions for the total matter density, $\Omega_m h^2$ (See Tables 5 and 6 and Fig. 9). More accurate measurements of the third peak will help resolve these discrepancies.

The differences between the two sets of data may be due to statistical fluctuations. For example, the SDSS main galaxy sample power spectrum differs from the power spectrum measured from the 2dfGRS: this leads to a lower value for the Hubble constant for the *WMAP* + SDSS data combination, $h = 0.710 \pm 0.026$, than for *WMAP* + 2dFGRS, $h = 0.733^{+0.020}_{-0.021}$. Note that while the SDSS LRG data parameters values are close to those from the main SDSS catalog, they are independent determinations with mostly different systematics.

Lensing measurements are sensitive to the amplitude of the local potential fluctuations, which scale roughly as $\sigma_8 \Omega_m^{0.6}$, so that lensing parameter constraints are nearly orthogonal to the CMB degeneracies (Tereno et al. 2005). The CFHTLS lensing data best-fit value for $\sigma_8 \Omega_m^{0.6}$ is 1–2 σ higher than the best-fit three year *WMAP* value. As a result, the combination of CFHT and *WMAP* data favors a higher value of σ_8 and Ω_m and a lower value of H_0 than *WMAP* data alone. Appendix A shows that the amplitude of this discrepancy is somewhat sensitive to our choice of priors. Because of the small error bars in the CFHT data set and the relatively small overlap region in parameter space, the CFHT data set has a strong influence on cosmological parameters. Because of the small errors in the CFHT data and the relatively small overlap region in parameter space, the CFHT data have a strong influence on cosmological parameters. This effect is exacerbated when additional cosmological data sets are included in the analysis. Because

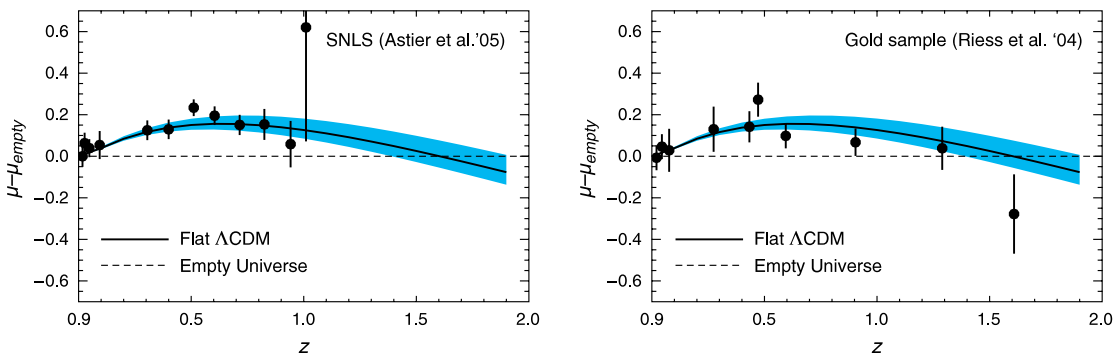

FIG. 8.—Using the *WMAP* ΛCDM parameters, we predict luminosity distance-redshift relationship and compare it to measurements from supernova surveys. The plots show the deviations of the distance measure (DM) from the empty universe model. The solid lines represent the best *WMAP* ΛCDM parameters, and the blue band shows the 68% confidence range. (*Left*) SNLS data (Astier et al. 2005). (*Right*) "Gold" supernova data (Riess et al. 2004).

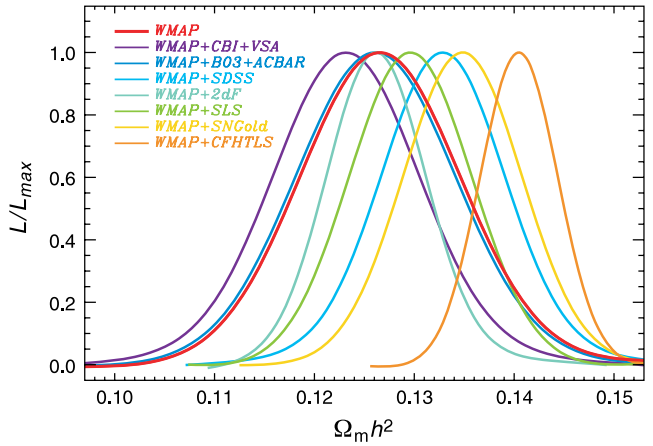

FIG. 9.—One-dimensional marginalized distribution of $\Omega_m h^2$ for *WMAP*, *WMAP* + CBI + VSA, *WMAP* + BOOM + ACBAR, *WMAP* + SDSS, *WMAP* + SN(SNLS), *WMAP* + SN(*HST*/GOODS), *WMAP* + 2dFGRS, and *WMAP* + CFHTLS for the power-law ΛCDM model.

of this, we do not include the lensing data in the full combined data set (*WMAP*. . . *WMAP* + ALL), rather we quote *WMAP* + CFHT results separately. The combined data sets place the strongest limits on cosmological parameters. Because they are based on the overlap between many likelihood functions, limits based on the *WMAP* + ALL data set should be treated with some caution. Figure 10 shows the two-dimensional marginalized likelihood surface for both *WMAP* only and for the combination of *WMAP* + ALL.

5. CONSTRAINING THE SHAPE OF THE PRIMORDIAL POWER SPECTRUM

While the simplest inflationary models predict that the spectral index varies slowly with scale, inflationary models can produce strong scale-dependent fluctuations (see e.g., Kawasaki et al. 2003; Hall et al. 2004; Yamaguchi & Yokoyama 2004). The first-year *WMAP* observations provided some motivation for considering these models as the data, particularly when combined with the Lyα forest measurements, were better fitted by models with a running spectral index (Spergel et al. 2003). Small-scale CMB measurements (Readhead et al. 2004a) also favor running spectral index models over power-law models.

Here we consider whether a more general function for the primordial power spectrum could better fit the new *WMAP* data. We consider three forms for the power spectrum:

1. $\Delta^2_{\mathcal{R}}(k)$ with a running spectral index: $1 + d\ln\Delta^2_R(k)/d\ln k = n(k_0) + dn_s/d\ln(k)\ln(k/k_0)$.
2. $\Delta^2_{\mathcal{R}}(k)$ allowed to freely vary in 15 bins in k-space, with $k_1 = 0$, $k_2 = 0.001$ Mpc^{-1}, $k_{15} = 0.15$ Mpc^{-1}, $k_{i+1} = 1.47k_i$ for $3 \le i \le 14$. $\Delta^2_{\mathcal{R}}(k)$ is given by linear interpolation within the bins and $\Delta^2_{\mathcal{R}}(k) = \Delta^2_{\mathcal{R}}(0.15/\mathrm{Mpc})$ for $k > 0.15$/Mpc.
3. $\Delta^2_{\mathcal{R}}(k)$ with a sharp k cutoff at $k = k_c$,

$$\Delta^2_{\mathcal{R}}(k) = 0, \qquad k \le k_c,$$
$$\Delta^2_{\mathcal{R}}(k) \propto \left(\frac{k}{k_0}\right)^{(n_s-1)}, \qquad k > k_c, \tag{9}$$

Figure 11 shows how *WMAP* data alone can be used to reconstruct the primordial power spectrum as a function of scale, parameterized by logarithmically spaced bins out to $k = 0.15$ Mpc^{-1}. Even allowing for these additional degrees of freedom, the data prefer a nearly featureless power-law power spectrum.

The deviation of the primordial power spectrum from a simple power law can be most simply characterized by a sharp cutoff in the primordial spectrum. Analysis of this model finds that putting in a cutoff of $k_c \sim 3 \times 10^{-4}$ Mpc improves the fit by $\Delta\chi^2 = 1.2$, not enough to justify a radical change in the primordial spectrum.

Table 3 demonstrates that, while models with reduced large-scale power provide slightly improved fits to the CMB data, the improvements do not warrant additional parameters.

5.1. *External Data Sets and the Running Spectral Index*

The uncertainties in the measurements of running is slightly improved by including the small-scale experiments. For models with only scalar fluctuations, the marginalized value for the derivative of the spectral index is $dn_s/d\ln k = -0.055^{+0.030}_{-0.031}$ for *WMAP* only, $dn_s/d\ln k = -0.066^{+0.029}_{-0.028}$ for the *WMAP* + CBI + VSA data, and $dn_s/d\ln k = -0.058 \pm 0.029$ for *WMAP* + BOOM + ACBAR. For models with tensors, $dn_s/d\ln k = -0.085 \pm 0.043$ for *WMAP* only, $dn_s/d\ln k = -0.090^{+0.038}_{-0.039}$ for *WMAP* + CBI + VSA, and $dn_s/d\ln k = -0.082 \pm 0.040$ for *WMAP* + BOOM + ACBAR. As Figure 12 shows, models with negative running allow large tensor amplitudes; thus, when we marginalize over r with a flat prior, these models favor a more negative running.

Figure 13 shows that both the power-law ΛCDM model and the running spectral index model fit the CMB data. At present, the small-scale data do not yet clearly distinguish the two models.

A large absolute value of running would be problematic for most inflationary models, so further testing of this suggestive trend is important for our understanding of early universe physics. Additional *WMAP* data and upcoming, more sensitive small-scale CMB data will further test deviations from scale invariance. Current large-scale structure data do not strengthen the case for running because these data sets probe similar physical scales to the *WMAP* experiment. Figure 12 shows that current data favor a large running; however, the evidence is not yet compelling. The constraints from *WMAP* + lensing and *WMAP* + 2dFGRS are similar to the *WMAP* + SDSS constraints shown in Figure 12.

5.2. *Is the Power Spectrum Featureless?*

Since inflation magnifies fluctuations that were once on sub-Planckian scales to scales of the observable horizon, trans-Planckian physics could potentially leave its imprint on the CMB sky. Over the past few years, there has been significant interest in the possibility of detecting the signature of trans-Planckian physics in the angular power spectrum. Several studies (Martin & Brandenberger 2001, 2003; Danielsson 2002; Easther et al. 2002; Bergström & Danielsson 2002; Kaloper et al. 2002; Martin & Ringeval 2004; Burgess et al. 2003; Schalm et al. 2004) have discussed the possible form and the expected amplitude of the trans-Planckian effects that might modify the spectrum coming from slow roll inflation. The scalar power spectra resulting from power-law (PL) slow roll inflation can be written in the terms of Hubble Flow parameters, respectively, as (Leach & Liddle 2003)

$$\Delta^2_{\mathcal{RPL}}(k) = A_s\left[1 - 2(C+1)\epsilon_1 - C\epsilon_2 - (2\epsilon_1 + \epsilon_2)\ln\left(\frac{k}{k_0}\right)\right]. \tag{10}$$

Here ϵ_1 and ϵ_2 are slow roll parameters (Leach & Liddle 2003). After the release of the first-year *WMAP* data, Martin & Ringeval

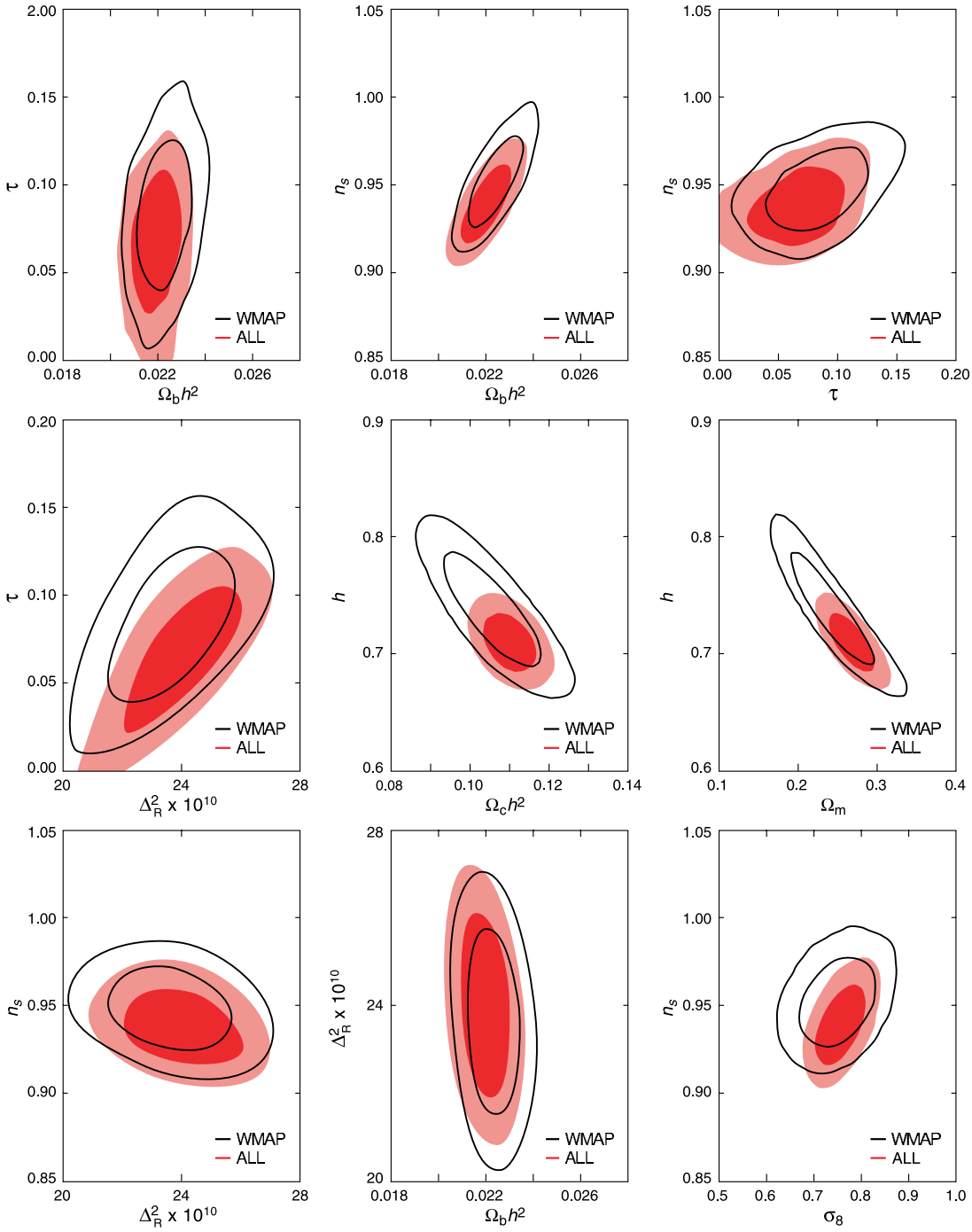

FIG. 10.—Joint two-dimensional marginalized contours (68% and 95% confidence levels) for various combination of parameters for *WMAP* only (*solid lines*) and *WMAP* + 2dFGRS + SDSS + ACBAR + BOOMERANG + CBI + VSA + SN(*HST*/GOODS) + SN(SNLS) (*filled red contours*) for the power-law ΛCDM model.

(2004) considered a primordial power spectrum of a slightly modified form to account for additional trans-Planckian (TP) features,

$$\Delta^2_{\mathcal{RTP}}(k) = \Delta^2_{\mathcal{RPL}}(k)[1 - 2|x|\sigma_0 \cos\theta(k)] - A_s|x|\sigma_0\pi(2\epsilon_1 + \epsilon_2)\sin\theta(k),$$
$$\text{with } \theta(k) = \frac{1}{2\sigma_0}\left[1 + \epsilon_1 + \epsilon_1 \ln\left(\frac{k}{k_0}\right)\right]. \quad (11)$$

Here $\sigma_0 \equiv Hl_c/2\pi$ is determined by the Hubble parameter during inflation, H, and the characteristic length scale for the trans-Planckian manifestation l_c, and $|x|\sigma_0$ characterizes the amplitude of the trans-Planckian corrections to the fiducial spectrum. Martin & Ringeval (2004) report that the χ^2 for such a model could give an improvement of 15 over the power-law inflationary models for an additional 2 degrees of freedom with the first-year *WMAP* data. With 3 years of data, many of the glitches and bites have disappeared, and the best-fit trans-Planckian model of the form in equation (11) reduce the effective χ^2 by only 4 overall and by 5 in TT relative to power-law inflation, a far less significant effect.

The effect of the trans-Planckian corrections can be highly model dependent (See Easther et al. 2005a and 2005b for discussions).

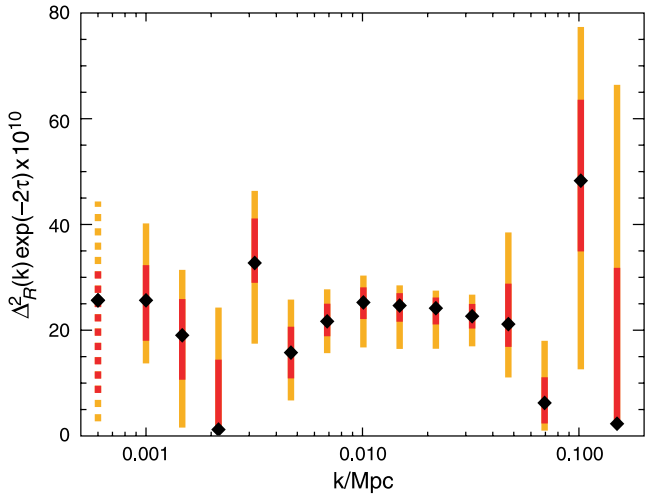

FIG. 11.—Reconstructed primordial curvature fluctuation spectrum, $\Delta^2_R(k)$, for a ΛCDM cosmology, in logarithmically spaced k bins, where k is in Mpc^{-1}. The errors show the 68% (*red*) and 95% (*orange*) constraints and the black diamonds the peak likelihood value. The dashed line shows the values for $k = 0$. Consistent with the predictions of simple inflationary theories, there are no significant features in the spectrum. The data are consistent with a nearly scale-invariant spectrum.

As an alternative, we consider forms that are more general as a way to look for oscillatory signals:

$$\Delta^2_{\mathcal{RTP}}(k) = \Delta^2_{\mathcal{RPL}}(k)[1 + \epsilon_{\rm TP}\cos\theta(k)], \qquad (12)$$

where $\theta = \upsilon(k/k_0) + \phi$ or $\theta = \upsilon\ln(k/k_0) + \phi$. In these models, there are three new parameters: the amplitude, $\epsilon_{\rm TP}$, the frequency, υ, and the phase, ϕ.

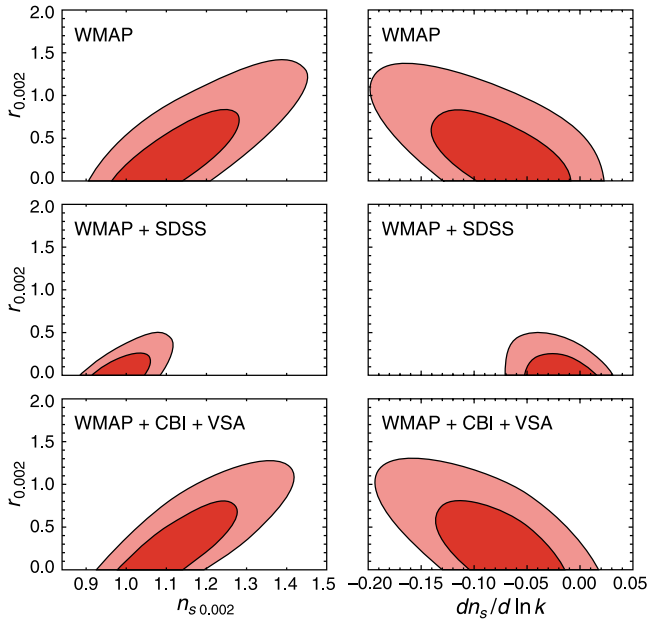

FIG. 12.—Joint two-dimensional marginalized contours (68% and 95%) for inflationary parameters, (r, n_s) (*left*) and (r, $dn_s/d\ln k$) (*right*), for model M11 in Table 3, with parameters defined at $k = 0.002$ Mpc^{-1}. *Top*: *WMAP* only. *Middle*: *WMAP* + SDSS. *Bottom*: *WMAP* + CBI + VSA. Note that $n_s > 1$ is favored because r and n_s are defined at $k = 0.002$ Mpc^{-1}. At $k = 0.05$ Mpc^{-1} $n_s < 1$ is favored. The data do not require a running spectral index, $dn_s/d\ln k$, at more than the 95% confidence level.

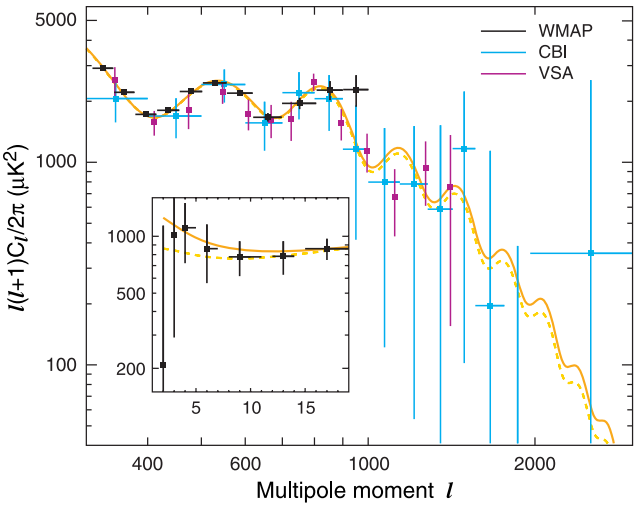

FIG. 13.—Running spectral index model provides a slightly better fit to the data than the power-law spectral index model. The solid line shows the best-fit power-law ΛCDM model, and the dashed line shows the best-fit running spectral index ΛCDM model (fit to *WMAP* + CBI + VSA). The insert compares the models to the *WMAP* $l < 20$ data and shows that the running spectral index model better fits the decline at $l = 2$; however, the improvement in χ^2 is only 3, not enough to strongly argue for the addition of a new parameter. We have also done the same analysis for BOOMERANG and ACBAR data and found similar results: the current high-l data are not yet able to distinguish between the running spectral index and power-law models.

Assuming the ΛCDM model, we fit these three parameters to the data and find reductions of 5 and 9.5 in the overall and TT $\chi^2_{\rm eff}$. As in the Martin & Ringeval model, the improvements in the $\chi^2_{\rm eff}$ are driven by improvements in the fit around $l \sim 30$–100 and the first peak.

6. *WMAP* + INFLATION

The inflationary paradigm (Guth 1981; Sato 1981; Linde 1982; Albrecht & Steinhardt 1982) explains the homogeneity, isotropy, and flatness of the universe by positing an early epoch of accelerated expansion. This accelerated period of expansion also generated superhorizon fluctuations (Guth & Pi 1982; Starobinsky 1982; Mukhanov & Chibisov 1981; Hawking 1982; Bardeen et al. 1983). In the simplest inflationary models, these fluctuations are Gaussian distributed in amplitude with random phase and a nearly scale-invariant spectrum of fluctuations.

The detailed predictions of inflationary models depend on the properties of the inflaton potential (see Linde 2005 and Lyth & Riotto 1999 for recent reviews). Simple inflationary models predict that the slope of the primordial power spectrum, n_s, differs from 1 and also predict the existence of a nearly scale-invariant spectrum of gravitational waves. In this section, we compare the simplest inflationary models to the *WMAP* 3 year data and to other cosmological data sets. Since we are constraining models with tensor modes, we also use the *WMAP* constraints on the amplitude of the B mode signal in the analysis. We characterize these models by seven basic parameters (the six basic parameters of the ΛCDM model plus one additional parameter, r, the ratio of the tensor to scalar power spectrum). Figure 14 shows the likelihood contours for the slope of the scalar fluctuations and the amplitude of the gravitational wave signal.

The *WMAP* 3 year data place significant constraints on inflationary models (see Table 7). The strength of these constraints is apparent when we consider monomial models for the inflaton

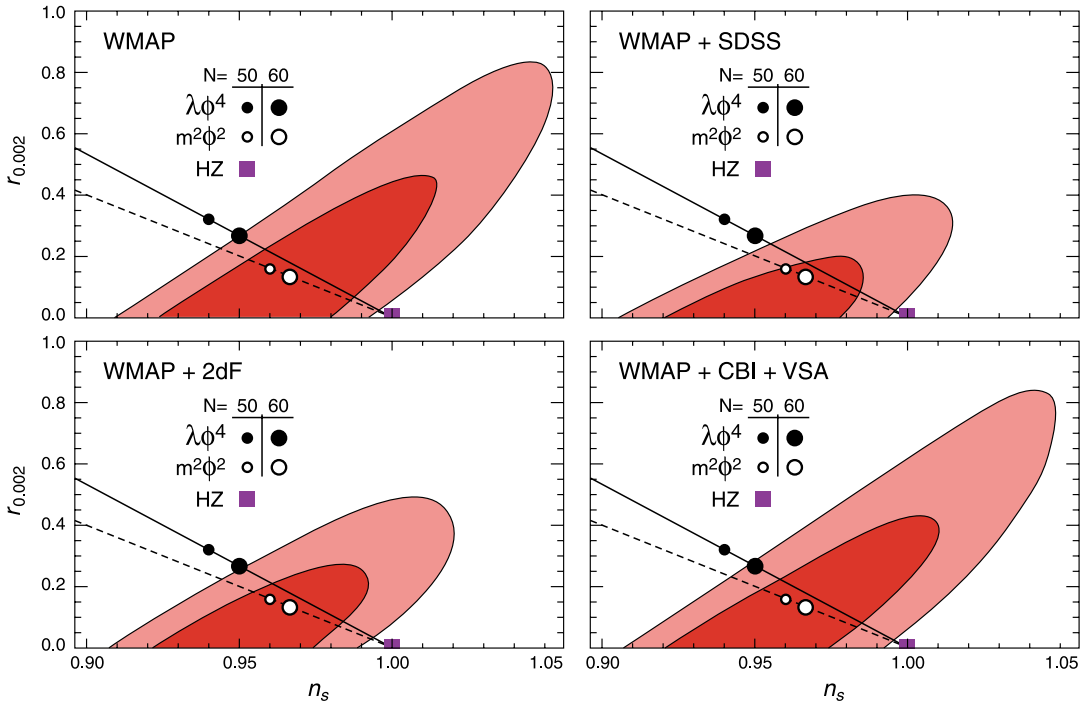

FIG. 14.—Joint two-dimensional marginalized contours (68% and 95% confidence levels) for inflationary parameters ($r_{0.002}, n_s$). We assume a power-law primordial power spectrum, $dn_s/d\ln k = 0$, as these models predict a negligible amount of running index, $dn_s/d\ln k \approx -10^{-3}$. *Upper left*: *WMAP* only. *Upper right*: *WMAP* + SDSS. *Lower left*: *WMAP* + 2dFGRS. *Lower right*: *WMAP* + CBI + VSA. The dashed and solid lines show the range of values predicted for monomial inflaton models with 50 and 60 *e*-folds of inflation (eq. [13]), respectively. The open and filled circles show the predictions of $m^2\phi^2$ and $\lambda\phi^4$ models for 50 and 60 *e*-folds of inflation. The rectangle denotes the scale-invariant Harrison-Zel'dovich-Peebles (HZ) spectrum ($n_s = 1, r = 0$). Note that the current data prefer the $m^2\phi^2$ model over both the HZ spectrum and the $\lambda\phi^4$ model by likelihood ratios greater than 12. ($\delta\chi^2 > 5$).

potential, $V(\phi) \propto \phi^\alpha$. These models (Lyth & Riotto 1999) predict

$$r = 16\epsilon_1 \simeq \frac{4\alpha}{N},$$
$$1 - n_s = 2\epsilon_1 + \epsilon_2 \simeq \frac{\alpha + 2}{2N}, \qquad (13)$$

where N is the number of *e*-folds of inflation between the epoch when the horizon scale modes left the horizon and the end of inflation. Figure 14 compares the predictions of these monomial inflationary models to the data. For $N = 60$, $\lambda\phi^4$ predicts $r = 4/15$, $n_s = 0.95$, just at the outer edge of the 3 σ contour. For $N = 50$, $\lambda\phi^4$ predicts $r = 0.32$, $n_s = 0.94$. However, if we allow for nonminimal gravitational couplings, then the gravity wave predictions of these models are significantly reduced (Hwang & Noh 1998; Komatsu & Futamase 1999) and the models are consistent with the data. Alternatively, the $m^2\phi^2$ model is a good fit to the observations and its predicted level of gravitational waves, $r \simeq 0.13$–0.16, is within range of upcoming experiments.

If we restrict our analysis to a specific model and value of N, then the model specifies both r and n_s. In Table 8 we show the best-fit parameters for the $m^2\phi^2$ potential with $N = 60$. Since n_s and r are set to 0.9667 and 0.1333 for this model, there are only five free parameters ($\Omega_m h^2$, $\Omega_b h^2$, h, τ, and A). The likelihood for the best-fit $m^2\phi^2$ is 12 times higher than the best-fit "Harrison Zel'dovich-Peebles" model with $n_s = 1$ and $r = 0$. To be conservative, this comparison uses the exact (res-4) likelihood code up to $l = 30$ and the slightly lower point source correction discussed in Appendix A. If we cut the exact likelihood off at $l = 12$, and use the original, higher point source value, the likelihood ratio is 15.

In Peiris et al. (2003) we used the inflationary flow equations (Hoffman & Turner 2001; Kinney 2002) to explore the generic predictions of inflationary models. Here we use the slow-roll approximation to explore the implications of the data for inflationary models. The results of the 3 year analysis are consistent with the conclusions from the first-year data: while the data rule out large regions of parameter space, there are also wide range of possible inflationary models consistent with our current data. One

TABLE 7
BEST-FIT INFLATIONARY PARAMETERS (*WMAP* DATA ONLY)

Parameter	ΛCDM + Tensor	ΛCDM + Running + Tensors
$\Omega_b h^2$	0.0233 ± 0.0010	0.0219 ± 0.0012
$\Omega_m h^2$	$0.1195^{+0.0094}_{-0.0093}$	0.128 ± 0.011
h	0.787 ± 0.052	0.731 ± 0.055
n_s	$0.984^{+0.029}_{-0.028}$	1.16 ± 0.10
$dn_s/d\ln k$	Set to 0	-0.085 ± 0.043
r	<0.65 (95% CL)	<1.1 (95% CL)
τ	0.090 ± 0.031	$0.108^{+0.034}_{-0.033}$
σ_8	0.702 ± 0.062	0.712 ± 0.056

TABLE 8
BEST-FIT PARAMETERS FOR $m^2\phi^2$ WITH $N = 60$ (*WMAP* DATA ONLY)

Parameter	Mean	Best Fit
$\Omega_b h^2$	0.02218 ± 0.00045	0.0222
$\Omega_m h^2$	0.1232 ± 0.0076	0.125
h	0.741 ± 0.029	0.734
τ	0.081 ± 0.027	0.0893
σ_8	0.734 ± 0.046	0.749

TABLE 9

CONSTRAINTS ON r, RATIO OF AMPLITUDE OF TENSOR FLUCTUATIONS TO SCALAR FLUCTUATIONS (AT $k = 0.002$ Mpc^{-1})

Data Set	r (No Running)	r (with Running)
WMAP	<0.65 (95% CL)	<1.1 (95% CL)
WMAP + BOOM + ACBAR	<0.68 (95% CL)	<1.1 (95% CL)
WMAP + CBI + VSA	<0.62 (95% CL)	<1.1 (95% CL)
WMAP + 2df	<0.38 (95% CL)	<0.64 (95% CL)
WMAP + SDSS	<0.30 (95% CL)	<0.38 (95% CL)

of the most intriguing features of Figure 14 is that the data now disfavor the exact Harrison-Zel'dovich-Peebles spectrum ($n_s = 1$, $r = 0$). For power-law inflationary models, this suggests a detectable level of gravity waves. There are, however, many inflationary models that predict a much smaller gravity wave amplitude. Alternative models, such as the ekpyrotic scenario (Khoury et al. 2001; Khoury et al. 2002) also predict an undetectable level of gravity waves.

There are several different ways of expressing the constraints that the CMB data impose on inflationary models. These parameters can be directly related to observable quantities: $n_s - 1 = -2\epsilon_1 - \epsilon_2$ and $r = 16\epsilon_1$. For the power-law models, the *WMAP* bound on r implies that $\epsilon_1 < 0.03$ (95% CL). An alternative slow roll representation (see Liddle & Lyth 1992, 1993) uses

$$\epsilon_v \equiv \frac{M_{Pl}^2}{2}\left(\frac{V'}{V}\right)^2, \tag{14}$$

$$\eta_v \equiv M_{Pl}^2\left(\frac{V''}{V}\right). \tag{15}$$

These parameters can be related directly to observables: $r = 16\epsilon_v$ and $n_s - 1 = -6\epsilon_v + 2\eta_v$. Peiris et al. (2003) discusses various classes of models in slow roll parameter space.

Models with a significant gravitational wave contributions, $r \sim 0.3$, make specific predictions for CMB and large-scale structure observations: (1) a modified temperature spectrum with more power at low multipoles and (2) a lower amplitude of density fluctuations (for fixed CMB temperature fluctuations). For power-law models, the strongest CMB constraints come from the shape of the temperature spectrum and the amplitude of density fluctuations. In order to fit the CMB data, models with higher r values require larger values of n_s and land a lower amplitude of scalar fluctuations, which impacts large-scale structure predictions. Thus, the strongest overall constraints on the tensor mode contribution comes from the combination of CMB and large-scale structure measurements (see Table 9). These strong limits rely on our assumption of a power-law spectral index. If we allow for a running index, then models with a large tensor components are consistent with the data.

7. CONSTRAINING THE COMPOSITION OF THE UNIVERSE

7.1. *Dark Energy Properties*

Over the past two decades, there has been growing evidence for the existence of dark energy (Peebles 1984; Turner et al. 1984; Ostriker & Steinhardt 1995; Dunlop et al. 1996; Krauss & Turner 1999; Bahcall et al. 1999). By measuring both the acceleration (Riess et al. 1998; Perlmutter et al. 1999) and deceleration (Riess et al. 2004) of the universe, supernova observations provide the most direct evidence for the existence of dark energy.

The nature of this dark energy is a mystery. From a field theoretic perspective the most natural explanation for this would be the presence of a residual vacuum energy density or cosmological constant, Λ (Carroll et al. 1992; Peebles & Ratra 2003). However, there are well-known fine-tuning and coincidence problems in trying to explain the 120 orders-of-magnitude discrepancy between the expected "natural" Planck-scale energy density of a cosmological constant and the observed dark energy density. These problems motivate a wide range of alternative explanations for the observations including the presence of an extra matter candidate: for example a dynamical, scalar "quintessence" field (Peebles & Ratra 1988; Wetterich 1988; Zlatev et al. 1999), minimally coupled (Caldwell et al. 1998; Ferreira & Joyce 1998) or nonminimally coupled to gravity (Amendola 1999) or other matter (Bean & Magueijo 2001). In this latter case, the measured acceleration is due to interactions in the matter bulk. Another alternative is that modifications to gravity (e.g., Deffayet 2001; Deffayet et al. 2002) are responsible for the observed anomalies.

The dark energy has two distinct cosmological effects: (1) through the Friedman equation, it alters the evolution of $H(z)$, and (2) through the perturbation equations, it alters the evolution of $D(z)$, the growth rate of structure. The supernova data measure only the luminosity distance, which depends on $H(z)$, while the large-scale structure data are sensitive to both $H(z)$ and $D(z)$.

While the presence of dark energy impacts the CMB primarily through the distance to the surface of last scatter, the dark energy clustering properties also affect the CMB properties. The dark energy response to gravitational perturbations depends on its isotropic and anisotropic sound speeds (Hu 1998; Bucher & Spergel 1999). This affects the CMB fluctuations through the ISW effect. If the dark energy can cluster, then it produces a smaller ISW effect and does not enhance the power spectrum at large angular scales. These effects are most dramatic for models with $w < -1$, as dark energy effects in these models turn on suddenly at late times and significantly enhance the quadrupole. This can be understood in terms of the constraints imposed by the shape of the angular power spectrum: if we assume that the dark energy properties can be described by a constant value of w, then fixed peak position and heights (which determine $\Omega_m h^2$) confine our models to a narrow valley in the (Ω_m, w) likelihood surface as shown in Figures 15 and 16. These figures and Table 10 show that the 3 year data enable a more accurate determination of $\Omega_m h^2$ which narrows the width of the degeneracy valley. The pair of figures show that CMB data can place strong limits on models with $w < -1$ and nonclustering dark energy. On the other hand, if the dark energy is a matter component that can cluster, even meagerly, as is the case for scalar field theories where $c_s^2 = 1$, then this clustering counters the suppression of perturbation growth during the accelerative epoch and the quadrupole's magnitude is reduced. This lessens the discriminating power of the quadrupole for measuring w: while CMB data rule out the $w \ll -1$ region in Figure 15, they do not constrain models in the same region in Figure 16.

It is interesting to note that if we relax the assumption of spatial flatness, the data still prefer models with w close to -1 (see Figs. 17 and 18). In this analysis, we assume that the dark energy clusters.

7.2. *Neutrino Properties*

7.2.1. *Neutrino Mass*

Both atmospheric neutrino and solar neutrino experiments show that neutrinos are massive and that there is significant mixing between the various neutrino interaction eigenstates (see

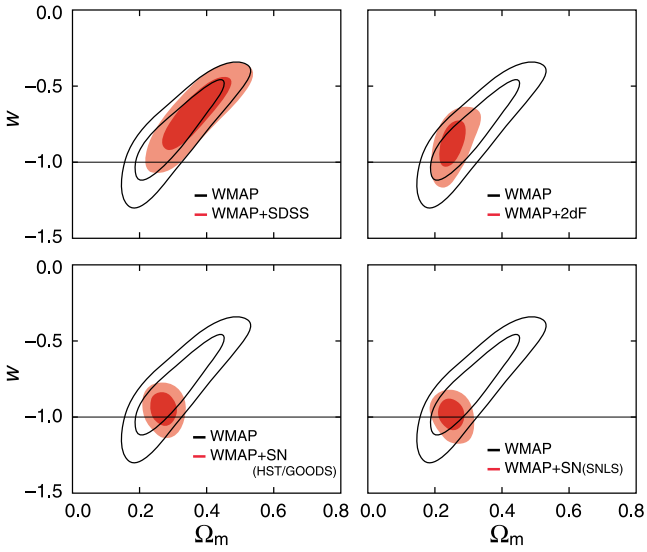

FIG. 15.—Constraints on w, the equation of state of dark energy, in a flat universe model based on the combination of *WMAP* data and other astronomical data. We assume that w is independent of time and ignore density or pressure fluctuations in dark energy. In all of the figures, *WMAP* only constraints are shown in blue and *WMAP* + astronomical data set in red. The contours show the joint 2D marginalized contours (68% and 95% confidence levels) for Ω_m and w. *Upper left*: *WMAP* only and *WMAP* + SDSS. *Upper right*: *WMAP* only and *WMAP* + 2dFGRS. *Lower left*: *WMAP* only and *WMAP* + SN(*HST*/GOODS). *Lower right*: *WMAP* only and *WMAP* + SN(SNLS). In the absence of dark energy fluctuations, the excessive amount of ISW effect at $l < 10$ places significant constraints on models with $w < -1$.

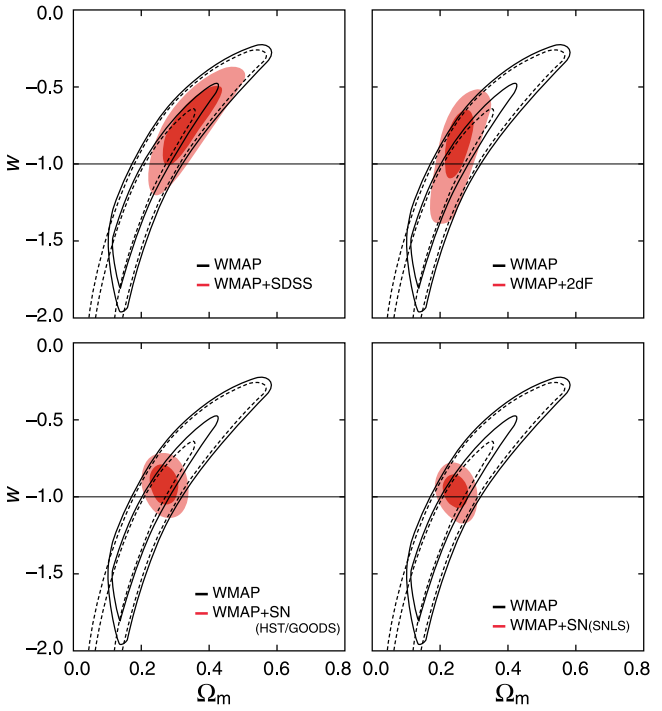

FIG. 16.—Constraints on w, the equation of state of dark energy, in a flat universe, model M6 in Table 3, based on the combination of *WMAP* data and other astronomical data. We assume that w is independent of time, but include density and pressure fluctuations in dark energy with the speed of sound in the comoving frame equal to the speed of light, $c_s^2 = 1$. In all of the figures, *WMAP* data only constraints are shown in black solid lines and *WMAP* + astronomical data set in red. The contours show the joint 2D marginalized contours (68% and 95% confidence levels) for Ω_m and w. *Upper left*: *WMAP* only and *WMAP* + SDSS. *Upper right*: *WMAP* only and *WMAP* + 2dFGRS. *Lower left*: *WMAP* only and *WMAP* + SNgold. *Lower right*: *WMAP* only and *WMAP* + SNLS. In the presence of dark energy fluctuations, the ISW effect at $l < 10$ is nearly canceled by dark energy fluctuations and thus the *WMAP* data alone do not place significant constraints on w. The *WMAP* only models are shown assuming no prior on H_0 (*dashed black lines*) and with an assumed prior of $H_0 < 100$ km s^{-1} Mpc^{-1} (*solid black lines*).

Mohapatra et al. 2005 for a recent review). These experiments measure the difference between the square of the neutrino masses, $m_{\nu_i}^2 - m_{\nu_j}^2$, rather than the mass of individual neutrino mass eigenstates. Cosmological measurements nicely complement these measurements by constraining $\sum_i m_{\nu_i}$. Since light massive neutrinos do not cluster as effectively as cold dark matter, the neutrino mass has a direct impact on the amplitude and shape of the matter power spectrum (Bond et al. 1980; Bond & Szalay 1983; Ma 1996; Hu et al. 1998). The presence of a significant neutrino component lowers the amplitude of matter fluctuations on small scales, σ by roughly a factor proportional to ($\sum m_\nu$), where $\sum m_\nu$ is the total mass summed over neutrino species, rather than the mass of individual neutrino species. The current large-scale structure data restrict $\Delta \ln \sigma_8 < 0.2$, but they are not sensitive enough to resolve the free-streaming scale of individual neutrino species (Takada et al. 2006).

Using a combination of the first-year *WMAP* data, small-scale CMB, and large-scale structure data, Spergel et al. (2003) placed an upper limit on $\sum_i m_{\nu_i} < 0.7$ eV. While this limit does not depend on the Lyα data, it is sensitive to galaxy bias measurements (which normalizes the large-scale structure data) and to the addition of small-scale CMB data (which improves the measurement of cosmological parameters). Over the past year, several groups obtained comparable (but slightly different) limits (Hannestad 2003; Pierpaoli 2003; Elgarøy & Lahav 2003). The differences are due to including (or removing) external data sets and priors or to adding additional cosmological parameters.

The limits on neutrino masses from *WMAP* data alone are now very close to limits based on combined CMB data sets. Ichikawa et al. (2005) used the CMB data alone to place a limit on the neutrino mass of $\sum m_\nu < 2.0$ eV. Using *WMAP* data alone, we now find $\sum m_\nu < 1.8$ eV.

Since the presence of massive neutrinos slows the growth of small-scale structure, the combination of CMB and large-scale structure data constrain the neutrino mass. Figure 19 shows the likelihood function as a function of neutrino mass and amplitude of mass fluctuations in the local universe, σ_8. The 95% confidence limits on neutrino mass are given in Table 11. The combination of *WMAP* with SDSS and *WMAP* with 2dFGRS data constrain σ_8 at roughly the same level, 20% at the 95% confidence level. This constraint yields comparable limits on the neutrino mass. While the *WMAP* data have improved, the error bars on σ_8 have not significantly changed from the limits obtained from WMAPext + 2dFGRS, thus, the limit on neutrino mass is quite close to the first-year limit. Note that in the first-year analysis, we used the Verde et al. (2002) measurement of bias for the 2dFGRS preliminary data as there had not been an equivalent analysis done for the full

TABLE 10

CONSTRAINTS ON w IN FLAT COSMOLOGIES WITH DIFFERENT ASSUMPTION ABOUT DARK ENERGY CLUSTERING

Data Set	With Perturbations	No Perturbations
WMAP + SDSS	$-0.75^{+0.17}_{-0.16}$	-0.69 ± 0.16
WMAP + 2dFGRS	$-0.89^{+0.16}_{-0.14}$	$-0.877^{+0.097}_{-0.098}$
WMAP + SNGold	$-0.919^{+0.081}_{-0.080}$	$-0.942^{+0.075}_{-0.073}$
WMAP + SNLS	$-0.967^{+0.073}_{-0.072}$	$-0.984^{+0.070}_{-0.068}$
CMB + LSS + SN	$-0.926^{+0.054}_{-0.053}$	-0.915 ± 0.051

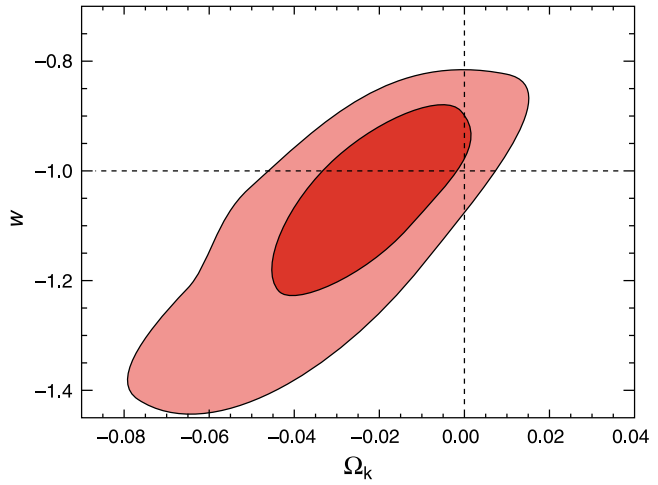

FIG. 17.—Constraints on a nonflat universe with quintessence-like dark energy with constant w (model M10 in Table 3). The contours show the 2D marginalized contours for w and Ω_k based on the CMB + 2dFGRS + SDSS + supernova data sets. This figure shows that with the full combination of data sets, there are already strong limits on w without the need to assume a flat universe prior. The marginalized best-fit values for the equation of state and curvature are $w = -1.08 \pm 0.12$ and $\Omega_k = -0.026^{+0.016}_{-0.015}$ at the 68% confidence level.

2dFGRS data set. As discussed in § 4.1.4, we now marginalize over the 2dFGRS bias and use the bias measurements of Seljak et al. (2005b) for SDSS.

If the constraints on amplitude are reliable, then small-scale matter power spectrum structure data can significantly improve these neutrino constraints. Goobar et al. (2006) have recently completed a CMB + Lyα study and place a limit of $\sum m_\nu < 0.30$ eV (95% CL). Similarly, cluster-based measurements of σ_8 and lensing-based measurements of σ_8 have the potential to tighten the constraint on m_ν.

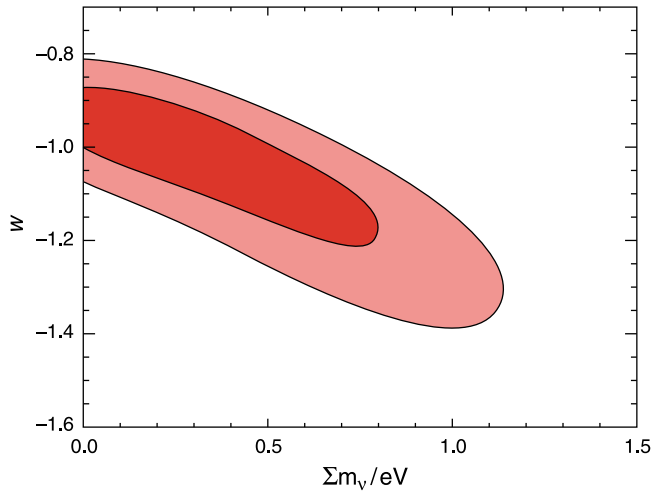

FIG. 18.—Constraints on a flat universe with quintessence-like dark energy and nonrelativistic neutrinos. The contours show the 2D marginalized constraints on the mass of nonrelativistic neutrinos, m_ν, and the dark energy equation of state, w, assumed constant, based on the CMB + 2dFGRS + SDSS + supernova data sets. In this analysis, we assume that the dark energy clusters. With the combination of CMB + 2dFGRS + SDSS + supernova data sets, there is not a strong degeneracy between neutrino and dark energy properties. Even in this more general model, we still have an interesting constraint on the neutrino mass and equation of state: $\sum m_\nu < 1.0$ eV (95%CL) and $w = -1.07 \pm 0.12$ (68% CL). This suggests that the astronomical dark energy and neutrino limits are robust even when we start to consider more baroque models.

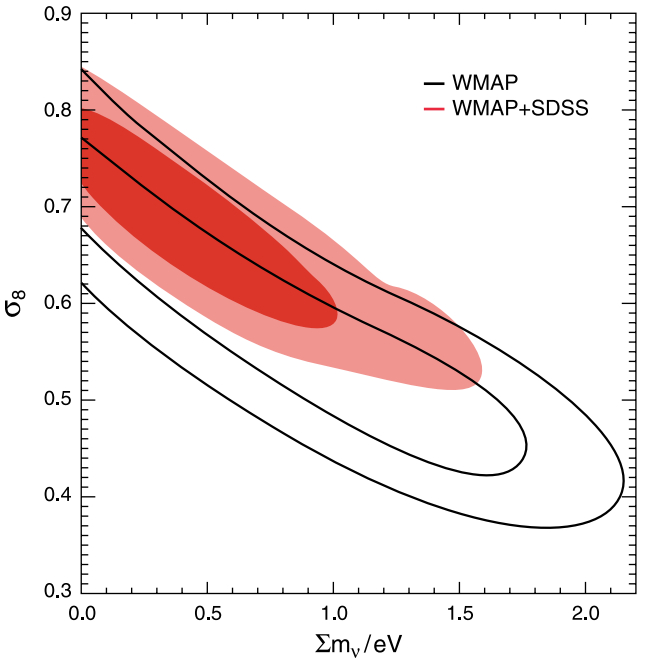

FIG. 19.—Joint two-dimensional marginalized contours (68% and 95% confidence levels) on (σ_8, m_ν) for *WMAP* only, model M7 in Table 3, and *WMAP* + SDSS. By measuring the growth rate of structure from $z = 1088$ to $z \simeq 0$, these observations constrain the contribution of nonrelativistic neutrinos to the energy density of the universe.

7.2.2. *Number of Relativistic Species*

If there are other light stable neutral particles (besides the three light neutrinos and the photon), then these particles will affect the CMB angular power spectrum and the evolution of large-scale structure. Because of the details of freeze-out at electron-positron annihilation (Gnedin & Gnedin 1998; Dolgov et al. 1999), QED corrections at finite temperature (Mangano et al. 2002), and nontrivial terms in the neutrino mass matrix (Mangano et al. 2005), the effective number of neutrino species is slightly greater than 3. Any light particle that does not couple to electrons, ions, and photons will act as an additional relativistic species. For neutrinos, we can compute their effects accurately as their temperature is $(4/11)^{1/3}$ of the CMB temperature. For other relativistic species, the limit on $N_\nu^{\rm eff} - 3.04$ can be converted into a limit on their abundance by scaling by the temperature.

The shape of the CMB angular power spectrum is sensitive to the epoch of matter/radiation equality. If we increase N_ν, the effective number of neutrino species, then we will need to also increase the cold dark matter density, $\Omega_c h^2$, and slowly change other parameters to remain consistent with the *WMAP* data (Bowen et al. 2002). In addition, the presence of these additional neutrino species alters the damping tail and leaves a distinctive signature on the high-l angular power spectrum (Bashinsky & Seljak 2004) and on the small-scale matter power spectrum.

TABLE 11
CONSTRAINTS ON NEUTRINO PROPERTIES

Data Set	$\sum m_\nu$ (95% Limit for $N_\nu = 3.04$)	N_ν
WMAP	1.8 eV (95% CL)	...
WMAP + SDSS	1.3 eV (95% CL)	$7.1^{+4.1}_{-3.5}$
WMAP + 2dFGRS	0.88 eV (95% CL)	2.7 ± 1.4
CMB + LSS + SN	0.66 eV (95% CL)	3.3 ± 1.7

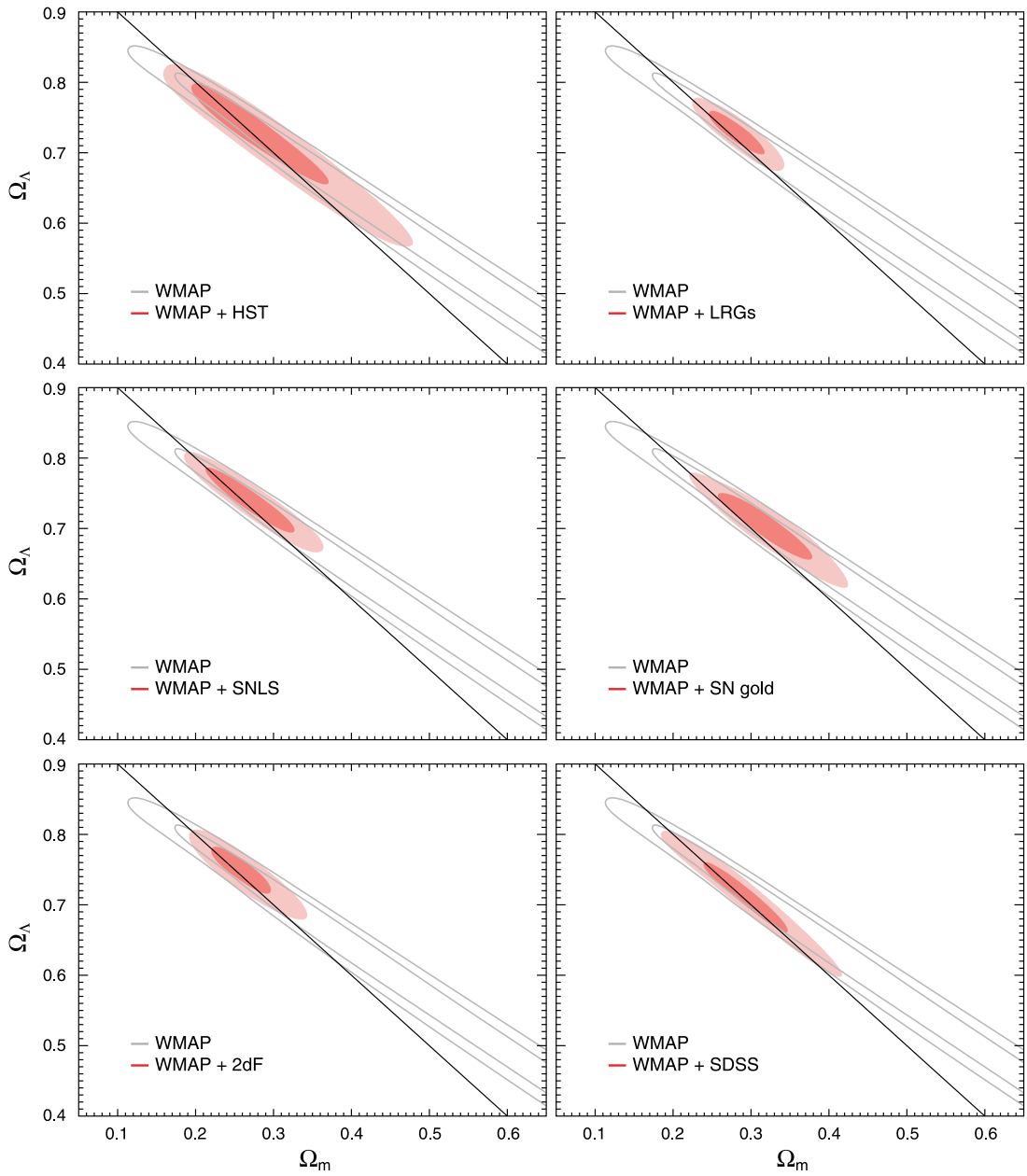

FIG. 20.—Joint two-dimensional marginalized contours (68% and 95%) for matter density, Ω_m, and vacuum energy density, Ω_Λ, for power-law CDM models with dark energy and dark matter, but without the constraint that $\Omega_m + \Omega_\Lambda = 1$ (model M10 in Table 3). The panels show various combinations of *WMAP* and other data sets. While models with $\Omega_m = 0.415$ and $\Omega_\Lambda = 0.630$ are a better fit to the *WMAP* 3 year data alone than the flat model, the combination of *WMAP* 3 year data and other astronomical data favors nearly flat cosmologies. *Upper left*: *WMAP* + *HST* Key Project measurement of H_0. *Upper right*: *WMAP* + SDSS LRG measurement of the angular diameter distance to $z = 0.35$. *Middle left*: *WMAP* + SNLS data. *Middle right*: *WMAP* + SNGold. *Lower left*: *WMAP* + 2dFGRS. *Lower right*: *WMAP* + SDSS.

The high matter density also alters the growth rate of structure, thus, the combination of large-scale structure and CMB data constrains the existence of any new light relativistic species. These limits constrain both the existence of new particles and the interaction properties of the neutrino (Bowen et al. 2002; Hall & Oliver 2004). Hannestad (2001) used the pre-*WMAP* CMB, and large-scale structure data to place an upper limit of $N_\nu < 17$. After the release of the first-year *WMAP* data, several authors (Hannestad 2003; Pierpaoli 2003; Barger et al. 2003; Crotty et al. 2003; Elgarøy & Lahav 2003; Barger et al. 2004; Hannestad 2006) used the combination of *WMAP*, 2dFGRS, and various external data to reduce this limit by a factor of 2–3. Table 11 shows the maximum-likelihood estimate of the number of neutrino species for different data set combinations using the new *WMAP* data. The SDSS and 2dFGRS data differ in the shapes of the two measured power spectra: this difference leads to the disagreement in their best-fit values for $N_\nu^{\rm eff}$.

7.3. *Nonflat Universe*

The *WMAP* observations place significant constraints on the geometry of the universe through the positions of the acoustic peaks. The sound horizon size, r_s, serves as a very useful ruler for measuring the distance to the surface of last scatter. For power-law open universe models, $\theta_A = 0.595^\circ \pm 0.002^\circ$. Figure 20 shows that this constraint confines the likelihood function to a narrow degeneracy surface in (Ω_m, Ω_Λ). This degeneracy line is well fitted by $\Omega_K = -0.3040 + 0.4067\Omega_\Lambda$. However, the CMB data alone do not distinguish between models along the valley: it is

TABLE 12
JOINT DATA SET CONSTRAINTS ON GEOMETRY AND VACUUM ENERGY

Data Set	Ω_K	Ω_Λ
WMAP + $h = 0.72 \pm 0.08$	-0.014 ± 0.017	0.716 ± 0.055
WMAP + SDSS.....	$-0.0053^{+0.0068}_{-0.0060}$	0.707 ± 0.041
WMAP + 2dFGRS	$-0.0093^{+0.0098}_{-0.0092}$	$0.745^{+0.025}_{-0.024}$
WMAP + SDSS LRG	-0.012 ± 0.010	0.728 ± 0.021
WMAP + SNLS	-0.011 ± 0.012	0.738 ± 0.030
WMAP + SNGold.....	-0.023 ± 0.014	0.700 ± 0.031

consistent with both flat models and models with $\Omega_\Lambda = 0$. If we allow for a large SZ signal, then the *WMAP* data alone favor a model with $\Omega_K = -0.04$; however, this model is not consistent with other astronomical data.

The combination of *WMAP* data and other astronomical data places strong constraints on the geometry of the universe (see Table 12):

1. The angular scale of the baryon acoustic oscillation (BAO) peak in the SDSS LRG sample (Eisenstein et al. 2005) measures the distance to $z = 0.35$. The combination of the BAO and CMB observations strongly constrain the geometry of the universe. The position of the peak in the galaxy spectrum in the SDSS and 2dFGRS surveys provide local measurements of the angular diameter distance.
2. Figure 21 shows that the Hubble constant varies along this line, so that the *HST* Key Project constraint on the Hubble constant leads to a strong bound on the curvature.
3. SNe observations measure the luminosity distance to $z \sim 1$. The combination of SNe data and CMB data also favors a nearly flat universe.

The strong limits quoted in Table 12 rely on our assumption that the dark energy has the equation of state, $w = -1$. In § 7.1, we discussed relaxing this assumption and assuming that w is a constant. Figure 15 shows that by using the combination of CMB, large-scale structure, and supernova data, we can simultaneously constrain both Ω_k and w. This figure confirms that our minimal model, $\Omega_k = 0$, and $w = -1$ is consistent with the current data.

8. ARE CMB FLUCTUATIONS GAUSSIAN?

The detection of primordial non-Gaussian fluctuations in the CMB would have a profound impact on our understanding of the physics of the early universe. While the simplest inflationary models predict only mild non-Gaussianities that should be undetectable in the *WMAP* data, there are a wide range of plausible mechanisms for generating significant and detectable non-Gaussian fluctuations (see Bartolo et al. 2004a for a recent review). There are a number of plausible extensions of the standard inflationary model (Lyth et al. 2003; Dvali et al. 2004; Bartolo et al. 2004b) or alternative early universe models (Arkani-Hamed et al. 2004; Alishahiha et al. 2004) that predict skewed primordial fluctuations at a level detectable by *WMAP*.

There are other cosmological mechanisms for generating non-Gaussianity. The smallness of the CMB quadrupole seen by both *WMAP* and *COBE* has stimulated interest in the possibility that the universe may be finite (Luminet et al. 2003; Aurich et al. 2005). If the universe were finite and had a size comparable to horizon size today, then the CMB fluctuations would be non-Gaussian (Cornish et al. 1996; Levin et al. 1997; Bond et al. 2000; Inoue et al. 2000). While analysis of the first-year data did not find any evidence for a finite universe (Phillips & Kogut 2006; Cornish et al. 2004), these searches were nonexhaustive so the data rule out most but not all small universes.

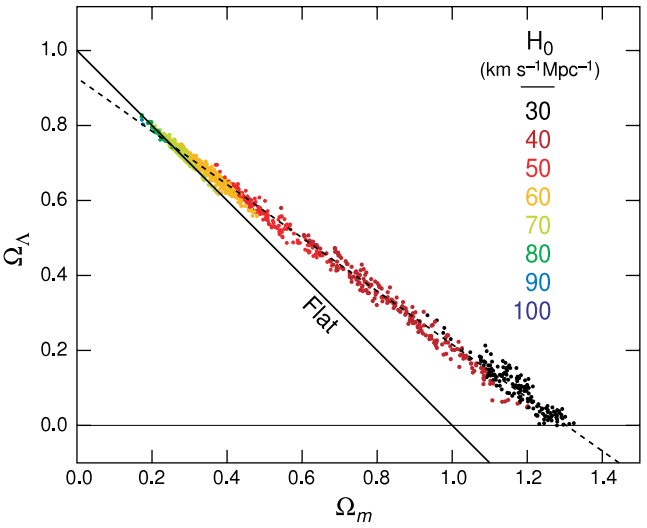

FIG. 21.—Range of nonflat cosmological models consistent with the *WMAP* data only. The models in the figure are all power-law CDM models with dark energy and dark matter, but without the constraint that $\Omega_m + \Omega_\Lambda = 1$ (model M10 in Table 3). The different colors correspond to values of the Hubble constant as indicated in the figure. While models with $\Omega_\Lambda = 0$ are not disfavored by the *WMAP* data only ($\Delta\chi^2_{\rm eff} = 0$; model M4 in Table 3), the combination of *WMAP* data plus measurements of the Hubble constant strongly constrain the geometry and composition of the universe within the framework of these models. The dashed line shows an approximation to the degeneracy track: $\Omega_K = -0.3040 + 0.4067\Omega_\Lambda$. Note that for these open universe models, we assume a flat prior on Ω_Λ.

Using an analysis of Minkowski functionals, Komatsu et al. (2003) did not find evidence for statistically isotropic but non-Gaussian fluctuations in the first-year sky maps. The Colley & Gott (2003) reanalysis of the maps confirmed the conclusion that there was no evidence of non-Gaussianity. Eriksen et al. (2004b) measured the Minkowski functionals and the length of the skeleton for the first-year maps on 11 different smoothing scales. While they found no evidence for deviations from non-Gaussianity using the Minkowski area, Minkowski length, and the length of the skeleton, they did find an intriguingly high χ^2 for the genus statistic.

For a broad class of theories, we can parameterize the effects of nonlinear physics by a simple coupling term that couples a Gaussian random field, ψ, to the Bardeen curvature potential, Φ:

$$\Phi(\boldsymbol{x}) = \psi(\boldsymbol{x}) + f_{\rm NL}\psi^2(\boldsymbol{x}). \quad (16)$$

Simple inflationary models based on a single slowly rolling scalar field with the canonical kinetic Lagrangian predict $|f_{\rm NL}| < 1$ (Maldacena 2003; Bartolo et al. 2004a); however, curvaton inflation (Lyth et al. 2003), ghost inflation (Arkani-Hamed et al. 2004), and Dirac-Born-Infeld (DBI) inflation models (Alishahiha et al. 2004) can generate much larger non-Gaussianity, $|f_{\rm NL}| \sim 100$. Using the *WMAP* first-year data, Komatsu et al. (2003) constrained $-54 < f_{\rm NL} < 134$ at the 95% confidence level. Several different groups (Gaztañaga & Wagg 2003; Mukherjee & Wang 2003; Cabella et al. 2004; Phillips & Kogut 2006; Creminelli et al. 2006) have applied alternative techniques to measure $f_{\rm NL}$ from the maps and have similar limits on $f_{\rm NL}$. Babich et al. (2004) note that these limits are sensitive to the physics that generated the non-Gaussianity as different mechanisms predict different forms for the bispectrum.

Since the release of the *WMAP* data, several groups have claimed detections of significant non-Gaussianities (Tegmark et al. 2003;

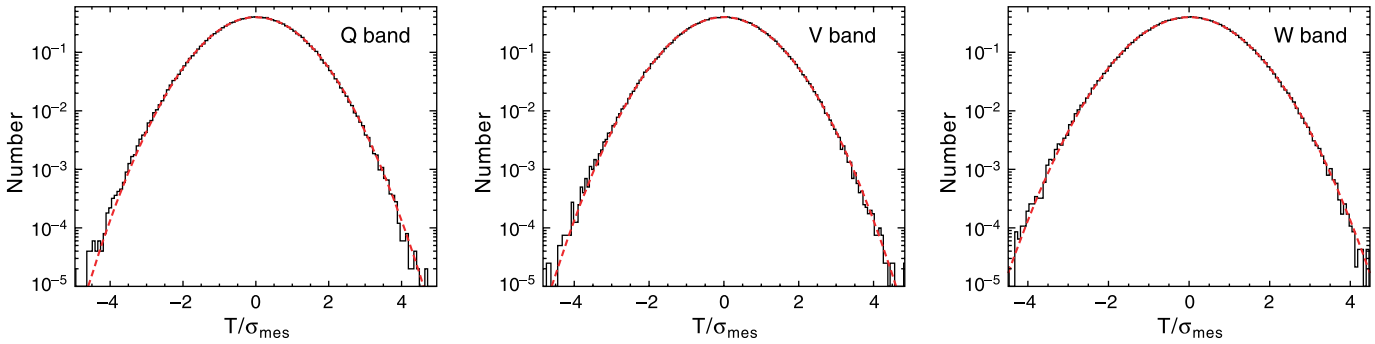

FIG. 22.—Normalized one-point distribution function of temperature anisotropy, defined in eq. (17), for the template-cleaned Q (*left*), V (*middle*), and W (*right*) band maps outside the Kp2 cut. The sky maps have been degraded to $N_{\rm side} = 256$ for this figure. The red line shows the Gaussian distribution, which is an excellent fit to the one-point distribution function.

Eriksen et al. 2004a; Copi et al. 2004; Vielva et al. 2004; Hansen et al. 2004; Park 2004; Larson & Wandelt 2004; Cruz et al. 2005). Almost all of these claims imply that the CMB fluctuations are not stationary and claim a preferred direction or orientation in the data. Hajian et al. (2005) argue that these detections are based on a posteriori selection of preferred directions and do not find evidence for preferred axes or directions. Because of the potential revolutionary significance of these detections, they must be treated with some caution. Galactic foregrounds are non-Gaussian and anisotropic, and even low-level contamination in the maps can produce detectable non-Gaussianities (Chiang et al. 2003; Naselsky et al. 2005) but have only minimal effects on the angular power spectrum (Hinshaw et al. 2003). Similarly, point sources can be a source of non-Gaussianity at small angular scales (Eriksen et al. 2004a). Because of the *WMAP* scan pattern, the variance in the noise in the maps is spatially variable. There is significant $1/f$ noise in several of the Difference Assemblies (DAs) (particularly W4)—which leads to anisotropies in the two-point function of the noise. Finally, most of the claimed detections of significant non-Gaussianities are based on a posteriori statistics. Many of the claimed detections of non-Gaussianity can be tested with the 3 year *WMAP* data (see footnote 16). Future tests should use the simulated noise maps, Monte Carlo simulations, and the difference maps (year 1 − year 2, year 2 − year 3, etc.) to confirm that the tests are not sensitive to noise statistics and the multifrequency data to confirm that any claimed non-Gaussianity has a thermal spectrum. Claims of non-Gaussianity incorporating data close to the Galactic plane (within the Kp2 cut) should be treated with caution, as the foreground corrections near the plane are large and uncertain.

The following subsections describe a number of statistical tests designed to search for non-Gaussianities in the microwave sky. All of these analyses use 3 year maps cleaned with the KKaHa-Dust templates (Hinshaw et al. 2007). We refer to these maps as the "template-cleaned maps." In the first subsection, we show that the probability distribution function of the cleaned CMB maps is consistent with Gaussianity. In the second subsection, we show that the Minkowski functionals are consistent with expectations for Gaussian fluctuations. Next, we compute the bispectrum of the cleaned maps. The final subsection describes measurements of the four-point function.

8.1. *One-Point Distribution Function*

One of the simplest tests of non-Gaussianity is a measurement of the one-point probability function. However, because the detector noise in the map is inhomogeneous (higher in the ecliptic plane and lower near the poles), this test is nontrivial. We account for the spatial variations in noise by computing a variance-normalized temperature for each pixel in a given map:

$$u_i = \frac{T_i}{\sqrt{\sigma^2_{\rm noise}/N_{\rm obs} + \sigma^2_{\rm CMB}}}, \qquad (17)$$

where T_i is the measured temperature signal, the detector noise depends on the number of observations of a given pixel, $N_{\rm obs}$. Here we apply the analysis to template-cleaned maps outside the Kp2 sky cut. For this analysis, we compute $\sigma_{\rm noise}$, the noise per observation, from the year 1 − year 2 difference maps and fit $\sigma_{\rm CMB}$, the CMB signal, to the sum of the year one and year two maps. With $N_{\rm side} = 1024$, the computed $\sigma_{\rm noise}$ value is within 0.5% of the value of σ_0 estimated from the time series (Jarosik et al. 2007). As we lower the resolution, the value of $\sigma_{\rm noise}$ slowly increases with increasing pixel size. For W4, the channel with the large $1/f$ noise, this change is most dramatic; the value of σ_0 at resolution $N_{\rm side} = 32$ is 6% higher than the value computed for $N_{\rm side} = 1024$.

Figures 22 and 23 show the one-point distribution function of the cleaned sky maps as a function of resolution. Most of the distributions appear to be rather well fitted by a Gaussian. This result is consistent with that from the area of hot and cold spots (one of the Minkowski functionals), which measures the cumulative one-point probability function. However, with $N_{\rm side} = 16$, there is a slight excess at negative T in the first panel of Figure 23. This is due to the cold spot near $l = 209$ and $b = -57$ discussed by Vielva et al. (2004) in the context of the first-year data. Cruz et al. (2006) argue that there is a 1.85% probability of seeing the level of skewness and kurtosis associated with this cold spot. While this probability would increase if they allowed for variable smoothing scales, the results are intriguing and merit further investigation.

8.2. *Size and Shape of Hot and Cold Spots*

Minkowski functionals (Minkowski 1903; Gott et al. 1990; Mecke et al. 1994; Schmalzing & Buchert 1997; Schmalzing & Gorski 1998; Winitzki & Kosowsky 1998) measure the contour length, area, and number of hot and cold spots. Following the approach used in the first-year analysis, we compute the Minkowski functionals as a function of temperature threshold, $\nu = \Delta T/\sigma$, where σ is the standard deviation of the map. For a two-dimensional map, we measure three Minkowski functionals, the genus, $G(\nu)$, of the maps, the contour length, $C(\nu)$ and the area within the contours, $A(\nu)$.

We compare the measured values of the Minkowski functionals to their expected amplitude for a Gaussian sky. We simulate a

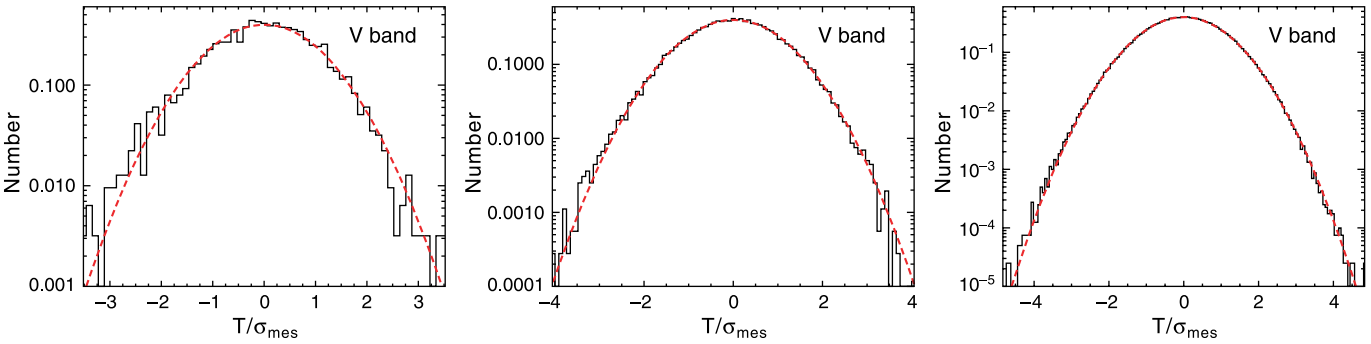

FIG. 23.—Normalized one-point distribution function of temperature anisotropy, defined in eq. (17), for the template-corrected V-band data maps outside the Kp0 cut. The sky maps have been degraded to $N_{\rm side} = 16$ (*left*), 64 (*middle*), and 256 (*right*) for this figure. The red line shows the best-fit Gaussian, which is an excellent fit to the one-point distribution function.

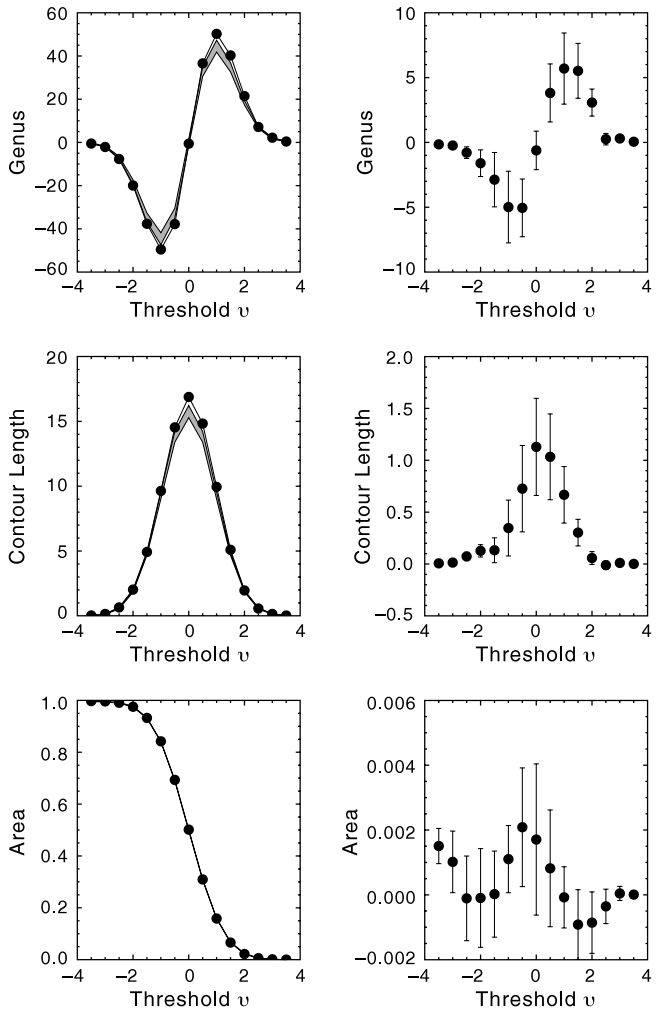

FIG. 24.—*WMAP* data are in excellent agreement with the Gaussian simulations based on the analysis of the Minkowski functionals for the 3 year *WMAP* data outside the Kp0 cut. The filled circles in the left panel shows the values for the data at $N_{\rm side} = 128$ (28′ pixels). The gray band shows the 68% confidence interval for the Gaussian Monte Carlo simulations. The right panels show the residuals between the mean of the Gaussian simulations and the *WMAP* data. Note that the residuals are highly correlated from bin to bin, so the χ^2 are consistent with the Gaussian simulations.

series of maps based on the best-fit parameters for ΛCDM and the *WMAP* noise patterns. For the analysis, we use the template-cleaned V + W maps outside the Kp0 sky mask region. Following the approach used in Komatsu et al. (2003) we compute the Minkowski functionals at 15 thresholds from $-3.5\ \sigma$ to $+3.5\ \sigma$ and compare each functional to the simulations using a goodness of fit statistic,

$$\chi^2 = \sum_{\nu_1\nu_2} \left[F^i_{WMAP} - \langle F^i_{\rm sim}\rangle\right]_{\nu_1} \Sigma^{-1}_{\nu_1\nu_2} \left[F^i_{WMAP} - \langle F^i_{\rm sim}\rangle\right]_{\nu_2}, \quad (18)$$

where F^i_{WMAP} is the Minkowski functional computed from the *WMAP* data, $F^i_{\rm sim}$ is the Minkowski functional computed from the simulated data, and $\Sigma_{\nu_1\nu_2}$ is the bin-to-bin covariance from the simulations. Figure 24 shows the Minkowski functionals as a function of threshold for a map with $N_{\rm side} = 128$ (28′ pixels). These pixels are small enough to resolve the acoustic spots, but not so small as to be noise dominated. The figure shows that the contour length, area, and number of spots is consistent with expectations for a Gaussian theory. Table 13 lists the probability of measuring the observed values of the Minkowski functionals

TABLE 13

χ^2 FOR MINKOWSKI FUNCTIONALS FOR 15 THRESHOLDS FOR THE TEMPLATE-CLEANED VW

Pixels	Minkowski	χ^2	dof	⟨Sim⟩	$F > WMAP$
128.....	Genus	20.9	15	15.4	0.17
	Contour	19.2	15	15.1	0.19
	Spot area	14.0	15	15.3	0.54
	Combined	51.6	45	47.2	0.31
64.....	Genus	18.3	15	14.9	0.24
	Contour	19.3	15	14.9	0.19
	Spot area	8.4	15	15.5	0.93
	Combined	50.0	45	47.2	0.36
32.....	Genus	17.3	15	15.4	0.31
	Contour	27.8	15	15.8	0.04
	Spot area	8.5	15	15.8	0.89
	Combined	43.8	45	49.1	0.61
16.....	Genus	28.2	15	15.8	0.05
	Contour	19.0	15	15.7	0.29
	Spot area	14.1	15	15.6	0.47
	Combined	84.6	45	49.4	0.03
8.....	Genus	10.8	15	15.5	0.62
	Contour	24.3	15	16.0	0.09
	Spot area	28.8	15	15.0	0.05
	Combined	100.5	45	49.0	0.03

TABLE 14
AMPLITUDE OF NON-GAUSSIANITY

Band	$f_{\rm NL}$	$b_{\rm src}$ (10^{-5} μK^3 sr^2)
Q	41 ± 55	4.8 ± 2.0
V	25 ± 50	0.12 ± 0.52
W	11 ± 50	−0.21 ± 0.34
V + W	18 ± 46	0.25 ± 0.26
Q + V + W	30 ± 42	0.73 ± 0.36

as a function of pixel size. At all resolutions, the maps are consistent with Gaussian simulations.

We have also simulated non-Gaussian sky with non-Gaussian signals generated according to equation (16). By comparing these simulations to the data, we can constrain $f_{\rm NL} = 7 \pm 66$ at the 68% confidence level, consistent with the bispectrum measurement (§ 8.3).

8.3. *Bispectrum*

The bispectrum is sensitive to both primordial non-Gaussianity and various sources of secondary anisotropy (Spergel & Goldberg 1999; Goldberg & Spergel 1999; Komatsu & Spergel 2001). Here we use the *WMAP* 3 year data to constrain the amplitude of primordial non-Gaussianity and to detect the amplitude of the point source signal in the cleaned Q-, V-, and W-band maps.

The amplitude of the primordial non-Gaussian signal can be found by computing a cubic statistic on the map (Komatsu et al. 2005):

$$S_{\rm primordial} = \frac{1}{f_{\rm sky}} \int 4\pi r^2\, dr \int \frac{d^2\hat{n}}{4\pi} A(r, \hat{n}) B^2(r, \hat{n}), \qquad (19)$$

where $f_{\rm sky}$ is the fraction of the sky used in the analysis, $B(r, \hat{n})$ is a Weiner filtered map of the primordial fluctuations, and A is optimized to detect the form of the nonlinearities. The amplitude of $S_{\rm primordial}$ can be related directly to $f_{\rm NL}$. Here we use A and B as defined in Komatsu et al. (2005). While we used $l_{\rm max} = 265$ for the first-year analysis, we use $l_{\rm max} = 350$ for the present analysis, as noise is significantly lower with 3 years of data. The error on $f_{\rm NL}$ begins to increase at $l_{\rm max} = 350$ due to the presence of inhomogeneous noise. Note that Creminelli et al. (2006) argue that the optimal estimator for $S_{\rm primordial}$ should include a term that is linear in temperature anisotropy as well as a cubic term that we already have in equation (19). They claim that their estimator could reduce the error on $f_{\rm NL}$ by about 20%. While their result is attractive, we shall not include the linear term in our analysis, as their estimator has not been tested against non-Gaussian simulations and thus it is not yet clear if it is unbiased.

Point sources are an expected cause of non-Gaussianity. Because point sources are not very correlated on the angular scales probed by *WMAP*, the point sources make a constant contribution to the bispectrum, $b_{\rm src}$. Komatsu et al. (2005) develops a cubic statistic approach for computing $b_{\rm src}$:

$$S_{\rm ps} = \frac{1}{m_3} \int \frac{d^2\hat{n}}{4\pi} D^3(\hat{n}), \qquad (20)$$

where $m_3 = (4\pi)^{-1} \int d^2\hat{n} M^3(\hat{n})$, $M(\hat{n}) = [\sigma^2_{\rm CMB} + N(\hat{n})]^{-1}$, and $D(\hat{n})$ is a match filter optimized for point source detection:

$$D(\hat{n}) = \sum_{l,m} \frac{b_l}{\tilde{C}_l} a_{lm} Y_{lm}(\hat{n}), \qquad (21)$$

where b_l is a beam transfer function and $\tilde{C}_l = C_l^{\rm cmb} b_l^2 + N_l$. We weight the temperature maps by $M(\hat{n})$ before we calculate a_{lm}. We use $l_{\rm max} = 1024$ for calculating $D(\hat{n})$. (See § 3.2 of Komatsu et al. 2003 for details of the weighting method.) Given the uncertainties in the source cutoff and the luminosity function, the values for $b_{\rm src}$ in Table 14 are consistent with the values of $A_{\rm ps}$ in Hinshaw et al. (2007).

Table 14 lists the measured amplitude of the non-Gaussian signals in the 3 year maps. The values are computed for template-cleaned Q-, V-, and W-band maps. With 3 years of data, the limits on primordial non-Gaussianity have improved from $-58 < f_{\rm NL} < 137$ to $-54 < f_{\rm NL} < 114$ at the 95% confidence level. The improvement in limit on $f_{\rm NL}$ is roughly consistent with the expectation that in the signal-dominated regime, $\Delta f_{\rm NL} \propto l_{\rm max}^{-1}$ (Komatsu & Spergel 2001). The level of point source non-Gaussianity in the 3 year maps is lower than in the first-year maps. This drop is due to the more sensitive 3 year masks removing additional sources.

8.4. *Trispectrum*

Motivated by claims that there are large-scale variations in the amplitude of fluctuations, we consider a non-Gaussian model that generates a nontrivial four-point function for the curvature (and temperature) fluctuations but does not produce a three-point function. This model describes a cosmology in which the value

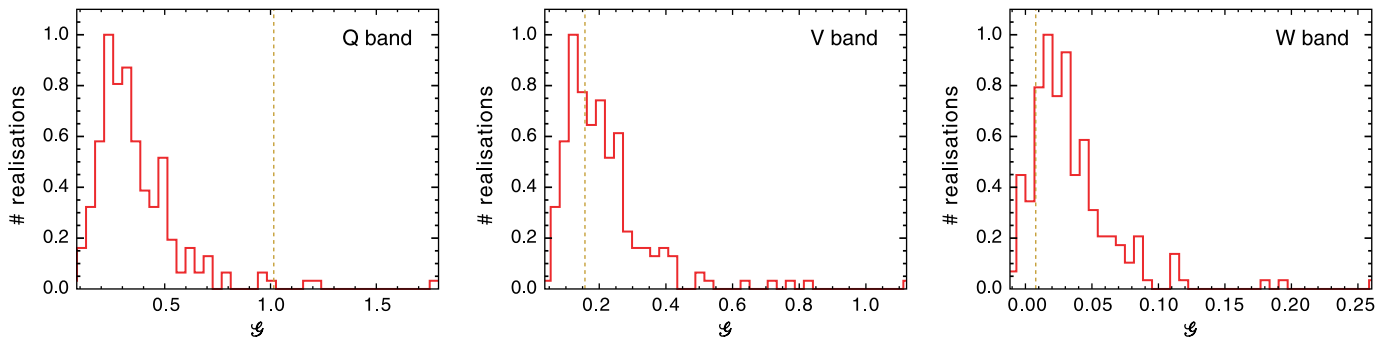

FIG. 25.—Constraints on the amplitude of the four-point function. The measured amplitude of the four-point function (expressed in terms of a non-Gaussian amplitude defined in eq. [23]) is compared to the same statistic computed for simulated Gaussian random fields. The yellow line shows the results for Q, V, and W bands, and the red histogram shows the distribution of the results of the Monte Carlo realizations. Note that in both the simulations and the data A is greater than 0 due to the inhomogeneous noise. The excess in Q is may be due to point source contamination.

of one field modulates the amplitude of fluctuations in a second field:

$$\Phi(\boldsymbol{x}) = \phi(\boldsymbol{x})[1 + g_{\rm NL}\psi(\boldsymbol{x})], \quad (22)$$

where ϕ and ψ are Gaussian random fields and Φ is the Bardeen curvature potential. The presence of such a term would generate variations in the amplitude of fluctuations across the sky.

Appendix B derives an estimator for the amplitude of the non-Gaussian term, $g_{\rm NL}^2|\psi|^2$. This estimator is based on approximating the CMB fluctuations as arising from an infinitely thin surface of last scatter. We measure the amplitude of the four-point function by computing

$$\mathcal{G} = \sum_i (T_i^f \nabla^2 T_i^f - N_i^2)^2, \quad (23)$$

where T^f is a smoothed map (e.g., an $N_{\rm side} = 128$ map), T_i is an unsmoothed map, and N_i is the expected value of $T_f \nabla^2 T_i$ for a map without any signal.

Figure 25 shows measurements of $\mathcal{G}$ from the Q-, V-, and W-band data. The V- and W-band data show any evidence for a nontrivial four-point function, while Q-band data may show the contamination from point sources. At the S/N level of the 3 year data, there are no significant cosmological or systematic effects modulating the amplitude of the fluctuations as a function of scale.

9. CONCLUSIONS

The standard model of cosmology has survived another rigorous set of tests. The errors on the *WMAP* data at large l are now 3 times smaller, and there have been significant improvements in other cosmological measurements. Despite the overwhelming force of the data, the model continues to thrive. This was the basic result of Spergel et al. (2003) and was reinforced by subsequent analyses of the first-year *WMAP* data with the SDSS (Tegmark et al. 2004a) and analysis of first-year *WMAP* plus the final 2dFGRS survey (Sanchez et al. 2006). After the analyses in this paper were completed, a larger SDSS LRG sample was released. An analysis of the 3 year *WMAP* data combined with the new larger sample reached the same basic conclusions as this paper: the ΛCDM model is consistent with both CMB and large-scale structure measurements and its basic parameters are now reasonably well constrained (Tegmark et al. 2006).

The data are so constraining that there is little room for significant modifications of the basic ΛCDM model. The combination of *WMAP* measurements and other astronomical measurements place significant limits on the geometry of the universe, the nature of dark energy, and even neutrino properties. While allowing for a running spectral index slightly improves the fit to the *WMAP* data, the improvement in the fit is not significant enough to require a new parameter.

Cosmology requires new physics beyond the standard model of particle physics: dark matter, dark energy, and a mechanism to generate primordial fluctuations. The *WMAP* data provide insights into all three of these fundamental problems:

1. The clear detection of the predicted acoustic peak structure implies that the dark matter is nonbaryonic.
2. The *WMAP* data are consistent with a nearly flat universe in which the dark energy has an equation of state close to that of a cosmological constant, $w = -1$. The combination of *WMAP* data with measurements of the Hubble constant, baryon oscillations, supernova data, and large-scale structure observations all reinforces the evidence for dark energy.

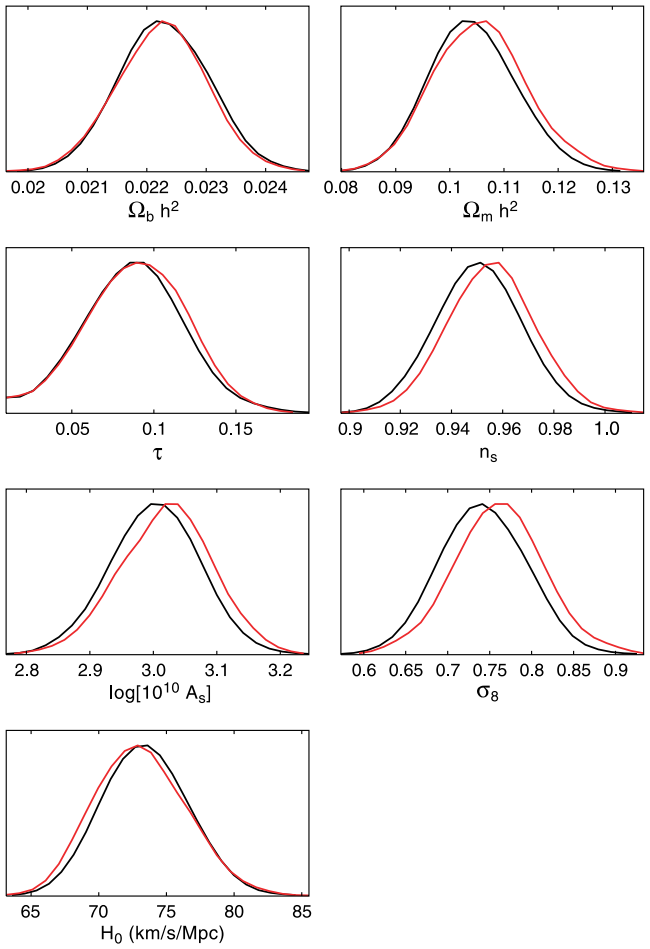

FIG. 26.—Effect of SZ marginalization on the likelihood function. The red curve is the likelihood surface for the 3 year *WMAP* data for the power-law ΛCDM model with $A_{\rm SZ} = 0$. The black curve is the likelihood surface after marginalizing over the amplitude of the SZ contribution.

3. The simplest model for structure formation, a scale-invariant spectrum of fluctuations, is not a good fit to the *WMAP* data. The *WMAP* data require either tensor modes or a spectral index with $n_s < 1$ to fit the angular power spectrum. These observations match the basic inflationary predictions and are well fitted by the predictions of the simple $m^2\phi^2$ model.

Further *WMAP* observations and future analyses will test the inflationary paradigm. While we do not find convincing evidence for significant non-Gaussianities, an alternative model that better fits the low-l data would be an exciting development. Within the context of the inflationary models, measurements of the spectral index as a function of scale and measurements of tensor modes directly will provide a direct probe into the physics of the first moments of the big bang.

The *WMAP* mission is made possible by the support of the Office of Space Sciences at NASA Headquarters and by the hard and capable work of scores of scientists, engineers, technicians, machinists, data analysts, budget analysts, managers, administrative staff, and reviewers. We thank the referee for helpful comments, Henk Hoekstra, Yannick Mellier, and Ludovic Van Waerbeke for providing the CFHTLS data and discussions of the lensing data, John Sievers for discussions of small-scale CMB experiments, Adam Riess and Kevin Kriscinius for discussion of

supernova data, Daniel Eisenstein for discussion of the SDSS LRG data, Max Tegmark for discussions of SDSS P(k) data, and John Peacock for discussions about the 2dFGRS data. E. K. acknowledges support from an Alfred P. Sloan Research Fellowship. H. V. P. is supported by NASA through Hubble Fellowship grant HF-01177.01-A awarded by the Space Telescope Science Institute, which is operated by the Association of Universities for Research in Astronomy, Inc., for NASA under contract NAS 5-26555. This research has made use of NASA's Astrophysics Data System Bibliographic Services, the HEALPix software, CAMB software, and the CMBFAST software. CosmoMC (Lewis & Bridle 2002) was used to produce Figures 1 and 26. We also used CMBWARP software (Jimenez et al. 2004) for initial investigations of the parameter space. This research was additionally supported by NASA LTSA03-000-0090, NASA ADP04-000-0093, NASA ATPNNG04GK55G, and NASA ADP05-0000-092 awards.

APPENDIX A

SZ MARGINALIZATION, PRIORS, AND LIKELIHOOD APPROXIMATIONS

In this Appendix we discuss the affect that various analysis choices have on the estimated cosmological parameters, focusing on the six-parameter ΛCDM model.

The 3 year analysis now accounts for the SZ effect by marginalizing over the amplitude of the SZ contribution, parameterized by the model of Komatsu & Seljak (2002). Specifically, we evaluate their predicted spectrum using $\Omega_m = 0.26$, $\Omega_b = 0.044$, $h = 0.72$, $n_s = 0.97$ and $\sigma_8 = 0.8$. We define the amplitude of the SZ signal (relative to this model) by $A_{\rm SZ}$ and marginalize over this parameter with a flat prior, $0 < A_{\rm SZ} < 2$. This range is based on the assumption that the Komatsu & Seljak (2002) model estimates the true SZ signal with an uncertainty of order 1. Numerical simulations (Nagai 2006) and analytical studies (Reid & Spergel 2006) find a tight correlation between mass and SZ signal, with uncertainties that are dominated by the cluster gas fraction. These results support the Komatsu & Seljak (2002) approach and suggest that the range of this prior is generous. Afshordi et al. (2005) analyze of the SZ signal from 116 nearby clusters in the first-year *WMAP* data and find that the signal from nearby clusters is 30%–40% weaker than expected. Since these nearby clusters are the dominant source of fluctuations in the *WMAP* angular power spectrum, this implies that $A_{\rm SZ} < 1$.

We now use the amplitude of the angular power spectrum peak, C_{220}, rather than A as the amplitude parameter in the Monte Carlo Markov Chains. This choice of prior leads to a slightly lower best-fit amplitude.

Figure 26 shows how the SZ marginalization and the change in amplitude prior affect our estimates of cosmological parameters. Except for σ_8, the effects are all relatively small. For σ_8 we estimate that roughly half of this change is due to the SZ marginalization and half is due to the change in amplitude prior. Lewis (2006) provides a detailed study of the effects of gravitational lensing on the analysis and show that it is smaller than the SZ effect.

Since the first draft of this paper was circulated, it has been pointed out (Eriksen et al. 2007) that the pseudo-C_l-based power spectrum is biased slightly high in the range $12 < l < 30$, which in turn biases the spectral index, n_s, slightly low. As a result, we have increased the sky map resolution used in our exact TT likelihood module (to $N_{\rm side} = 16$), which allows us to use this form up to $l = 30$. We have established that this approach agrees well with an independent exact form based on Gibbs sampling methodology (Eriksen et al. 2007).

Huffenberger et al. (2006) argue that the point source amplitude quoted in the original version of Hinshaw et al. (2007) was too high: they find $A_{\rm ps} = 0.011 \pm 0.001$, while Hinshaw et al. (2007) originally quoted $A_{\rm ps} = 0.017 \pm 0.002$. Subsequently, Hinshaw et al. (2007) have reanalyzed the source contribution and now favor an intermediate value with a more conservative error, $A_{\rm ps} = 0.014 \pm 0.003$. The original source correction also had the effect of biasing the spectral index slightly low.

Table 15 shows the sensitivity of the spectral index, n_s, to the various treatments discussed above. The first row (Fiducial) gives the result originally quoted in this paper. The second row (No SZ correction) gives the result if we assume $A_{\rm SZ} = 0$. The third row (No beam error) shows the effect of assuming the beam window function has no error. The fourth row (Lower point source amplitude) shows the change induced by changing the source amplitude (and its uncertainty) from 0.017 ± 0.002 to 0.014 ± 0.003. The sixth row (Foreground marginalization) shows the effect of disabling marginalization over the foreground emission template in the exact likelihood module (up to $l = 12$). The seventh row (Res 4 likelihood) shows the effect of using the exact likelihood module to $l = 30$, and the last row shows our current best estimate of n_s.

The detailed form of the likelihood function and the treatment of point sources and the SZ effect has a $\sim 0.5\,\sigma$ effect on the best-fit slope. We have also used simulations where we know the input model to check the effects of including various secondary effects. Lewis (2006) provides a detailed study of the effects of gravitational lensing on the analysis and show that it is smaller than the SZ effect.

TABLE 15

Sensitivity of Slope to Likelihood Model and Prior

Treatment	Result
Fiducial ($N_{\rm side} = 8$ likelihood, $A_{\rm ps} = 0.017$)	0.951 ± 0.016
No SZ correction	0.954 ± 0.016
No beam error	0.953 ± 0.016
Reduced point source amplitude ($A_{\rm ps} = 0.014$)	0.955 ± 0.016
Huffenberger et al. (2006) point source amplitude ($A_{\rm ps} = 0.011$)	0.957 ± 0.016
Foreground marginalization	0.953 ± 0.016
$N_{\rm side} = 16$ likelihood	0.957 ± 0.016
$N_{\rm side} = 16$ likelihood + $A_{\rm ps} = 0.014$ + no SZ correction	0.960 ± 0.016
$N_{\rm side} = 16$ likelihood + $A_{\rm ps} = 0.014$	0.958 ± 0.016

APPENDIX B

TRISPECTRUM METHODOLOGY

B1. PREDICTED TRISPECTRUM SIGNAL

We consider here a model that generates a nontrivial trispectrum, but no bispectrum signal. We assume that the gravitational potential Φ is a product of two independent Gaussian fields, ϕ and ψ:

$$\Phi(\boldsymbol{x}) = \phi(\boldsymbol{x})[1 + g_{\rm NL}\psi(\boldsymbol{x})], \tag{B1}$$

where $g_{\rm NL}$ characterizes the strength of the nonlinear term.

Following Komatsu et al. (2005) approach for the bispectrum, extended recently to the trispectrum in Kogo & Komatsu (2006) the observed temperature multipoles are

$$a_{lm} = b_l \int r^2 dr \Phi_{lm}(r)\alpha_l(r) + n_{lm}, \tag{B2}$$

where b_l is the beam, n_{lm} is the noise, and $\alpha_l(r)$ is the radiation transfer function:

$$\alpha_l(r) = \frac{2}{\pi}\int k^2 dk g_{Tl}(k) j_l(kr). \tag{B3}$$

The nonlinear coupling term generates a second-order term:

$$a_{lm} = n_{lm} + b_l \int r^2 dr \alpha_l(r)\left[\phi_{lm}(r) + \phi_{l'm'}(r)\psi_{l''m''}(r)C_{lm}^{l'm'l''m''}\right], \tag{B4}$$

where

$$C_{lm}^{l'm'l''m''} = \sqrt{\frac{4\pi}{(2l+1)(2l'+1)(2l''+1)}}\begin{pmatrix} l & l' & l'' \\ 0 & 0 & 0 \end{pmatrix}\begin{pmatrix} l & l' & l'' \\ m & m' & m'' \end{pmatrix}. \tag{B5}$$

This term does not have any effect on the bispectrum as $\langle\phi^3\rangle = 0$ and $\langle\psi^3\rangle = 0$. However, it does have a nontrivial effect on the trispectrum.

As with gravitational lensing (see Hu 2001), the largest trispectrum term is the diagonal term, $T_{ll}^{ll}(0) = \langle C_l C_l\rangle - 3\langle C_l\rangle^2$. This term would generate an excess in the χ^2 of the fit of the model to the data:

$$T_{ll}^{ll}(0) = g_{\rm NL}^2 C_l \int r^2 dr \int \tilde{r}^2 d\tilde{r}\alpha_l(r)\alpha_l(\tilde{r}) \times \sum_{ml'm'l''m''}\sum_{\tilde{l}'\tilde{m}'\tilde{l}''\tilde{m}''}\left\langle\phi_{l'm'}(r)\phi_{\tilde{l}'\tilde{m}'}(\tilde{r})\right\rangle\left\langle\psi_{l''m''}(r)\psi_{\tilde{l}''\tilde{m}''}(\tilde{r})\right\rangle C_{lm}^{l'm'l''m''} C_{lm}^{\tilde{l}'\tilde{m}'\tilde{l}''\tilde{m}''}. \tag{B6}$$

We can then use

$$\left\langle\phi_{l'm'}(r)\phi_{\tilde{l}'\tilde{m}'}(\tilde{r})\right\rangle = \delta_{l'\tilde{l}'}\delta_{m'\tilde{m}'}\int k^2 dk P_\phi(k) j_{l'}(kr) j_{l'}(k\tilde{r}), \tag{B7}$$

and the equivalent relationship for ψ to rewrite the trispectrum as

$$T_{ll}^{ll}(0) = g_{\rm NL}^2 \xi_l C_l^2, \tag{B8}$$

where

$$\xi_l = \frac{4\pi}{C_l}\int k^2 dk P_\phi(k)\int (k')^2 dk' P_\psi(k') \times \begin{pmatrix} l & l' & l'' \\ 0 & 0 & 0 \end{pmatrix}^2 \int r^2 dr \int \tilde{r}^2 d\tilde{r}\alpha_l(r)\alpha_l(\tilde{r}) j_{l'}(kr) j_{l''}(k'r) j_{l'}(k\tilde{r}) j_{l''}(k'\tilde{r}). \tag{B9}$$

While this full integral is numerically intractable, we approximate the surface of last scatter as a thin screen so that

$$a_{lm} = b_l \Phi_{lm}(r_*)\boldsymbol{\alpha}_l + n_{lm}; \tag{B10}$$

then, the trispectrum coupling term reduces to

$$\xi_l = \frac{4\pi\alpha_l^2}{C_l}\int k^2 dk P_\phi(k) j_{l'}^2(kr_*)\int k'^2 dk' P_\psi(k') j_{l''}^2(k'r_*)\begin{pmatrix} l & l' & l'' \\ 0 & 0 & 0\end{pmatrix}^2. \tag{B11}$$

Recall that in this limit,

$$C_l = \alpha_l^2\int k^2 dk P_\phi(k) j_l^2(kr_*). \tag{B12}$$

Thus,

$$\xi_l = \frac{4\pi\alpha_l^2 C_{l'}}{\bar{\alpha}_{l'}^2 C_l}\int k'^2 dk' P_\psi(k') j_{l''}^2(k'r_*)\begin{pmatrix} l & l' & l'' \\ 0 & 0 & 0\end{pmatrix}^2. \tag{B13}$$

The amplitude of ξ_l is, thus, roughly the variance in the ψ field on the scale r_*/l. Note that ξ_l is a positive definite quantity so that $T_{ll}^{ll}(0)$ should be always positive.

B2. DETECTING THE NON-GAUSSIAN SIGNAL

If we assume that ξ_l is constant, then we can follow Hu (2001) and compute an optimal quadratic statistic. We approximate the optimal statistic as $\sum_i (T_i^f \nabla^2 T_i^f - N_i^2)^2$, where T^f is a smoothed map (e.g., a res 7 map) and we use the approximation that $C_l = A/l(l+1)$. This has the advantage that we can easily compute it and it has well-defined noise properties.

B2.1. *Practical Implementations*

We define for this purpose the dimensionless $\mathcal{G}$ statistic as

$$\begin{aligned}\mathcal{G} = &\sum_{p,b_1,b_2,b_3,b_4} w_{p,b_1}\hat{T}_{p,b_1} w_{p,b_2}\hat{T}_{p,b_2} w_{p,b_3}\hat{T}_{p,b_3} w_{p,b_4}\hat{T}_{p,b_4} \\ &- \sum_{b_1,b_2,b_3,b_4}\Big(\sum_{p_1} w_{p_1,b_1}\hat{T}_{p_1,b_1} w_{p_1,b_2}\hat{T}_{p_1,b_2}\Big)\Big(\sum_{p_2} w_{p_2,b_1}\hat{T}_{p_2,b_1} w_{p_2,b_2}\hat{T}_{p_2,b_2}\Big),\end{aligned} \tag{B14}$$

where b_i refers to various bands (Q, V, and W for year 1, year 2, and year 3) that are all distinct for a single term so that the noise bias is null for this statistic, w_{p,b_i} is a particular pixel weight (we will consider it equal unity first) and $\hat{T}_b$ is a filtered map defined as

$$\hat{T}_{pb} = \frac{T_{pb}}{\sqrt{\sum_q T_{qb}^2}}, \tag{B15}$$

$$T_{pb} = \sum_{lm} f_{lb}\tilde{a}_{lmb}^M Y_{lm}(\hat{\boldsymbol{n}}_p), \tag{B16}$$

where $\tilde{a}_{lm}^M$ values are the spherical harmonic coefficients of the masked sky. We use at this level the Kp12 mask to hide the brighter part of the galaxy (and potentially the brighter point sources) and ignore cut sky effects in considering those pseudo-a_{lm} values. But when computing the sum over pixels in $\mathcal{G}$, we consider only pixels outside the Kp2 area. The obvious advantage of this simple real space statistic is its ability to handle inhomogeneous noise and to localize its various contributions in real space. The second term in the definition of $\mathcal{G}$ aims at subtracting off the Gaussian unconnected part, so that if the $\hat{T}$ fields are homogeneous Gaussian fields, we obtain $\langle \mathcal{G}^{\rm ps}\rangle = 0$.

The exact nature of f_l will depend on the source of the signal. For example, point sources do contribute to all n-points functions in real or harmonic space and are as such visible in the power spectrum, bispectrum, and trispectrum. The first two have been used to set limits and corrections.

Should we want to isolate the point sources contribution with the $\mathcal{G}$ statistic, we would proceed in the following manner. The point sources power spectrum is well approximated by a constant, white noise–like, power spectrum $C_l^{\rm ps}$ (see Komatsu et al. 2003). Given the measured power spectrum, $\tilde{C}_l = C_l b_l^2 + C_l^{\rm ps} b_l^2 + N_l$, the Wiener like filter to reconstruct point sources is to $f_l^{\rm ps} = b_l^2/\tilde{C}_l$. Note that this filter would be optimal only if point sources were drawn from a Gaussian distribution, which is not true. We can, however, expect it to be close to optimal.

In order to constrain the CMB contribution to the trispectrum and constrain $g_{\rm NL}$ close to optimality, we will set f_{l1} and f_{l2} to the Wiener filter for the CMB field, $f_{l1} = f_{l3} = C_l^{\rm theory} b_l^2/C_l^{\rm measured}$ and $f_{l2} = f_{l4} = l(l+1)f_{l1}$, where $C_l^{\rm theory}$ is the best-fit model angular power spectrum and $C_l^{\rm measured}$ is the measured raw power spectrum including the signal and the noise and not corrected for the beam window function.

We restrict ourselves to a unit weighting that is nearly optimal in the signal-dominated regime where we draw our conclusions from, i.e., at resolution lower than $N_{\rm side} = 64$.

B2.2. *Explicit relation to the trispectrum*

Ignoring the weights and using the identities from Komatsu (2001)

$$\langle T_1(\hat{\boldsymbol{n}})T_2(\hat{\boldsymbol{n}})T_3(\hat{\boldsymbol{n}})T_4(\hat{\boldsymbol{n}})\rangle_c = \sum_p T_{1p}T_{2p}T_{3p}T_{4p} \tag{B17}$$

$$= \sum_{l_1m_1l_2m_2l_3m_3l_4m_4} \langle t_{l_1m_1}t_{l_2m_2}t^*_{l_3m_3}t^*_{l_4m_4}\rangle_c \times \int d\Omega(\hat{\boldsymbol{n}})Y_{l_1m_1}(\hat{\boldsymbol{n}})Y_{l_2m_2}(\hat{\boldsymbol{n}})Y^*_{l_3m_3}(\hat{\boldsymbol{n}})Y^*_{l_4m_4}(\hat{\boldsymbol{n}}) \tag{B18}$$

$$= \sum_{l_1m_1l_2m_2l_3m_3l_4m_4LM} \sqrt{\frac{(2l_1+1)(2l_2+1)}{4\pi(2L+1)}}\sqrt{\frac{(2l_3+1)(2l_4+1)}{4\pi(2L+1)}} \times C^{L0}_{l_10l_20}C^{L0}_{l_30l_40}C^{LM}_{l_1m_1l_2m_2}\langle t_{l_1m_1}t_{l_2m_2}t^*_{l_3m_3}t^*_{l_4m_4}\rangle_c \, . \, C^{LM}_{l_3m_3l_4m_4} \tag{B19}$$

It is then easy to relate to standard expression for the connected part of the trispectrum as in Hu (2001) and Komatsu (2001).

REFERENCES

Abazajian, K., et al. 2005, ApJ, 625, 613
Abroe, M. E., et al. 2004, ApJ, 605, 607
Afshordi, N. 2004, Phys. Rev. D, 70, 083536
Afshordi, N., Lin, Y.-T., & Sanderson, A. J. R. 2005, ApJ, 629, 1
Afshordi, N., Loh, Y.-S., & Strauss, M. A. 2004, Phys. Rev. D, 69, 083524
Albrecht, A., & Steinhardt, P. J. 1982, Phys. Rev. Lett., 48, 1220
Alishahiha, M., Silverstein, E., & Tong, D. 2004, Phys. Rev. D, 70, 123505
Allen, S. W., Schmidt, R. W., Ebeling, H., Fabian, A. C., & van Speybroeck, L. 2004, MNRAS, 353, 457
Allen, S. W., Schmidt, R. W., Fabian, A. C., & Ebeling, H. 2003, MNRAS, 342, 287
Amendola, L. 1999, Phys. Rev. D, 60, 043501
Arkani-Hamed, N., Creminelli, P., Mukohyama, S., & Zaldarriaga, M. 2004, J. Cosmol. Astropart. Phys., 4, 1
Asplund, M., Nissen, P. E., Lambert, D. L., Primas, F., & Smith, V. V. 2005, in IAU Symposium, ed. V. Hill, P. François, & F. Primas (Cambridge: Cambridge Univ. Press), 53
Astier, P., et al. 2005, BAAS, 37, 1176
Aurich, R., Lustig, S., Steiner, F., & Then, H. 2005, Phys. Rev. Lett., 94, 021301
Babich, D., Creminelli, P., & Zaldarriaga, M. 2004, J. Cosmol. Astropart. Phys., 8, 9
Bahcall, N. A., & Bode, P. 2003, ApJ, 588, L1
Bahcall, N. A., Ostriker, J. P., Perlmutter, S., & Steinhardt, P. J. 1999, Science, 284, 1481
Bania, T. M., Rood, R. T., & Balser, D. S. 2002, Nature, 415, 54
Bardeen, J. M., Bond, J. R., Kaiser, N., & Szalay, A. S. 1986, ApJ, 304, 15
Bardeen, J. M., Steinhardt, P. J., & Turner, M. S. 1983, Phys. Rev. D, 28, 679
Barger, V., Kneller, J. P., Lee, H.-S., Marfatia, D., & Steigman, G. 2003, Phys. Lett. B, 566, 8
Barger, V., Marfatia, D., & Tregre, A. 2004, Phys. Lett. B, 595, 55
Bartolo, N., Komatsu, E., Matarrese, S., & Riotto, A. 2004a, Phys. Rep. 402, 103
Bartolo, N., Matarrese, S., & Riotto, A. 2004b, J. High Energy Phys., 4, 6
Bashinsky, S., & Seljak, U. 2004, Phys. Rev. D, 69, 083002
Bean, R., & Dore, O. 2004, Phys. Rev. D, 69, 083503
Bean, R., & Magueijo, J. 2001, Phys. Lett. B, 517, 177
Beltrán, M., García-Bellido, J., Lesgourgues, J., Liddle, A. R., & Slosar, A. 2005, Phys. Rev. D, 71, 063532
Bennett, C. L., et al. 2003, ApJS, 148, 1
Bergström, L., & Danielsson, U. H. 2002, J. High Energy Phys., 12, 38
Blanchard, A., Douspis, M., Rowan-Robinson, M., & Sarkar, S. 2003, A&A, 412, 35
Boesgaard, A. M., Stephens, A., & Deliyannis, C. P. 2005, ApJ, 633, 398
Bonamente, M., Joy, M., La Roque, S. Carlstrom, J., Reese, E., Dawson, K. 2006, ApJ, 647, 25
Bond, J. R., & Efstathiou, G. 1984, ApJ, 285, L45
———. 1987, MNRAS, 226, 655
Bond, J. R., Efstathiou, G., & Silk, J. 1980, Phys. Rev. Lett., 45, 1980
Bond, J. R., Pogosyan, D., & Souradeep, T. 2000, Phys. Rev. D, 62, 043005
Bond, J. R., & Szalay, A. S. 1983, ApJ, 274, 443
Bond, J. R., et al. 2005, ApJ, 626, 12
Borgani, S., et al. 2001, ApJ, 561, 13
Boughn, S., & Crittenden, R. 2004, Nature, 427, 45
Boughn, S. P., & Crittenden, R. G. 2005, MNRAS, 360, 1013
Bowen, R., Hansen, S. H., Melchiorri, A., Silk, J., & Trotta, R. 2002, MNRAS, 334, 760
Bridges, M., Lasenby, A. N., & Hobson, M. P. 2006, MNRAS, 369, 1123
Bucher, M., & Spergel, D. 1999, Phys. Rev. D, 60, 043505
Burgess, C. P., Cline, J. M., Lemieux, F., & Holman, R. 2003, J. High Energy Phys., 2, 48
Cabella, P., Hansen, F., Marinucci, D., Pagano, D., & Vittorio, N. 2004, Phys. Rev. D, 69, 063007
Caldwell, R. R., Dave, R., & Steinhardt, P. J. 1998, Phys. Rev. Lett., 80, 1582
Carroll, S. M., Press, W. H., & Turner, E. L. 1992, ARA&A, 30, 499
Cen, R. 2003, ApJ, 591, L5
Chaboyer, B., & Krauss, L. M. 2002, ApJ, 567, L45
Chae, K.-H., et al. 2002, Phys. Rev. Lett., 89, 151301
Charbonnel, C., & Primas, F. 2005, A&A, 442, 961
Chiang, L., Naselsky, P. D., Verkhodanov, O. V., & Way, M. J. 2003, ApJ, 590, L65
Chiu, W. A., Fan, X., & Ostriker, J. P. 2003, ApJ, 599, 759
Ciardi, B., Ferrara, A., & White, S. D. M. 2003, MNRAS, 344, L7
Clocchiatti, A., et al. 2006, ApJ, 642, 1
Coc, A., Vangioni-Flam, E., Descouvemont, P., Adahchour, A., & Angulo, C. 2004, ApJ, 600, 544
Cole, S., et al. 2005, MNRAS, 362, 505
Colley, W. N., & Gott, J. R. 2003, MNRAS, 344, 686
Contaldi, C. R., Hoekstra, H., & Lewis, A. 2003, Phys. Rev. Lett., 90, 221303
Copi, C. J., Huterer, D., & Starkman, G. D. 2004, Phys. Rev. D, 70, 043515
Corasaniti, P.-S., Giannantonio, T., & Melchiorri, A. 2005, Phys. Rev. D, 71, 123521
Cornish, N. J., Spergel, D. N., & Starkman, G. D. 1996, Phys. Rev. Lett., 77, 215
Cornish, N. J., Spergel, D. N., Starkman, G. D., & Komatsu, E. 2004, Phys. Rev. Lett., 92, 201302
Creminelli, P., Nicolis, A., Senatore, L., Tegmark, M., & Zaldarriaga, M. 2006, J. Cosmol. Astropart. Phys., 5, 4
Crighton, N. H. M., Webb, J. K., Ortiz-Gil, A., & Fernández-Soto, A. 2004, MNRAS, 355, 1042
Crittenden, R. G., & Turok, N. 1996, Phys. Rev. Lett., 76, 575
Croft, R. A. C., Weinberg, D. H., Katz, N., & Hernquist, L. 1998, ApJ, 495, 44
Crotty, P., Lesgourgues, J., & Pastor, S. 2003, Phys. Rev. D, 67, 123005
Cruz, M., Martínez-González, E., Vielva, P., & Cayón, L. 2005, MNRAS, 356, 29
Cruz, M., Cayon, L, Martinez-Gonzalez, E., Vielva, P., & Jin, J. 2006, ApJ, 655, 11
Danielsson, U. H. 2002, Phys. Rev. D, 66, 023511
Deffayet, C. 2001, Phys. Lett. B, 502, 199
Deffayet, C., Dvali, G., & Gabadadze, G. 2002, Phys. Rev. D, 65, 044023
Desjacques, V., & Nusser, A. 2005, MNRAS, 361, 1399
Dickinson, C., et al. 2004, MNRAS, 353, 732
Dolgov, A. D., Hansen, S. H., & Semikoz, D. V. 1999, Nucl. Phys. B, 543, 269
Dunkley, J., Bucher, M., Ferreira, P. G., Moodley, K., & Skordis, C. 2005, MNRAS, 356, 925
Dunlop, J., Peacock, J., Spinrad, H., Dey, A., Jimenez, R., Stern, D., & Windhorst, R. 1996, Nature, 381, 581
Dvali, G., Gruzinov, A., & Zaldarriaga, M. 2004, Phys. Rev. D, 69, 083505

Easther, R., Greene, B. R., Kinney, W. H., & Shiu, G. 2002, Phys. Rev. D, 66, 023518
Easther, R., Kinney, W. H., & Peiris, H. 2005a, J. Cosmol. Astropart. Phys., 5, 9
———. 2005b, J. Cosmol. Astropart. Phys., 8, 1
Efstathiou, G. 2004, MNRAS, 348, 885
Eisenstein, D. J., et al. 2005, ApJ, 633, 560
Elgarøy, Ø., & Lahav, O. 2003, J. Cosmol. Astropart. Phys., 4, 4
Ellis, J., Olive, K. A., & Vangioni, E. 2005, Phys. Lett. B, 619, 30
Eriksen, H. K., Hansen, F. K., Banday, A. J., Górski, K. M., & Lilje, P. B. 2004a, ApJ, 605, 14
Eriksen, H. K., Banday, A. J., Górski, K. M., & Lilje, P. B. 2004b, ApJ, 612, 633
Eriksen, H. K. et al. 2007, ApJ, 656, 641
Ettori, S., Tozzi, P., & Rosati, P. 2003, A&A, 398, 879
Fan, X., et al. 2006, AJ, 131, 1203
Feldman, H., et al. 2003, ApJ, 596, L131
Ferreira, P. G., & Joyce, M. 1998, Phys. Rev. D, 58, 023503
Fields, B. D., Olive, K. A., & Vangioni-Flam, E. 2005, ApJ, 623, 1083
Fosalba, P., & Gaztañaga, E. 2004, MNRAS, 350, L37
Freedman, W. L., et al. 2001, ApJ, 553, 47
Gaztañaga, E., & Wagg, J. 2003, Phys. Rev. D, 68, 021302
Gelman, A., & Rubin, D. 1992, Statistical Sci., 7, 457
Gnedin, N. Y., & Gnedin, O. Y. 1998, ApJ, 509, 11
Gnedin, N. Y., & Hamilton, A. J. S. 2002, MNRAS, 334, 107
Goldberg, D. M., & Spergel, D. N. 1999, Phys. Rev. D, 59, 103002
Goobar, A., Hannestad, S., Mortsell, E., & Tu, H. 2006, J. Cosmol. Astropart. Phys., 6, 19
Gott, J. R. I., Park, C., Juszkiewicz, R., Bies, W. E., Bennett, D. P., Bouchet, F. R., & Stebbins, A. 1990, ApJ, 352, 1
Grainge, K., et al. 2003, MNRAS, 341, L23
Guth, A. H. 1981, Phys. Rev. D, 23, 347
Guth, A. H., & Pi, S. Y. 1982, Phys. Rev. Lett., 49, 1110
Haiman, Z., & Holder, G. P. 2003, ApJ, 595, 1
Hajian, A., Souradeep, T., & Cornish, N. 2005, ApJ, 618, L63
Hall, L. J., & Oliver, S. 2004, Nucl. Phys. B Proc. Supp., 137, 269
Hall, L. M. H., Moss, I. G., & Berera, A. 2004, Phys. Rev. D, 69, 083525
Hamuy, M., Phillips, M. M., Suntzeff, N. B., Schommer, R. A., Maza, J., & Aviles, R. 1996, AJ, 112, 2391
Hannestad, S. 2001, Phys. Rev. D, 64, 083002
———. 2003, J. Cosmol. Astropart. Phys., 5, 4
———. 2006, J. Cosmol. Astropart. Phys., 1, 1
Hansen, F. K., Cabella, P., Marinucci, D., & Vittorio, N. 2004, ApJ, 607, L67
Hawking, S. W. 1982, Phys. Lett., B115, 295
Henry, J. P. 2004, ApJ, 609, 603
Heymans, C., et al. 2005, MNRAS, 361, 160
Hinshaw, G., et al. 2003, ApJS, 148, 135
———. 2007, ApJS, 170, 288
Hoekstra, H., Yee, H. K. C., & Gladders, M. D. 2002, ApJ, 577, 595
Hoekstra, H., et al. 2006, ApJ, 647, 116 (Ho06)
Hoffman, M. B., & Turner, M. S. 2001, Phys. Rev. D, 64, 023506
Hu, W. 1998, ApJ, 506, 485
———. 2001, in RESCEU 1999, Birth and Evolution of the Universe, ed. K. Sato & M. Kawasaki (Tokyo: Universal Academy Press), 131
Hu, W., Eisenstein, D. J., & Tegmark, M. 1998, Phys. Rev. Lett., 80, 5255
Hu, W., Fukugita, M., Zaldarriaga, M., & Tegmark, M. 2001, ApJ, 549, 669
Hu, W., & Holder, G. P. 2003, Phys. Rev., D68, 023001
Huffenberger, K. M., Eriksen, H. K., & Hansen, F. K. 2006, ApJ, 651, L81
Huffenberger, K. M., Seljak, U., & Makarov, A. 2004, Phys. Rev. D, 70, 063002
Hwang, J., & Noh, H. 1998, Phys. Rev. Lett., 81, 5274
Ichikawa, K., Fukugita, M., & Kawasaki, M. 2005, Phys. Rev. D, 71, 043001
Iliev, I. T., Mellema, G., Pen, U.-L., Merz, H., Shapiro, P. R., & Alvarez, M. A. 2005, in IAU Colloq. 199, ed. P. R. Williams, C.-G. Shu, & B. Menard (Cambridge: Cambridge Univ. Press), 369
Inoue, K. T., Tomita, K., & Sugiyama, N. 2000, MNRAS, 314, L21
Jarosik, N., et al. 2007, ApJS, 170, 263
Jarvis, M., Bernstein, G. M., Fischer, P., Smith, D., Jain, B., Tyson, J. A., & Wittman, D. 2003, AJ, 125, 1014
Jedamzik, M. 2004, Phys. Rev. D, 70, 063524
Jedamzik, K., Choi, K.-Y.,Roszkowski, L., & Ruiz de Austri, R. 2005, preprint (hep-ph/0512044)
Jena, T., et al. 2005, MNRAS, 361, 70
Jimenez, R., Verde, L., Peiris, H., & Kosowsky, A. 2004, Phys. Rev., D70, 023005
Jimenez, R., Verde, L., Treu, T., & Stern, D. 2003, ApJ, 593, 622
Jones, W. C., et al. 2006, ApJ, 647, 823
Kaloper, N., Kleban, M., Lawrence, A., Shenker, S., & Susskind, L. 2002, J. High Energy Phys., 11, 37
Kaplinghat, M., Chu, M., Haiman, Z., Holder, G. P., Knox, L., & Skordis, C. 2003, ApJ, 583, 24
Kawasaki, M., Yamaguchi, M., & Yokoyama, J. 2003, Phys. Rev. D, 68, 023508
Khoury, J., Ovrut, B. A., Seiberg, N., Steinhardt, P. J., & Turok, N. 2002, Phys. Rev., D65, 086007
Khoury, J., Ovrut, B. A., Steinhardt, P. J., & Turok, N. 2001, Phys. Rev., D64, 123522
Kinney, W. H. 2002, Phys. Rev., D66, 083508
Kirkman, D., Tytler, D., Suzuki, N., O'Meara, J. M., & Lubin, D. 2003, ApJS, 149, 1
Kneller, J. P., & Steigman, G. 2004, New J. Phys., 6, 117
Knop, R. A., et al. 2003, ApJ, 598, 102
Knox, L., Christensen, N., & Skordis, C. 2001, ApJ, 563, L95
Kogo, N., & Komatsu, E. 2006, Phys. Rev. D, 73, 3007
Kogut, A., et al. 2003, ApJS, 148, 161
Komatsu, E. 2001, Ph.D. thesis, Tohoku Univ. (astro-ph/0206039)
Komatsu, E., & Futamase, T. 1999, Phys. Rev. D, 59, 064029
Komatsu, E., & Kitayama, T. 1999, ApJ, 526, L1
Komatsu, E., & Seljak, U. 2001, MNRAS, 327, 1353
———. 2002, MNRAS, 336, 1256
Komatsu, E., & Spergel, D. N. 2001, Phys. Rev. D, 63, 63002
Komatsu, E., Spergel, D. N., & Wandelt, B. D. 2005, ApJ, 634, 14
Komatsu, E., et al. 2003, ApJS, 148, 119
Koopmans, L. V. E., Treu, T., Fassnacht, C. D., Blandford, R. D., & Surpi, G. 2003, ApJ, 599, 70
Kosowsky, A., Milosavljevic, M., & Jimenez, R. 2002, Phys. Rev. D, 66, 63007
Krisciunas, K., et al. 2005, AJ, 130, 2453
Kuo, C. L., et al. 2004, ApJ, 600, 32
Krauss, L. M., & Turner, M. S. 1999, Gen. Relativ. Gravitation, 31, 1453
Lahav, O., Rees, M. J., Lilje, P. B., & Primack, J. R. 1991, MNRAS, 251, 128
Larena, J., Alimi, J.-M., & Serna, A. 2005, preprint (astro-ph/0511693)
Larson, D. L., & Wandelt, B. D. 2004, ApJ, 613, L85
Leach, S. M., & Liddle, A. R. 2003, Phys. Rev. D, 68, 123508
Leitch, E. M., Kovac, J. M., Halverson, N. W., Carlstrom, J. E., Pryke, C., & Smith, M. W. E. 2005, ApJ, 624, 10
Levin, J. J., Barrow, J. D., Bunn, E. F., & Silk, J. 1997, Phys. Rev. Lett., 79, 974
Lewis, A., & Bridle, S. 2002, Phys. Rev. D, 66, 103511
Lewis, A., Challinor, A., & Lasenby, A. 2000, ApJ, 538, 473
Lewis, A. 2006, preprint (astro-ph/0603753)
Lewis, A., & Challinor, A. 2006, Phys. Rep., 429, 1
Liddle, A. R., & Lyth, D. H. 1992, Phys. Lett., B291, 391
———. 1993, Phys. Rept., 231, 1
Linde, A. 2005, NewA Rev., 49, 35
Linde, A. D. 1982, Phys. Lett. B, 108, 389
Luminet, J., Weeks, J. R., Riazuelo, A., Lehoucq, R., & Uzan, J. 2003, Nature, 425, 593
Lyth, D. H., & Riotto, A. 1999, Phys. Rep., 314, 1
Lyth, D. H., Ungarelli, C., & Wands, D. 2003, Phys. Rev. D, 67, 23503
Ma, C.-P. 1996, ApJ, 471, 13
Madau, P., Rees, M. J., Volonteri, M., Haardt, F., & Oh, S. P. 2004, ApJ, 604, 484
Maldacena, J. 2003, J. High Energy Phys., 5, 13
Mangano, G., Miele, G., Pastor, S., & Peloso, S. 2002, Phys. Lett. B, 534, 8
Mangano, G., Miele, G., Pastor, S., Pinto, T., Pisanti, O., & Serpico, P. D. 2005, Nucl. Phys. B, 729, 221
Malhotra, S., & Rhoads, J. E. 2004, ApJ, 617, L5
Martin, J., & Brandenberger, R. H. 2001, Phys. Rev. D, 63, 123501
———. 2003, Phys. Rev. D, 68, 063513
Martin, J., & Ringeval, C. 2004, Phys. Rev. D, 69, 083515
Mason, B. S., et al. 2003, ApJ, 591, 540
Mathews, G. J., Kajino, T., & Shima, T. 2005, Phys. Rev. D, 71, 021302
McDonald, P., et al. 2005, ApJ, 635, 761
McGaugh, S. S. 2004, ApJ, 611, 26
Mecke, K. R., Buchert, T., & Wagner, H. 1994, A&A, 288, 697
Meiksin, A., & White, M. 2004, MNRAS, 350, 1107
Meléndez, J., & Ramírez, I. 2004, ApJ, 615, L33
Minkowski, H. 1903, Mathematische Ann., 57, 447
Mohapatra, R. N., et al. 2005, preprint
Mohayaee, R., & Tully, B. 2005, ApJ, 635, L113
Montroy, T. E., et al. 2006, ApJ, 647, 813
Mukhanov, V. F., & Chibisov, G. V. 1981, J. Exp. Theor. Phys. Lett., 33, 532
Mukherjee, P., Parkinson, D., & Liddle, A. R. 2006, ApJ, 638, L51
Mukherjee, P., & Wang, Y. 2003, ApJ, 599, 1
Nagai, D. 2006, ApJ, 650, 538
Naselsky, P. D., Chiang, L.-Y., Novikov, I. D., & Verkhodanov, O. V. 2005, Int. J. Mod. Phys. D, 14, 1273
Nobili, S., et al. 2005, A&A, 437, 789
Nolta, M. R., et al. 2004, ApJ, 608, 10

Novosyadlyj, B., Durrer, R., & Lukash, V. N. 1999, A&A, 347, 799 (NDL)
O'Dwyer, I. J., et al. 2004, ApJ, 617, L99
———. 2005, ApJS, 158, 93
Oguri, M. 2004, Ph.D. thesis, Univ. Tokyo
Oh, S. P., & Haiman, Z. 2003, MNRAS, 346, 456
Olive, K. A., & Skillman, E. D. 2004, ApJ, 617, 29
Ostriker, J. P., & Steinhardt, P. J. 1995, Nature, 377, 600
Padmanabhan, N., Hirata, C. M., Seljak, U., Schlegel, D. J., Brinkmann, J., & Schneider, D. P. 2005, Phys. Rev. D, 72, 043525
Page, L., et al. 2003a, ApJS, 148, 39
———. 2003b, ApJS, 148, 233
———. 2007, ApJS, 170, 335
Park, C. 2004, MNRAS, 349, 313
Pearson, T. J., et al. 2003, ApJ, 591, 556
Peebles, P. J. E. 1984, ApJ, 284, 439
Peebles, P. J., & Ratra, B. 2003, Rev. Mod. Phys., 75, 559
———. 1988, ApJ, 325, L17
Peebles, P. J. E., & Yu, J. T. 1970, ApJ, 162, 815
Peiris, H. V., et al. 2003, ApJS, 148, 213
Pen, U. 1997, NewA, 2, 309
Perlmutter, S., et al. 1999, ApJ, 517, 565
Phillips, M. M. 1993, ApJ, 413, L105
Phillips, N. G., & Kogut, A. 2006, ApJ, 645, 820
Piacentini, F., et al. 2006, ApJ, 647, 833
Pierpaoli, E. 2003, MNRAS, 342, L63
Pierpaoli, E., Borgani, S., Scott, D., & White, M. 2003, MNRAS, 342, 163
Pogosian, L., Corasaniti, P. S., Stephan-Otto, C., Crittenden, R., & Nichol, R. 2005, Phys. Rev. D, 72, 103519
Rasia, E., Mazzotta, P., Borgani, S., Moscardini, L., Dolag, K., Tormen, G., Diaferio, A., & Murante, G. 2005, ApJ, 618, L1
Readhead, A. C. S., et al. 2004a, ApJ, 609, 498
———. 2004b, Science, 306, 836
Refregier, A. 2003, ARA&A, 41, 645
Refregier, A., Komatsu, E., Spergel, D. N., & Pen, U. 2000, Phys. Rev. D, 61, 123001
Reid, B. A., & Spergel, D. N. 2006, ApJ, 651, 643
Richard, O., Michaud, G., & Richer, J. 2005, ApJ, 619, 538
Richer, H. B., et al. 2004, AJ, 127, 2904
Ricotti, M., & Ostriker, J. P. 2004, MNRAS, 352, 547
Riess, A. G., Press, W. H., & Kirshner, R. P. 1996, ApJ, 473, 88
Riess, A. G., et al. 1998, AJ, 116, 1009
———. 2004, ApJ, 607, 665
———. 2005, ApJ, 627, 579
Ruhl, J. E., et al. 2003, ApJ, 599, 786
Sanchez, A., et al. 2006, MNRAS, 366, 189
Sato, K. 1981, MNRAS, 195, 467
Schalm, K., Shiu, G., & van den Schaar, J. P. 2004, J. High Energy Phys., 0404, 076
Schmalzing, J., & Buchert, T. 1997, ApJ, 482, L1
Schmalzing, J., & Gorski, K. M. 1998, MNRAS, 297, 355
Schmidt, B. P., et al. 1998, ApJ, 507, 46
Scranton, R., et al. 2003, preprint
Seager, S., Sasselov, D. D., & Scott, D. 2000, ApJS, 128, 407
Seljak, U., Sugiyama, N., White, & Zaldarriaga, M. 2003, Phys. Rev. D, 68, 3507
———. 2005a, Phys. Rev. D, 71, 103515
———. 2005b, Phys. Rev. D, 71, 043511
Semboloni, E., et al. 2006, A&A, 452, 51
Serebrov, A., et al. 2005, Phys. Lett. B, 605, 72
Sievers, J. L., et al. 2003, ApJ, 591, 599
Silk, J., & Wilson, M. L. 1981, ApJ, 244, L37
Simon, J., Verde, L., & Jimenez, R. 2005, Phys. Rev. D, 71, 123001
Skordis, C., Mota, D. F., Ferreira, P. G., & Bœhm, C. 2006, Phys. Rev. Lett., 96, 011301
Slosar, A., Seljak, U., & Makarov, A. 2004, Phys. Rev., D69, 123003
Smith, R. E., et al. 2003, MNRAS, 341, 1311
Sokasian, A., Yoshida, N., Abel, T., Hernquist, L., & Springel, V. 2004, MNRAS, 350, 47
Somerville, R. S., & Livio, M. 2003, ApJ, 593, 611
Soucail, G., Kneib, J.-P., & Golse, G. 2004, A&A, 417, L33
Spergel, D. N., & Goldberg, D. M. 1999, Phys. Rev. D, 59, 103001
Spergel, D. N., et al. 2003, ApJS, 148, 175
Starobinsky, A. A. 1982, Phys. Lett. B, 117, 175
Steigman, G. 2005, preprint
Sunyaev, R. A., & Zel'dovich, Y. B. 1970, Ap&SS, 7, 3
Takada, M., Komatsu, E., & Futamase, T. 2006, Phys. Rev. D, 73, 3520
Tegmark, M., de Oliveira-Costa, A., & Hamilton, A. J. 2003, Phys. Rev. D, 68, 123523
Tegmark, M., Zaldarriaga, M., & Hamilton, A. J. 2001, Phys. Rev. D, 63, 043007
Tegmark, M., et al. 2004a, Phys. Rev. D, 69, 103501
———. 2004b, ApJ, 606, 702
Tegmark, M., et al. 2006, Phys. Rev. D, 74, 3507
Tereno, I., Doré, O., van Waerbeke, L., & Mellier, Y. 2005, A&A, 429, 383
Tonry, J. L., et al. 2003, ApJ, 594, 1
Totani, T., Kawai, N., Kosugi, G., Aoki, K., Yamada, T., Iye, M., Ohta, K., & Hattori, T. 2006, PASJ, 58, 485
Trotta, R. 2007, MNRAS, 375, L26
Tumlinson, J., Vankatesan, A., & Shull, J. M. 2004, ApJ, 612, 602
Turner, E. L. 1990, ApJ, 365, L43
Turner, M. S., Steigman, G., & Krauss, L. M. 1984, Phys. Rev. Lett., 52, 2090
Vale, A., & Ostriker, J. P. 2006, MNRAS, 371, 1173
Van den Bosch, F., Mo, H., & Yang, X. 2003, MNRAS, 345, 923
Van Waerbeke, L., Mellier, Y., & Hoekstra, H. 2005, A&A, 429, 75
Venkatesan, A., Tumlinson, J., & Shull, J. M. 2003, ApJ, 584, 621
Verde, L., et al. 2002, MNRAS, 335, 432
———. 2003, ApJS, 148, 195
Vielva, P., Martínez-González, E., Barreiro, R. B., Sanz, J. L., & Cayón, L. 2004, ApJ, 609, 22
Vielva, P., Martínez-González, E., & Tucci, M. 2006, MNRAS, 365, 891
Vikhlinin, A., et al. 2003, ApJ, 590, 15
Vittorio, N., & Silk, J. 1984, ApJ, 285, L39
Voevodkin, A., & Vikhlinin, A. 2004, ApJ, 601, 610
Wambsganss, J., Bode, P., & Ostriker, J. P. 2004, ApJ, 606, L93
Wetterich, C. 1988, Nucl. Phys. B, 302, 668
Winitzki, S., & Kosowsky, A. 1998, NewA, 3, 75
Wyithe, J. S. B., & Cen, R. 2006, preprint (astro-ph/0602503)
Wyithe, J. S. B., & Loeb, A. 2003, ApJ, 588, L69
Yamaguchi, M., & Yokoyama, J. 2004, Phys. Rev. D, 70, 023513
Zaldarriaga, M., & Seljak, U. 2000, ApJS, 129, 431
Zehavi, I., et al. 2005, ApJ, 630, 1
Zlatev, I., Wang, L., & Steinhardt, P. J. 1999, Phys. Rev. Lett., 82, 896